A Nonlinear Energy Sink with Energy Harvester

By
Daniel Kremer

A thesis
presented to Lakehead University
in partial fulfillment of the requirement for the degree of
Master of Science
In
Control Engineering

Thunder Bay, Ontario, Canada, 2013

Abstract

The transfer of energy between systems is a natural process, manifesting in many different ways. In engineering transferable energy can be considered wanted or unwanted. Specifically in mechanical systems, energy transfer can occur as unwanted vibrations, passing from a source to a receiver. In electrical systems, energy transfer can be desirable, where energy from a source may be used elsewhere. This work proposes a method to combine the two, converting unwanted mechanical energy into useable electrical energy.

A nonlinear energy sink (NES) is a vibration absorber that passively localizes vibrational energy, removing mechanical energy from a primary system. Consisting of a mass-spring-damper such that the stiffness is essentially nonlinear, a NES can localize vibrational energy from a source and dissipate it through damping. Replacing the NES mass with a series of magnets surrounded by coils fixed to the primary mass, the dissipated energy can be directly converted to electrical energy.

A NES with energy harvesting properties is constructed and introduced. The system parameters are identified, with the NES having an essentially cubic nonlinear stiffness. A transduction factor is quantified linking the electrical and mechanical systems. An analytic analysis is carried out studying the transient and harmonically excited response of the system. It is found that the energy harvesting does not reduce the vibrational absorption capabilities of the NES. The performance of the system in both transient and harmonically excited responses is found to be heavily influenced by input energies. The system is tested, with good match to analytic results.

Acknowledgments

I would like to thank my supervisor Professor Kefu Liu, who saw potential in me and encouraged me into graduate studies. More importantly he gave me the freedom to explore, make mistakes, learn from them and find my own way. This helped me find a real passion for nonlinear vibrations, and their study. In addition I would like to thank all the Professors at Lakehead. The knowledge I gained here armed me with the tools to approach my problems creatively and analytically.

I would like to also thank Kailash Batia for his assistance in the machine shop, and for putting up with me and my questions. Also the 'Plastic Guys' of **Surecraft Plastic Ltd.** for supplying me with materials and information about plastics, and Gary Mezo of **Kildred Winding Industries Ltd.** for supplying the copper for the coils.

To my friends and family, I thank you all. Simply put, you always reminded me it was worth it. To Mason: thank you for staying up with me during the late nights, playing Frisbee with me, taking me for walks, and getting me out of the lab.

Weronika and Adam who were my original partners in designing the basis of this work for our undergraduate project, because of your hard work I had a strong foundation to work with, and had a lot of fun thinking it out with you.

Most importantly, my unending gratitude goes to my wife Weronika Grotowska. It was her idea to work with Dr.Liu for our undergraduate project, and it

was her initial idea. All of this work was also made possible by her patience, understanding, support and praise. I could not have done it without you.

Contents

1 Introduction 1

1.1 Motivation of the Research 1

1.2 Literature Review 4

1.2.1 Active and Semi Active vibration Control 4

1.2.2 Passive Vibration Absorption 6

1.2.3 Nonlinear Energy Sinks 6

1.2.4 Energy Harvesting 10

1.3 Objectives and Contributions 11

1.4 Thesis Outline 13

2 Energy Harvesting Nonlinear Energy Sink 14

2.1 Test Apparatus Overview 14

2.2 Nonlinear Energy Sink 16

2.2.1 Experimental Setup of the NES 16

2.2.2 Preliminary Equations of Motion 20

2.3 Energy Harvesting System 22

2.4 Conclusion 30

3 System Parameter Identification 31

3.1 Primary System Parameters 31

3.2 Transduction Factor – Electrical Damping Coefficient 33

3.3 Nonlinear Stiffness and Damping 36
3.3.1 Effect of Repelling Magnets 37
3.3.2 Beam Nonlinear Stiffness and Damping 38
3.3.3 Electrical Damping 43
3.4 Conclusion 46
4 System Analysis 47
4.1 Transient Response 47
4.1.1 Vibration Absorption 48
4.1.2 Frequency Energy Plots 55
4.1.3 Effects of Damping 61
4.1.4 Transient Energy Harvesting 62
4.2 Harmonically Forced Responses 65
4.2.1 Validation of the Solutions 75
4.2.2 Interpretation of FRPs 79
4.2.3 Response Analysis 80
4.2.3.1 Low Amplitude Excitation 81
4.2.3.2 High Amplitude Excitation 86
4.2.4 Energy Harvesting 88
4.3 Conclusion 91
5 Apparatus Testing 93
5.1 Testing Setup 93
5.2 Transient Response 94
5.3 Harmonically Excited Testing 98
5.4 Conclusion 106
6 Summary 107

List of Figures

1.1: Common vibrational problems: a) transient fixed based; b) harmonic base excitation.....2

1.2: Transient response of the primary system to an initial displacement of 0.002 m. Long sustain of vibration due to low damping coefficient. $m_p = 0.917$ (k[illegible]) , $k_p = 4970$ ([illegible]), [illegible] $= 0.36$ (k[illegible]) and $x0 = 3$

(m[illegible]).....3

1.3: Displacement ratio of system: [illegible] $= 11.72$

(H[illegible]).....4

1.4: A typical arrangement for an active vibration controller scheme 5

1.5: General schematic of a NES with base excitation. 7

1.6: General schematic of an electromagnetic energy harvester.....11

2.1: Schematic of the physical apparatus. 15

2.2: Schematic of the entire system. 15

2.3: Image of the NES setup. 17

2.4: Effects of beam preloading; a) normally clamped beam with equilibrium at [illegible] $= 0$, b) a preloaded beam with equilibrium point at [illegible] $\neq$

0. 18

2.5: Repelling magnet configuration for the NES. 19

2.6: Transient response of the NES after being struck; a) displacement b) WT Morlet spectra of response. 20

2.7: Free body diagram of the generalized system. 21

2.8 Schematic of the energy proposed energy harvesting configuration. 22

2.9: Simplified model of an energy harvester 23

2.10: Image showing the coil arrangement. 24

2.11: Diagram of single coil and magnet. 25

2.12: Electrical system of 27

2.13: Free body diagram of all forces acting on the oscillating magnet. 29

3.1: a) recorded free response of primary system with fitted damping curve, b) FFT plot of response with ◆◆$_p$ = 11.74 (H◆◆) .....

32

3.2: FEMM analysis results: a) magnitude of flux density b) axial component of the flux density c) radial component of the flux density. Black boxes signify the outer dimension of the magnets. 34

3.3: a) diagram of coil and magnet b) B_a data within the region of $r_1 - r_2$ over the length of magnet. 35

3.4: a) transduction factor $k_{◆◆1}$ for a single coil. b) total transduction factor k_t and the fitted data of for the data. 36

3.5: a) static test arrangement for determining force displacement relationship, b) force diagram of magnet arrangement. 37

3.6: a) magnetic force displacement measurements and fitted data, b) total force displacement relationship for different magnet spacings. 38

3.7: Surface force map for the NES in the phase plane. 40

3.8: a) NES: force-displacement relationship at ◆◆(◆◆,0), b) NES: force-velocity relationship at ◆◆(0,◆◆)

.....41

3.9: Primary system: a) Surface force map of the primary in the phase plane, b) force-displacement relationship at ◆◆(◆◆,0). .....

43

3.10: NES with load resistance of $10(\Omega)$: a) Surface force map of the primary in the phase plane, b) force-velocity relationship at ◆◆(0,◆◆). .....

44

3.11: NES with load resistance of $50(\Omega)$: a) Surface force map of the primary in the phase plane, b) force-velocity relationship at ◆◆(0,◆◆). .....

44

3.12 Approximate induced voltages 45

4.1: Simulation results for initial conditions of $X = 6 \times 10 - 4$(◆◆): (a) displacements (solid line: primary system; dashed line: NES); (b) percentage of the instantaneous total energy in the NES and (c) voltage across load resistor. 49

4.2: Simulation results for initial conditions of $X = 1 \times 10 - 3$(◆◆): (a) displacements (solid line: primary system; dashed line: NES); (b) percentage of the instantaneous total energy in the NES and (c) voltage across load resistor. 50

4.3: Simulation results for initial conditions of $X = 2 \times 10 - 3$(◆◆): (a) displacements (solid line: primary system; dashed line: NES); (b) percentage of the instantaneous total energy in the NES and (c) voltage across load resistor. 51

4.4: Simulation results for initial conditions of $X = 5 \times 10 - 3$(◆◆): (a) displacements (solid line: primary system; dashed line: NES); (b) percentage of the instantaneous total energy in the NES and (c) voltage across load resistor. 52

4.5: Percentage of initial energy dissipated in the NES as a function of initial energy; points refer to four specific simulations..... 53

4.6: Simulation results for increase in m_p with initial conditions of $X = 1 \times 10 - 3(\text{m})$: (a) displacements (solid line: primary system;
dashed line: NES); (b) percentage of the instantaneous total energy in the NES and (c) voltage across load resistor. 54

4.7: Simulation results for increase in k_p with initial conditions of $X = 1 \times 10 - 3(\text{m})$: (a) displacements (solid line: primary system;
dashed line: NES); (b) percentage of the instantaneous total energy in the NES and (c) voltage across load resistor. 54

4.8: Analytic approximations of frequency energy plot: backbone curves S11±..... 59

4.9: Frequency energy plots of wavelet transforms of the relative response $\text{m} - \text{m}$ of the four initial simulations with superimposed backbone curves S11±: a) low initial energy $X = 6 \times 10 - 4(\text{m})$, b) mid-low initial energy $X = 1 \times 10 - 3(\text{m})$, c) mid-high energy level $X = 2 \times 10$
$3(\text{m})$ and d) high energy level $X = 5 \times 10 - 3(\text{m})$.....

60

4.10: Energy dissipated by NES as a function of initial displacement and load resistance.....61

4.11: Simulation results for initial conditions of $X = 5 \times 10 - 3(\text{m})$ and $\text{m}_{\text{m m m}} = 10\Omega$: (a) displacements (solid line: primary system; dashed
line: NES); (b) percentage of the instantaneous total energy in the NES and (c) voltage across load resistor..... 62

4.12: $\text{m}(\text{m}_{\text{m m m}})$ as a function of load resistance.....

64

4.13: Energy across load resistor as a function of initial displacement and load resistance..... 64

4.14: Energy across load resistor as a function and load resistance for different initial displacements. 65

4.15: FEP for $Y = 0.005$ (��) and ��$_{\text{[illegible]}} = 50(\Omega)$: a) primary displacement ��$_p$; b) relative displacement H. Blue lines indicate stable periodic

orbits. Red lines are unstable indicating non periodic orbits. Black squares indicate Hopf bifurcation points and green triangles limit points. Red circles are responses from numerical integration of equations (3.23),(3.24). 77

4.16: SMR when $Y = 0.005$ (m), $\omega_{linear} = 50(\Omega)$ and $\Omega = 14.4$ (Hz): a) amplitudes computed from equations (4.77)-(4.80); b)reconstituted responses from equation (4.81); c) numerically integrated responses from original equations (3.23),(3.24). 78

4.17: SMR when $Y = 0.005$ (m), $\omega_{linear} = 50(\Omega)$ and $\Omega = 16.5$ (Hz): a) amplitudes computed from equations (4.77)-(4.80); b)reconstituted responses from equation (4.81); c) numerically integrated responses from original equations (3.23),(3.24). 78

4.18: Increasing frequency sweep. Arrows indicate response path as frequency is increased. 79

4.19: Decreasing frequency sweep. Arrows indicate response path as frequency is decreased. 80

4.20: Comparison of two types of response regimes. A) high amplitude excitation, B) low amplitude excitation. Green line represents primary system with NES disengaged. 81

4.21: FRP for $Y = 8 \times 10 - 5m$ and $\omega_{linear} = 50(\Omega)$: Blue lines indicate stable periodic response and red lines unstable response. Black squares indicate Hopf bifurcation points and green triangles limit points. Green line represents primary system with NES disengaged. 82

4.22: FRP for $Y = 8 \times 10 - 5m$ and $\omega_{linear} = 50(\Omega)$ with closed amplitude island: Blue lines indicate stable periodic response and red lines unstable response. Black squares indicate Hopf bifurcation points and green triangles limit points. Green line represents primary system with NES disengaged. 82

4.23: FRP for variations in load resistance. $Y = 8 \times 10 - 5m$. Periodic stability and bifurcation points not shown for clarity. 83

4.24: Primary displacement ratio as a function of force amplitude for $\text{R}_{\text{load}} = 50(\Omega)$. .....

84

4.25: FRP for $\text{R}_{\text{load}} = 50(\Omega)$: a) Y =9.22×10−5 (m) b) $Y = 1.143 \times 10 - 4(\text{R})$ .....

85

4.26: Primary displacement ratio as a function of force amplitude, arrow indicating an increase in load resistance. Lines correspond to a load resistance of 12, 25, 50 and 100 (Ω). 86

4.27: FRP for $Y = 0.001(\text{R})$ with changing load resistance, arrow indicating an increase in load resistance. Response lines correspond to a load resistance of 12, 25, 50 and 100 (Ω). Green line represents primary system with NES disengaged. 87

4.28: FRP for $Y = 0.00015(\text{R})$ with changing load resistance, arrow indicating an increase in load resistance. Response lines correspond to a load resistance of 25, 50 and 100 (Ω). Green line represents primary system with NES disengaged. 88

4.29: a) FRP for relative displacement and b) peak power as a function of frequency: $Y = 8.722 \times 10 - 5(\text{R})$ with changing load resistance, arrow indicating an increase in load resistance. Response lines correspond to a load resistance of 12, 25, 50 and 100 (Ω). 90

4.30: a) FRP for relative displacement and b) peak power as a function of frequency: $Y = 0.00015(\text{R})$ with changing load resistance, arrow indicating an increase in load resistance. Response lines correspond to a load resistance of 12, 25, 50 and 100 (Ω). 91

5.1: Image of the apparatus testing..... 93

5.2: Experimental results for $X = 1.085 \times 10 - 3m$ and $\text{R}_{\text{load}} = 50(\Omega)$: (a) displacements (solid line: primary system; dashed line: NES); (b)

percentage of the instantaneous total energy in the NES and (c) voltage across load resistor. 94

5.3: Experimental results for $X = 1.949 \times 10 - 3(\square\square)$ and $\square\square_{l\square\square\square} =$ (a) displacements (solid line: primary system; dashed line: NES); (b) percentage of the instantaneous total energy in the NES and (c) voltage across load resistor. 95

5.4: Experimental results for $X = 3.172 \times 10 - 3(\square\square)$ and $\square\square_{l\square\square\square} = 50(\Omega)$: (a) displacements (solid line: primary system; dashed line: NES);
(b) percentage of the instantaneous total energy in the NES and (c) voltage across load resistor. 96

5.5: FRPs of wavelet transforms from the relative response $\square\square_a - \square\square_p$ of the 3 tests with superimposed backbone curves S11± with $\square\square_{l\square\square\square} = 50(\Omega)$: a) $X = 1.085 \times 10 - 3(\square\square)$, b) $X = 1.949 \times 10 - 3(\square\square)$, and c) $X = 3.172 \times 10 - 3(\square\square$ 97

5.6: Comparison of the analytic and experimental frequency response of the primary system for shaker current of $\square\square_{\square\square R\square\square} =$

$0.7\square\square$ 99

5.7: Test results for a shaker current of $\square\square_{\square\square R\square\square} = 0.7(\square\square)$ and $\square\square_{l\square\square\square}$ =

$50(\Omega)$. a) displacement ratio, blue line experiment results with NES removed; b) average power consumed by the load resistor; c) relative displacement ratio 101

5.8: Test results for a shaker current of $\square\square_{\square\square R\square\square} = 0.7(\square\square)$ and $\square\square_{l\square\square\square}$

=

$26.3(\Omega)$. a) displacement ratio, blue line experiment results with NES removed; b) average power consumed by the load resistor; c) relative displacement ratio 102

5.9: Recorded displacement response for $\square\square_{\square\square R\square\square} = 0.7(\square\square)$ and $\square\square_{l\square\square\square} = 26.3\Omega$ and a excitation frequency $\Omega = 11.5(H\square\square)$.

..... 103

5.10: Test results for a shaker current of $I_{RMS} = 1(A)$ and $R_{load} = 26.3(\Omega)$. a) displacement ratio, blue line experiment results with NES

removed; b) average power consumed by the load resistor; c) relative displacement ratio.....104

5.11: Test results for a shaker current of $\mathrm{RMS}(I_{load}) = 1.5(A)$ and $R_{load} = 26.3(\Omega)$. a) displacement ratio γ_p, blue line experiment results with NES removed; b) average power consumed by the load resistor; c) relative displacement ratio.....105

List of Tables

2.1: Physical parameters of beam and magnets. 21

2.2: Coil physical properties..... 23

3.1: Estimated primary system parameters..... 33

3.2 Estimated parameters of NES identified using restoring force surface method..... 42

4.1: Calculated results of dissipated energy percentage for four simulations..... 53

4.2: Parameters for comparison simulations: 1) change in primary mass, 2) changing in primary stiffness..... 54

4.3: Maximum excitation amplitudes for various resistances..... 86

5.1: Comparision of harvested energy to predicted harvested energy..... 98

List of acronyms and abbreviations

TET	Targeted energy transfer
SMR	Strongly modulated response
FRP	Frequency response plot
FEP	Frequency energy plot
TMD	Tuned Mass Damper
NES	Nonlinear energy sink
RMS	Root mean square
FFT	Fast Fourier transform
WT	Wavelet transform

Chapter 1

Introduction

1.1 Motivation of the Research

The presence of undesirable vibrations in structures is a problem that has been studied for decades in engineering. Vibrations occur in numerous ways in everyday life; earthquakes, running motors, or momentary strikes of force can transmit vibrational energy to structures housing people or fragile items. Researchers and engineers examine the causes and potential solutions for mitigating vibrations.

This work will focus on two vibrational problems that commonly occur in structures: 1) the transient response of a system and 2) the harmonic base excitation. Figure 1.1 shows the schematic for the transient and base harmonically forced systems where x_p (x) is the absolute displacement of the primary structure, k_p and c_p are the stiffness and the damping coefficients for the primary system respectively. In both of the cases the main goal is the vibration attenuation of the primary mass.

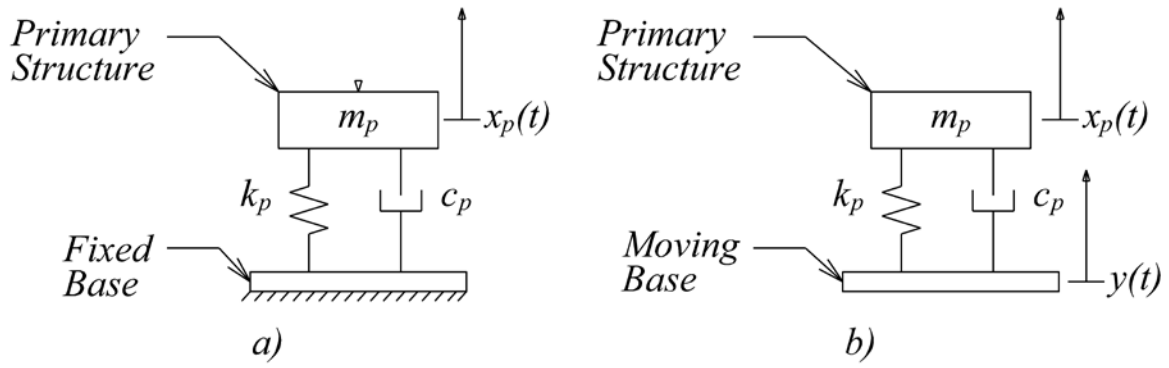

Figure 1.1: Common vibrational problems: a) transient fixed based; b) harmonic base excitation

In the case of the transient response of a system shown in Fig. 1.1(a), the primary mass is set into vibrations by an initial disturbance. The initial disturbance can be realized by either a momentary strike, initial velocity or initial displacement. The equation of motion for this system is described in Eqn.(1.1). The natural frequency of the system can be determined by Eqn.(1.2).

$$m_p\ddot{x}_p + c_p\dot{x}_p + k_p x_p = 0, \qquad x_p(0), \dot{x}_p(0) \qquad (1.1)$$

$$\omega_p = \sqrt{\frac{k_p}{m_p}} \qquad (1.2)$$

Figure 1.2 highlights the main problem in the transient response for a system with a low damping coefficient. The primary system is set into free vibration by an initial displacement and released, oscillating for an extended period of time at the natural frequency ω_p. The sustained vibrations in the system are unwanted, and the goal is to absorb these vibrations and to reduce the amount of time they are present.

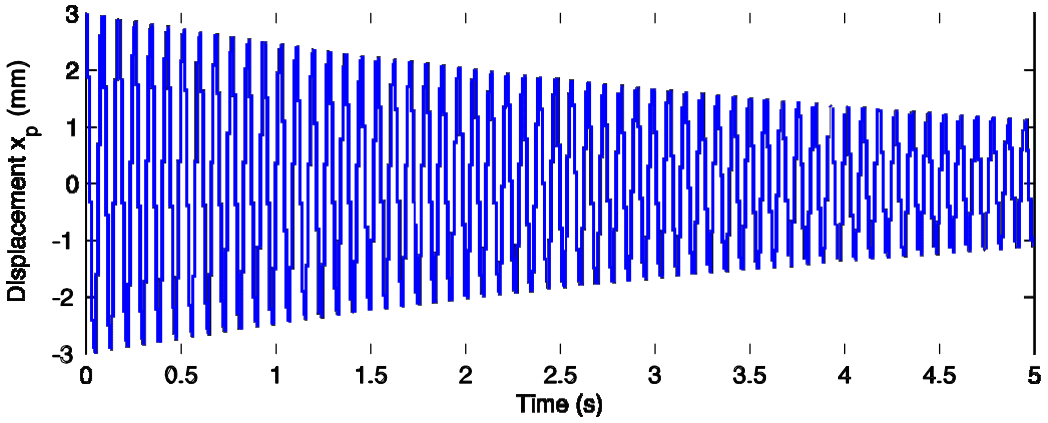

Figure 1.2: Transient response of the primary system to an initial displacement of 0.002 m. Long sustain of vibration due to low damping coefficient. $c_p = 0.917$ (k), $k_p = 4970$ (k/), $c_p = 0.36$ (k/) and $x_p(0) = 3$ (m.

Figure 1.3 presents the other common problem found in vibrations, where a primary system is excited by harmonic base displacement $y(t)$. Equations (1.3) - (1.4) describe the equations of motion for this system.

$$m_p \ddot{x}_p + c_p \dot{x}_p + k_p x_p = c_p \dot{y} + k_p y \quad (1.3)$$

$$y = Y \cos(\Omega t) \quad (1.4)$$

where Ω is the frequency and Y is the magnitude of base excitation. Here the displacement and velocity of the base transmitted to the primary system through the system spring and damper, generating an applied force to the mass causing it to oscillate. Depending on the frequency of the base excitation, the oscillating amplitude of the primary mass can either be amplified, or in some regions attenuated. Figure 1.3 shows the displacement transmissibility ratio (amplitude of x_p over base motion amplitude Y) for a system with the natural frequency at $\omega_n = 21.72$ (H).

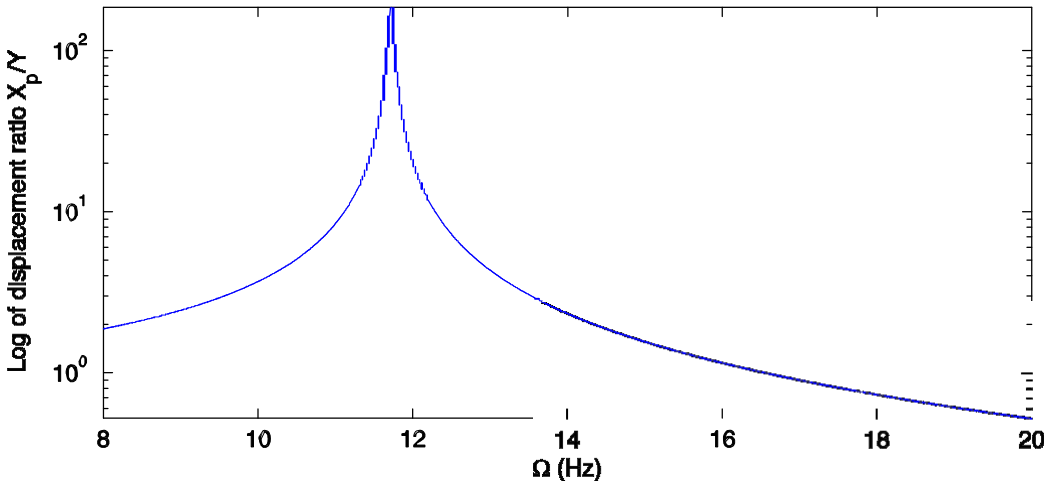

Figure 1.3: Displacement ratio of system: $\omega_n = 11.72$ ($H\omega$)

It can be seen that when the base frequency is equal to that of the primary system, there is a large amplification of the base motion. This condition is known as resonance, and can cause major problems in areas such as buildings and bridges. Addressing the problem of harmonic excitation will be one of the main focuses in this work.

With the basic problems of vibration identified, it is interesting to take a different view and look for benefits. In both the transient and harmonically force scenarios one fact stands out; the cause of any vibration is due to energy added to the system. The unwanted energy present in the system could be made useful, if harvested in an effective manner. Combining vibration absorption and vibrational energy harvesting, this work will try to address both topics, exploring the possibility for a way to minimize vibration and collect the energy for use elsewhere.

1.2 Literature Review

1.2.1 Active and Semi Active vibration Control

A large area of research in the control and attenuation of vibrations in primary structures is in active and semi active control. For both active and semi active vibration controls, unlike passive vibration control, there is need of additional components. Sensors, control systems and actuators are required to provide the necessary

components to control the vibrations. Figure 1.4 depicts a typical arrangement for an active control scheme. Sensors are used to monitor the motion of either primary structure or base and inputted to a controller that drives an actuator to apply a force to the structure to minimize vibration. Active control has a versatile and adaptable structure though the main drawbacks are power consumption and the possibility of instability if controller or model parameters are ill fitted. A thorough review of this subject is found in [1]. Some examples of active control schemes include active tuned mass dampers (ATMD) and distributed actuator systems.

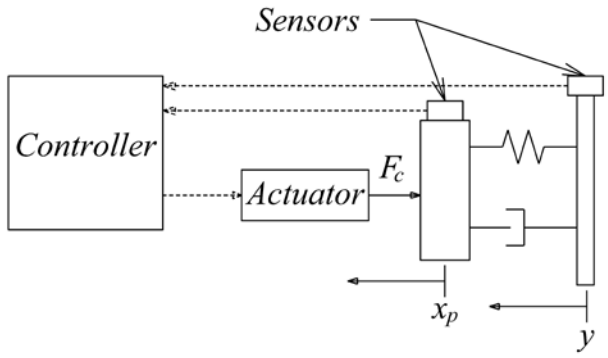

Figure 1.4: A typical arrangement for an active vibration controller scheme

Active control systems have been applied to a variety of vibration problems and structures. Minimizing the vibrations transmitted to a person in a vehicle, a dual controller for active seat suspension in [2] is investigated experimentally, while in [3] an active seat suspension is aimed to reduce the vibrational frequencies that match the characteristic frequencies of the human body.

Semi active vibration control is very similar to active control, the main difference being that no force is applied to the primary structure, control is instead gained through the change of system parameters such as stiffness and damping. Some examples of semi active control include stiffness control devices, electrorheological (ER) dampers, magnetorheological (MR) dampers and friction control devices. In [4] an encapsulated MR fluid is studied. Changing the magnetic field through the fluid, the stiffness and damping properties are altered as well resulting in good broadband vibration control. Employing an ER damper to torsional vibrations, the work reported in [5] demonstrates the fast reversible physical changes

that can occur when an electric field is applied to an ER fluid, resulting in good vibration damping.

1.2.2 Passive Vibration Absorption

The traditional means of vibration absorption is through the use of a linear vibration absorber. An absorber consists of a second mass-spring-damper system attached to the primary structure to protect it from vibrating. By adding the mass-spring-damper system, the overall system has two degrees of freedom, thus two natural frequencies [6]. Through careful tuning of the absorber parameters, good vibration suppression can be achieved. This arrangement is also known as the so-called tuned mass damper (TMD).

The limitation of the TMD is that it needs to be tuned for specific exciting frequency to be effective, outlined in the classic work [7]. In the transient regime, when properly tuned the TMD is a very effective vibration absorber, though changes in system parameters of mass or stiffness in the primary system can drastically change performance. Applied harmonic force to the system makes this especially true. The TMD is effective for a very small frequency region, if the excitation frequency changes, vibrations of the primary system will undergo amplification at the two natural frequencies. The study of the TMD will not be a focus in this work.

1.2.3 Nonlinear Energy Sinks

In the last two decades the study of nonlinear energy sinks (NES) has received much attention. A NES consists of a small mass and a spring with an essential nonlinearity and linear damper attached to a primary system, with the general schematic given in Fig. 1.5.

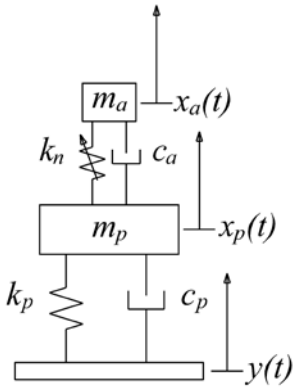

Figure 1.5: General schematic of a NES with base excitation.

The critical difference between a NES and the more general nonlinear vibration absorber as discussed by [8], is the lack of linear stiffness in the absorber. The equations of motion for a base excited linear oscillator are given in Eqns.(1.5)-(1.6), noting no linear stiffness k_a present for the absorber system. In below system and the majority of studied works, the nonlinear restoring force is realized as cubic, providing a smooth but strong nonlinearity.

$$m_p\ddot{x}_p + c_p\dot{x}_p + c_p\dot{x}_p - c_a\dot{x}_a - c_p\dot{x} - c_n(\dot{x}_p - \dot{x}_a)^3 = c_p y + c_p\dot{y} \tag{1.5}$$

$$m_a\ddot{x}_a + c_a\dot{x}_a - c_p\dot{x} + c_n\dot{x}_a - c_p\dot{x}^3 = 0 \tag{1.6}$$

The descriptions of the phenomenon produced vary depending on the goal of system being analyzed. In [9, 10] the authors examine the underlying Hamiltonian systems of an essentially nonlinear system attached to a linear oscillator in the transient regime. The authors show the effectiveness of such a system to passively absorb vibrational energy from the linear oscillator, and designate the phenomenon as energy pumping. The effectiveness of the absorber is attributed to internal a 1:1 resonance condition, where the nonlinear oscillator will always match the frequency of the linear oscillator. The phenomenon of energy pumping is explained as the controlled one way channeling of vibrational energy to a passive nonlinear "sink" where it localizes and diminishes in time due to damping dissipation. This is where the NES gains its full name. A detailed analysis of energy pumping is studied in

[11]. The authors present a comparison of the NES to the traditional TMD, and show that the NES has greater efficiency and robustness compared to the TMD.

In later works [12, 13], the phenomenon of energy pumping is replaced with the more meaningful designation of targeted energy transfer (TET). The significance is that with the attachment of an essentially nonlinear oscillator to a linear oscillator, the intent is to intentionally transfer vibrational energy to the nonlinear oscillator in a targeted way to reduce vibration in the linear system. Attributing TET again to the 1:1 internal resonance, the authors explain that the robustness of a NES is due to the fact of not having a preferential natural frequency in absence of linear stiffness, and that the frequency of the NES is generated by the nonlinear term. A consequence of this is that there is an energy threshold for the effectiveness of the NES in the transient regime in order to engage the nonlinearity. In [14], the authors present a detailed study of the transient response for TET. Three initial energy regions are defined that determine the effectiveness and potential for TET. It is shown that for low energies no significant energy dissipation in the NES is present, and that TET is not achieved. Increasing the initial energy levels to a defined intermediate level engages the nonlinear stiffness and TET is realized, the NES dissipating from 90-95% of the total vibrational energy within the system. Increasing the initial energy to the defined high energy region, TET is still realized but the effectiveness decreases, although the NES is still capable of dissipating a significant percentage of the energy. In the study provided by [14], a very interesting feature is noted; that the design of the NES was not pre-tuned, with no a-priori knowledge. The design of the NES has only the criteria of a small mass, zero linear stiffness and cubic stiffness. Compared to other vibration control schemes such as active, semi-active and traditional passive methods which require fine tuning for good performance, the NES is amazingly simple to design while still obtaining good results. Optimal results can still be achieved, by varying the mass, nonlinear stiffness and damping of the NES when the input energies are known [15].

For a harmonically forced system shown in Fig. 1.5, the NES has also shown to be very effective at absorbing vibrations. In papers [16-18], the response of a linear oscillator with an attached NES is analytically derived. It is shown that the primary system and NES can exhibit three types of response; common steady state response, weakly modulated response and the very interesting strongly modu-

lated response (SMR). The analysis of these systems is employed through a complexification-averaging method [14], where the dynamics are partitioned into slow and fast components, and then the averaging of the response at the forcing frequency. As previously discussed, the assumption of 1:1 resonance applied in this averaging for both the primary and NES systems. The resulting equations are then expressed in terms of saddle node and Hopf bifurcations [14].A frequency response plot (FRP) of the system is generated for the system for a broad region of forcing frequencies. The saddle node bifurcation points on the FRP generally indicate areas the existence of multiple periodic solutions, two being stable and the third unstable. Regions of Hopf bifurcation characterize a SMR response, which is shown to be related to the relaxation of the slow flow dynamics. It is shown that under certain conditions the efficiency of the NES as a vibration absorber is exceptional, and far exceeds that of a TMD. Regions with SMR responses are of particular interest, where the SMRs are regarded as repetitive TETs, and should be the aim of NES design.

Employing the theoretical and analytic theories, the NES has also been proven experimentally, though generating an essentially nonlinear stiffness proves to be difficult. In [19] the essentially nonlinear stiffness is generated by two coil springs attached to a mass on a linear rail, the springs are able to pivot at both ends. At the center position the springs are not under any pretension or compression resulting in a low linear stiffness. It is demonstrated that the experiment performs very well and produces a good match with the theoretical predictions, obtaining the 1:1 resonance and exhibiting TET. The authors also subject the system to a various earthquake type forcings. Here the ability of the NES to dynamically change frequency results in excellent vibration mitigation in the primary structure. Achieving the essential nonlinearity through thin steel wires with very little pretension, papers [20-22] illustrate the success of experimentally implementing a NES, with good matching to theoretical theory. The systems demonstrated the initial energy threshold as well as the optimal intermediate energy of TET. Using the same device, [23] examines the system under harmonic excitation. In this work the experiment differs from the ideal theoretical results, the system consisting of periodic solutions with saddle node bifurcations, but lacking the ideal Hopf and SMR. The results still demonstrate the regions of good performance for vibration suppression but still have amplification near primary resonance. The authors also report some

inconsistences between the experiment and the theoretical predictions, citing difficulty with modeling the cubic stiffness, resulting in a disagreement in the magnitude of the response.

1.2.4 Energy Harvesting

Energy harvesting devices gather energy from the environment. Energy harvesting has seen growth in many fields, scavenging energy from excess heat, electromagnetic waves and ambient vibrational energy. This energy can be used in various means, but are extremely useful in the area of wireless or remote networks [24], where getting power to sensor networks would be difficult or prohibitive. Continuing the theme of vibration this work will focus on the harvesting of vibrational energy.

Vibration energy harvesters use the principles of a single degree of freedom spring-mass-damper system that is excited by the external environment. This is very similar to Fig. 1.1(b). The external vibration causes the mass to oscillate generating mechanical energy. Transduction methods are employed to couple the oscillating mass to an electrical circuit for conversion of mechanical energy to electrical energy. Electromagnetic inductance, capacitance and piezoelectric elements are some of the most common transduction methods.

Piezoelectric energy harvesters generally consist of a cantilevered beam with an inertia mass placed on the end of the beam. A piezo-ceramic material is layered on the cantilevered beam which is stressed as the mass oscillates which converts the mechanical energy to an electric one. A review of current piezoelectric technologies can be found in [25-29], and will not be further discussed in this work.

Electromagnetic vibration energy harvesters are of particular interest, as they are easy to implement in existing mass-spring-damper systems, one of the goals of this work. The concept is that a housing is created with a spring-mass-damper system contained within, in a way that the mass can move relative to the housing. The mass will consist of a magnet with a strong magnetic field, and will be surrounded by a coil which is fixed to the housing, a simplified schematic is shown in Fig. 1.6.

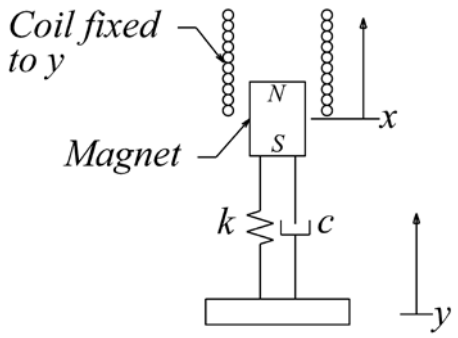

Figure 1.6: General schematic of an electromagnetic energy harvester

The housing is then rigidly attached to a vibration source generally of a harmonic forcing nature. The vibrational energy is transferred to the mass causing it to vibrate within the coil changing the magnetic field through the coil, inducing a voltage in the coil wire. The voltage generated is directly related to the relative velocity between the coil and magnet, where greater velocities will induce greater voltages [30, 31]. To ensure the highest velocities the system requires tuning to generate a resonance condition, matching the natural frequency of the generator to the frequency of the energy source. This leads to the main difficulty in linear vibrational energy harvesters, the effectiveness is limited to a small region of frequencies.

To address this problem nonlinear features are integrated into electromagnetic energy harvesters, in an attempt to increase the frequency range and gain wideband energy harvesting. Employing a levitating magnet for nonlinear stiffness [32], the authors achieved a moderate increase in frequency range. In [33], the same concept of a levitating magnetic mass is proposed where theoretical analysis predicts a good increase in frequency range. In both examples the systems are subject to jump phenomenon.

1.3 Objectives and Contributions

From the literature review it emerges that the NES is an excellent device performing well in both the transient and harmonically forced regimes. It is worthwhile to point out a very interesting aspect of the NES, mainly the description given for en-

ergy pumping by [10], namely that energy pumping is the controlled one way channeling of vibrational energy to a passive nonlinear "sink" where it localizes and diminishes in time due to damping dissipation. This work proposes that a NES be designed in a manner where the dissipated energy would be converted to a useful electrical power. The aim is to design and construct a nonlinear energy sink capable of energy harvesting

From a broad perspective this implies that a device could be manufactured that would have some very interesting complimenting features. The first feature is that the device would be a capable vibration absorber in the transient regime that would provide useable electrical energy. The second more intriguing feature would be broad band vibration absorption with broad band energy harvesting, a difficult feature to implement.

In order to achieve these goals, several objectives have been defined:

1. Design and build a test apparatus that consists of a primary system that acts as a linear oscillator, and allows for the testing of the transient response as well as a harmonically forced response.

2. Propose and construct a nonlinear energy sink that is capable of energy harvesting. The NES must have a low mechanical damping component and energy harvesting mass.

3. Identify the system parameters with main focus on the essentially nonlinear stiffness of the NES.

4. Perform an analytical analysis of the performance of the NES, and identify the key characteristics of the dynamical system.

5. Test the performance of the designed NES with energy harvesting.

1.4 Thesis Outline

This thesis will outline the development and study of a proposed NES with energy harvesting. Chapter 2 will provided an overview of the apparatus including of the essential nonlinearity was achieved. Basic equations of motion for the system will be identified in terms of general stiffness. A derivation of the electromagnetic induction will result in the development of a transduction factor which will link the mechanical and electrical systems. Chapter 3 will focus on the identification of system parameters. The transduction factor will be found through the use of a finite element model. The stiffness of the NES and primary systems will be found using the restoring force surface method, with the NES stiffness having an essentially cubic nonlinearity. An analytic study of the system will be conducted for transient and harmonically excited regimes in Chapter 4. Chapter 5 will verify the performance of the apparatus through testing. Chapter 6 summarizes the main findings of the research.

Chapter 2

Energy Harvesting Nonlinear Energy Sink

2.1 Test Apparatus Overview

One of the main objectives of this research was the design and construction of a test apparatus. Design goals were to create an apparatus to test the effectiveness of using a nonlinear energy sink for energy harvest. The apparatus should be readily constructed in house and suitable for the use of the equipment available.

Figure 2.1 shows the schematic of the developed system. The apparatus consists of three main parts: the base, the primary system, and the NES. The primary system is a platform supported by two steel plates. The lower ends of the steel plates are fastened to the base which can translate freely along a linear track through a linear bearing. The NES is made up of a mass attached to a thin steel beam. $x_1(t)$ and $x_2(t)$ represent the absolute displacement of the primary system mass and of the NES mass respectively, while $x_b(t)$ is the displacement of the base. The base is rigidly attached to a Brüel & Kjær type 2809 shaker fixed to ground, driven by a Brüel & Kjær type 2718 power amplifier. Three Wenglor CP24MHT80 reflex sensors are used to measure base displacement, the primary mass displacement, and the NES mass displacement, respectively. For analysis of the transient response of the system, the base can be rigidly fixed.

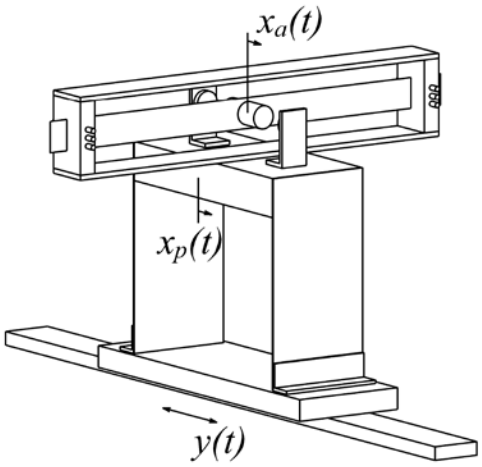

Figure 2.1: Schematic of the physical apparatus.

Figure 2.2 illustrates the data collection configuration of the entire system including all sensory data and analog lines. Analog input data is collected by the dSpace dS1104 data acquisition board, which also provides the output driving signal to the power amplifier. The control and sensing programming is produced using Matlab® Simulink® environment and the programming is directed by the dSpace Control Desktop software to the dS1104.

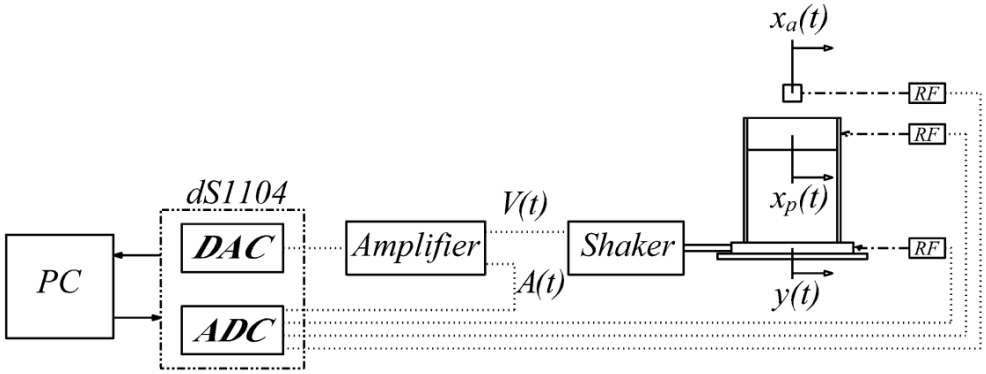

Figure 2.2: Schematic of the entire system.

An important feature of the system is the monitoring of the amplifier amperage being delivered to the shaker. With a constant applied voltage to the shaker the amperage delivered to the shaker will change according to the dynamics of the system vibration system. The output amperage is monitored in real-time and is dynamically changed to maintain a constant current to the shaker, this insures that

the force applied to the system will remain approximately constant regardless of system dynamics.

2.2 Nonlinear Energy Sink

In section 1.2.3, the NES has been shown to be a very effective vibration absorber for different forcing and transient regimes. To achieve this desired performance the absorber must be constructed to meet certain criteria.

$$m_a\ddot{x}_a + c_a\dot{x}_a + k_a x_a^3 = 0 \qquad (2.1)$$

An ideal NES has the form of Eqn.(2.1). Two main features of the NES are worth repeating for the design; 1) the ideal NES has no linear stiffness k_a and 2) the cubic term is strongly nonlinear. For the experiment design these two features will be implemented, as well as a third. In section 1.3 it was identified that to have a good performance in terms of energy harvesting, the mechanical damping should be kept to a minimum, or from Eqn.(2.1) kept c_a as low as possible.

2.2.1 Experimental Setup of the NES

The experimental NES consists of two main parts that make up the nonlinear restoring force while having a low mechanical damping. The first is a steel beam that is fixed at the ends with a set of two neodymium (NdFeB) permanent magnets fixed at the center position of the beam. The beam ends are fixed to a rigid cage surrounding the beam, which is attached to the primary mass. The two magnets act as the mass of the NES. The second component is a set of collinear NdFeB magnets that are placed in a repulsive orientation to that of the NES mass magnets. The fixed repelling magnets are mounted on brackets that can be moved to change the distance between the NES mass magnets and the fixed magnets. Figure 2.3 depicts the actual setup of the NES.

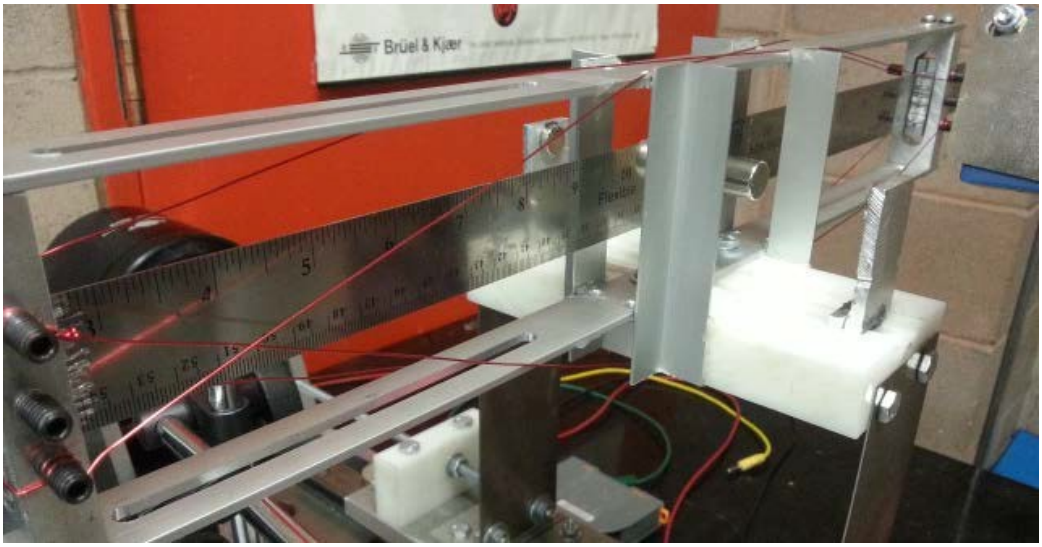

Figure 2.3: Image of the NES setup.

The selection of a steel beam for a spring was due to a few design factors. The main determining factor was to have low mechanical damping, while providing linear motion. Using a clamped beam removes the presence of any damping due to friction of mating parts, as with a linear rail system. A long thin steel beam with sufficient width would provide a good range of lateral motion, while remaining rotationally stiff. The employment of thin beams as restoring force springs has been extensively used [34, 35], as they are reliable, easily characterized and constructed.

The beam has a linear restoring force for small oscillations as well as a nonlinear component for larger oscillations. To reduce the linear component the beam was preloaded. Fixing one end of the beam in a holder, the beam was compressed slightly and then fixed in place. This task required delicate adjustments to achieve a good balance of low linear stiffness while not deforming the beam to an extent that would impede performance.

Performing a few loading trials, the optimal setup for the beam was when the spring favored one side but did not deform greatly. Figure 2.4 depicts a beam normally clamped and a slightly preloaded shape. With the slight bending, the beam could oscillate freely with low damping, but with an unsymmetric restoring force. An

offset from the equilibrium position of more than 0.5 (mm) would cause beam to move in an unsmooth manner, generating a highly nonlinear force but difficult to analyze.

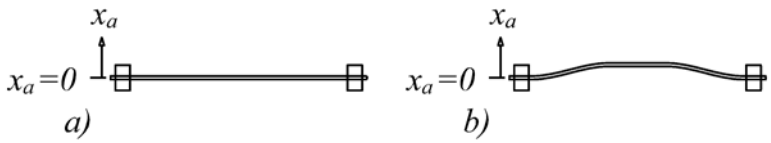

Figure 2.4: Effects of beam preloading; a) normally clamped beam with equilibrium at $x_a = 0$, b) a preloaded beam with equilibrium point at $x_a \neq 0$.

The fixed repelling magnets provide an additional source of stiffness to the NES. By changing the spacing between the fixed magnets and the oscillating ones the restoring force could be dramatically changed, allowing for a variety of potential stiffness. The magnetic force generated between two magnets is given by [36]

$$F_m = \frac{\mu_m}{2\pi d^2} \tag{2.2}$$

where d is the distance separating two magnets, and μ_m is the magnetic constant that depends on the strength of the magnets and the medium in which they operate. From Eqn.(2.2) it can be seen that the force generated is nonlinear with respect to separating distance. The restoring force F_m can also be used to correct for the favoring of the steel beam to one side. Figure 2.5 shows the schematic for the placement of the repelling magnets. Changing distances d_1 and d_2, the force can be altered and the overall stiffness can be balanced and the beam centered.

To balance the forces the following steps was taken. Once the beam was preloaded giving way to an offset in the negative (left) direction, the right magnet was placed at a desired distance d_2. The left magnet was then incrementally moved towards the oscillating magnet reducing distance d_1, until the beam reached a settling equilibrium point of $x_a = 0$. In this manner the forces from the preloaded beam and repelling magnets may be balanced to give symmetric stiffness.

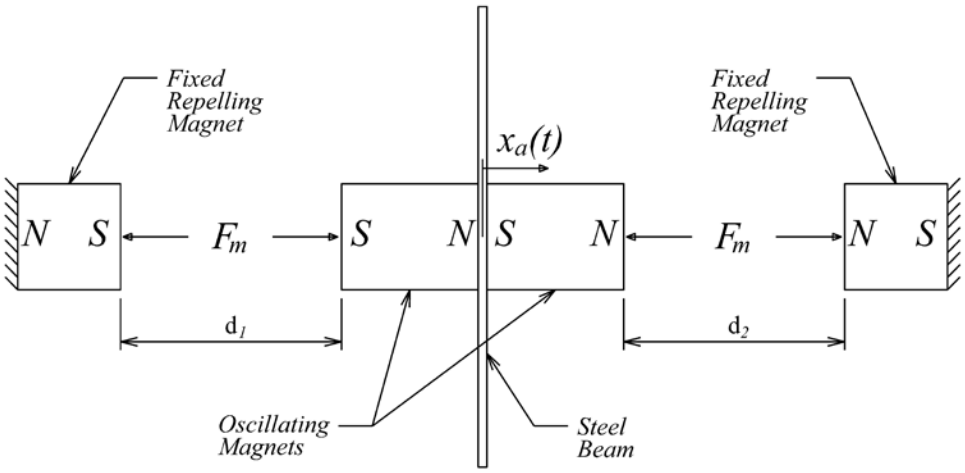

Figure 2.5: Repelling magnet configuration for the NES.

To demonstrate the effectiveness of the design a test was conducted. The repelling magnets were placed at a distance of $d_1 = 30 (mm)$ and $d_2 = 27.7 (mm)$, with the beam resting at a balanced $x_a = 0$. The beam was struck and the oscillations recorded. Figure 2.6 depicts the recorded response and a Wavelet Transform (WT) of the response when the NES was struck with an arbitrary force. Examination of Fig. 2.6(a) reveals two features defined in Section 1.3 as the primary design objectives: 1) the NES has extremely low mechanical damping, having long sustained oscillations and 2) the NES exhibits an essentially nonlinear stiffness, the displacement having a changing frequency. It was also apparent that the restoring forces have been balanced, the system oscillating evenly about the equilibrium point. A WT was applied to the displacement of the signal, Fig. 2.6(b) exposes the essential nonlinearity of the system. For large displacements the system has a high frequency of approximately 11-12 Hz. As the oscillation amplitude decreases the frequency also decreases to approximately 3-4 Hz.

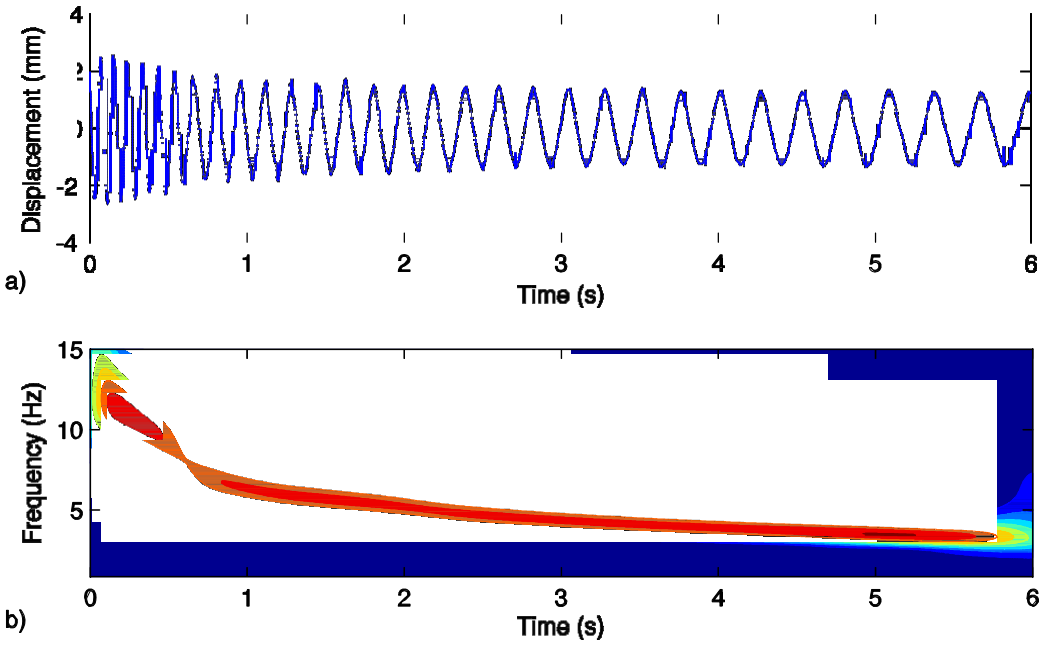

Figure 2.6: Transient response of the NES after being struck; a) displacement b) WT Morlet spectra of response.

From Fig. 2.6 some assumptions about the dynamics performance of a NES can be made. The larger amplitudes at the beginning of the test correspond to the larger amounts of energy present in the system and higher frequencies achieved. As the energy is dissipated through mechanical damping the frequencies likewise decrease. In the region of $0 \leq t \leq 0.75$ seconds there was a sharp decrease in the frequency, whereas for the remainder of the response there was a more gradual decrease in frequency. This change in threshold indicates that there was a dependence on energy level to engage the nonlinear part of the NES, and that performance may depend on the energy present in the system.

2.2.2 Preliminary Equations of Motion

From the previous section it is possible to construct the governing equations of motion for the system. In summary there is a linear base, attached to it is a linear oscillator having a spring-mass-damper configuration. Attached to the primary system is a nonlinear oscillator with low mechanical damping and undetermined restoring forces. The free body diagrams are shown in Fig. 2.7.

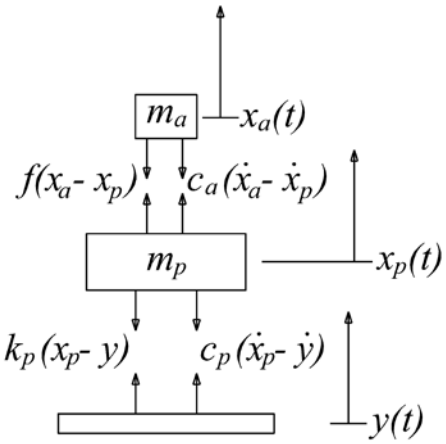

Figure 2.7: Free body diagram of the generalized system.

Using Newton's second law, the equations of motion can be summarized for the combined system:

$$m_p \ddot{x}_p + c_p(\dot{x}_p - \dot{y}) + c_p(\dot{x}_p - \dot{y}) - c_a(\dot{x}_a - \dot{x}_p) - c_a(\dot{x}_a - \dot{x}_p$$

$$) = 0 \qquad (2.3)$$

$$m_a \ddot{x}_a + \text{[illegible]} - c_p \dot{x}_p + c_a(\dot{x}_a - \dot{x}_p) = 0 \qquad (2.4)$$

where m is mass, c damping, k linear stiffness and the subscripts p and a denote the primary system and NES system respectively. The term $c_a(\dot{x}_a - \dot{x}_p)$ repre-
sents the restoring force to be quantified. The physical parameters of the NES are listed in Table 2.1.

Table 2.1: Physical parameters of beam and magnets.

Beam	
Length	480 (mm)
Width	30 (mm)
Thickness	0.52 (mm)
Oscillating magnet	
Mass	0.0305 (kg)
Length	25.4 (mm)

Radius	7.5 （mm）

Type	N40
Fixed magnet	
Length	3 (mm)
Radius	7.5 (mm)
Type	N40

2.3 Energy Harvesting System

The presence of an oscillating mass consisting of magnets opens up the possibilities for energy harvesting. During vibration the magnets will generate a changing magnetic field with respect to a fixed plane, the addition of a fixed coil within the changing field will allow a voltage to be induced in the coil. The proposed energy harvesting method for this thesis is a set of coils consisting of inner and outer radii that will surround the magnets which do not physically touch them as shown in Fig. 2.8. The coils will be connected in series such that the induced voltages will be summed.

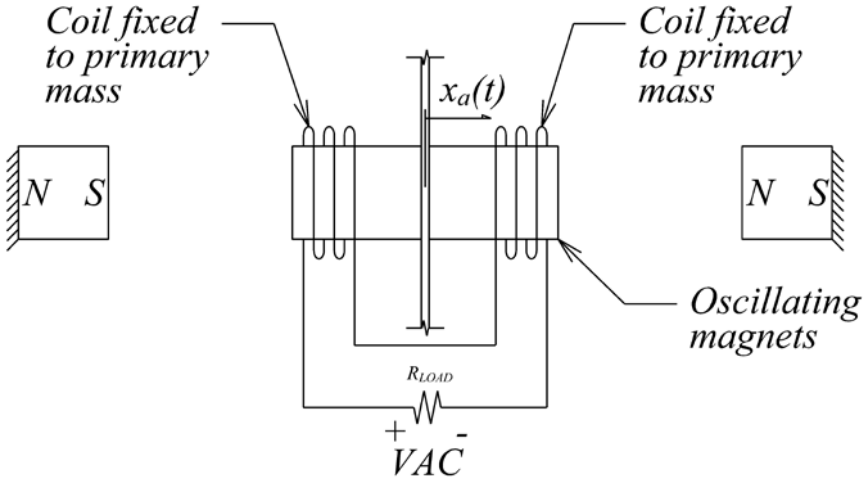

Figure 2.8 Schematic of the proposed energy harvesting configuration.

To determine the effects of the electrical system, and develop an overall model of the NES and energy harvesting, a physical derivation is required to extract the governing coefficients. A simplified model of a single coil and magnet are shown in Fig 2.9. The equation of motion for the system can be expressed by Eqn. (2.5) where $H = ◆◆_a - ◆◆_p$ is the relative displacement between the coil

(fixed

to the primary mass), and the oscillating magnet. The coefficient c_m is the mechanical damping, and the function $f(x)$ is the spring restoring force that includes linear and nonlinear terms shown as k in Fig. 2.9.

$$m_a \ddot{x}_a + c_m \dot{x} + f(x) = 0 \quad (2.5)$$

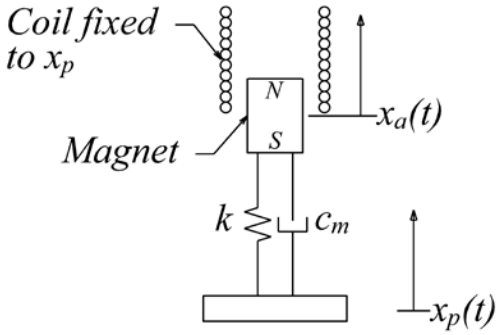

Figure 2.9: Simplified model of an energy harvester

The coils were constructed of enamel coated AWG 30 copper wire tightly wrapped around a High Density Polyethylene (HDPE) spool. The inner diameter of the spool was made large enough to avoid hitting the oscillating magnet. Each coil consisted of 256 turns of wire with a measured resistance of 6 (Ω). The wire was measured to have a 0.3482 (Ω/m) resistance, and the length calculated as 17.23 (m). The physical dimensions of the coil are listed in Table 2.2.

Table 2.2: Coil physical properties

	Coil
Inner radius (r_1)	9.398 (mm)
Outer radius (r_2)	12.98 (mm)
Height (h)	7.498 (mm)
Resistance (R_{coil})	6 (Ω)
Resistance per meter (R') (Ω/m)	0.3482
Turns (N)	256
Wire length (l_{wire}) (m)	17.23

The constructed coils were mounted on post so that they are in line with the magnets and fixed to the primary system as shown in Fig. 2.10. In this configuration the setup will act as an electromagnetic vibration transducer.

Figure 2.10: Image showing the coil arrangement.

To analyze the effects of the electric and mechanical components, a simplified approach was used based on Faraday's law of induction. The law states that any change in magnetic flux through a conductive loop of wire will cause a voltage to be induced in the wire. This induced voltage is the so-called electromotive force (EMF) which is given by:

$$\varepsilon = \oint_{wire} (v \times B) \cdot dl \qquad (2.6)$$

where v is the relative velocity between the coil and the oscillating magnet, B is the magnetic flux density generated by the magnet, dl is length of the wire coming rising the coil and $\times$ signifies the cross product, while the operator $\cdot$ denotes the dot product. Figure 2.11 depicts the single wire coil and magnet and the coordinates used to describe the velocity and magnetic field. The unit vectors in cylindrical coordinates are $\hat{r}$, $\hat{z}$ and $\hat{\beta}$ and point in the positive direction. In the diagram
the coil is considered to be moving towards the magnet and having a negative velocity, which is equivalent to the magnet moving towards a fixed coil. The radius of the coil is r and the distance separating the center of the magnet to the coil is H. The angle β is used later in an integration step and is used as an arbitrary reference frame.

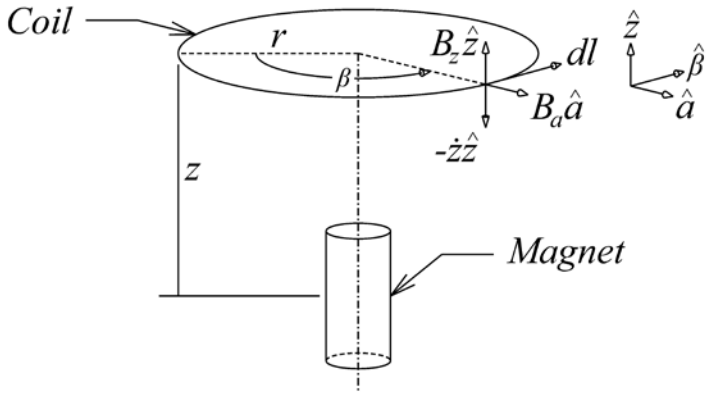

Figure 2.11: Diagram of single coil and magnet.

Due to the symmetry of the cylindrical magnet, only two components of the magnetic flux density are applied, B_a in the a-direction (radial component) and B_z in the z-direction (axial component). Using Fig.2.1 the velocity and magnetic field can be broken down into the directional components and combined into Faraday's law.

$$v = -\dot{z}\hat{z} \tag{2.7}$$

$$B = B_z\hat{z} + B_a\hat{a} \tag{2.8}$$

$$\varepsilon = \oint (-\dot{z}\hat{z}) \times (B_z\hat{z} + B_a\hat{a}) \cdot \hat{\beta}\, dl = -\oint B_a\, dl \tag{2.9}$$

Apparent from Eqn.(2.9), the only magnetic field component responsible for inducing a voltage is the radial component B_a. The magnitude of B_a at a point of interest is dependent on the strength of the magnetic material and the location in the z-a plane. The radial magnetic field can then be written as a function of distances:

$$\varepsilon = -N\pi B_a(r, z)\, r \tag{2.10}$$

The integral term in Eqn.(2.10) is the so-called transduction factor. This term is direct coupling between the mechanical and the electrical systems. This term will be used throughout this work and will be designated for one coil as:

$$\text{transduction factor} = -\int_{l_w} B_a \quad (2.11)$$

One can then rewrite the coupling factor such that:

$$\text{transduction factor} = -\int B_a(\quad \frac{1}{l_w}\int_{l_w} B_a(\quad\quad)\quad l_w \quad (2.12)$$

It can be seen that the parenthesized term is an average of the radial flux density over the length of the loop coil. For a coil consisting of multiple loops which are perfectly wound, the average can be approximated as the average of B_a over the area of the coil [37].

$$\text{transduction factor} = -\frac{1}{l_w}\int_{l_w} B_a(\quad\quad)\quad l_w = \frac{1}{A}\int_{A_{coil}} B_a(\quad\quad)\quad l_w \quad (2.13)$$

$$\text{transduction factor} = -\bar{B}_a(\quad\quad)l_w \quad (2.14)$$

where $A_{coil} = (r_2 - r_1)h_{coil}$

The transduction factor can be then shown in reduced form where $\bar{B}_a$ represents the average radial flux density through the cross section of coil. The magnet and the coil will consist of fixed physical parameters, because the coil will only change in the z direction the transduction factor can be reduced in terms of relative displacement:

$$\text{transduction factor} = -\bar{B}_a(\quad)l_w \quad (2.15)$$

Illustrated in Fig. 2.8, the system is comprised of two magnets and two coils, and they are connected in such that the induced voltages are summed. The different coupling factors will be noted by the subscripts 1 and 2. The two coils will be placed in series with a potentiometer that will act as a load. The circuit is shown in Fig. 2.12. R_{coil} is the resistance in a single coil, L_{coil} is the inductance of a coil, $i(t)$ is the time varying current in the circuit, R_{load} is the load resistor and $k_{t1,2}$ are the transduction factors from each coil respectively.

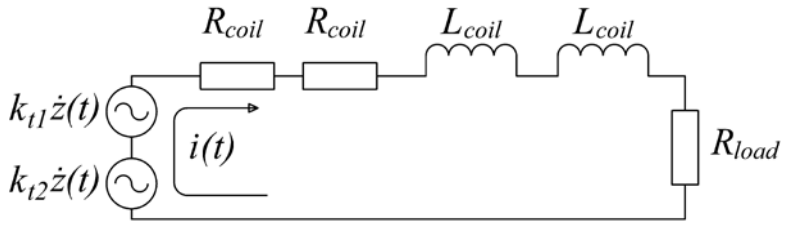

Figure 2.12: Electrical system

With an induced voltage in the electrical circuit, current will flow. For this system the inductance and resistance form the coils can be summed and Kirchoff's law applied to derive the electrical system equations:

$$2L_{coil}\frac{di}{dt} + (2R_{coil} + R_{load})i = k_t\dot{z} \tag{2.16}$$

$$k_t = k_{t1} + k_{t2} \tag{2.17}$$

where the transduction factor k_t is the total transduction factor for the two coils k_{t1} and k_{t2}.

Generally for an AC electrical circuit the inductance of the coil will play a significant role. The alternating current will cause the coil to have a reactance, along with the static resistance generating an impedance. The impedance of the coil can be defined by the complex equation:

$$Z_{coil} = R_{coil} + jX_{L_{coil}} \tag{2.18}$$

The inductance of the considered coils can be estimated according to the Wheeler approximations given by [38]:

$$L_{c\square\square\square} = \frac{3.15 \cdot 10^{-5} \square\square^2 N}{6R_m + 9h_{c\square\square\square} + 10(r_2 - r_1)} \quad (2.19)$$

$$\square\square_m = \frac{1}{2}(r_2 + r_1) \quad (2.20)$$

where N is the number of turns of the coil, $r_{1,2}$ are the inner and outer coil radii and $h_{c\square\square}$ is the height of the coil. The approximated inductance for a single coil was $1.52\,mH$. For the test apparatus the maximum driving frequency will be 25 Hz. Using this upper frequency limit the total reactance can be determined:

$$\square\square_{\square\square\square\square\square\square\square\square} = 2\square\square(25)(2L_{c\square\square\square}) = 0.477\,\Omega \quad (2.21)$$

The reactance accounts for less than 5% of the total resistance in the coils. For simplification of the electrical equations, the coil inductance will be neglected by setting $L_{c\square\square} = 0$. Rearranging Eqn.(2.16) the equation for current can be determined and expressed:

$$i = \frac{\square\square}{\frac{t}{2\square\square_{\square\square\square\square} + \square\square_{\square\square\square\square}} + \square\square} \quad (2.22)$$

The final step in the derivation is to apply Lenz's law. The law states that for a closed circuit condition the EMF voltage produced in the coil will cause a current to flow. This current will create a magnetic field which opposes the magnetic field that caused the current. This interaction causes a feedback electromechanical force which is given by:

$$F_w = \square\square_t i \quad (2.23)$$

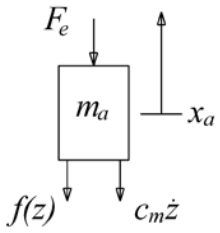

Figure 2.13: Free body diagram of all forces acting on the oscillating magnet.

Figure 2.13 depicts all of the forces acting on the vibrating magnets, and applying Newton's 2nd law of motion the equation of motion can be defined as:

$$m_a\ddot{z}_a + c_m\dot{z} + kz + F_w = 0 \tag{2.24}$$

Combining Eqns.(2.22)-(2.24) the equation of motion for the relative displacement of the absorber can be described in terms of the mechanical restoring forces as well as the electrical restoring forces:

$$m_a\ddot{z}_a + c_m\dot{z} + \frac{k_t^2}{k(R+2R)}\dot{z} + kz = 0 \tag{2.25}$$

It is clear from Eqn.(2.25) that there are two velocity coefficients, resulting in two damping parameters. The first, c_m, is the mechanical damping, and the second c_w is the electrical damping. The value of the electrical damping coefficient is dictated by the transduction factor as well as the total resistance in the coil and load.

$$c_w = \frac{k_t^2}{2R_{coil} + R_{load}} \tag{2.26}$$

$$m_a\ddot{z}_a + (c_m + c_w)\dot{z} + kz = 0 \tag{2.27}$$

The voltage and the power across the resistor can be found by again applying Kirchoff's Laws to Fig.2.1 such that:

$$V_{\text{[illegible]}al} = \frac{\text{[illegible]}}{\text{[illegible]}} \tag{2.28}$$

$$\text{[illegible]}_{\text{[illegible]}al} = 2R_{al} + R \tag{2.29}$$

$$P_{\text{[illegible]}al} = \text{[illegible]}^2 \frac{\text{[illegible]}}{(2\text{[illegible]} + \text{[illegible]})^2}\text{[illegible]}^2$$

$$\text{[illegible]}_{\text{[illegible]}al} =$$

2.4 Conclusion

The overall system has been described in terms of the mechanical system as well as the electrical one. From the derivation of the energy harvesting system it was seen that the coupling factor k_t is the direct link between the two systems. The transduction factor is also the method used to determine the electrical damping for the NES, and can be used to determine the current voltage and the power generated. Combining Eqns.(2.3),(2.4),(2.22)and (2.26) a complete model of the system can be defined.

$$m_p\text{[illegible]}_p + \text{[illegible]}_p(\text{[illegible]}_p - \text{[illegible]}) + \text{[illegible]}_p(\text{[illegible]}_p - \text{[illegible]}) - \text{[illegible]}(\text{[illegible]}_a - \text{[illegible]}_p) - \text{[illegible]}_m(\text{[illegible]}_a - \text{[illegible]}_p) - \frac{k_t^2}{2\text{[illegible]}_{cl} + \text{[illegible]}_{al}}(\text{[illegible]}_a - \text{[illegible]}_p) = 0 \tag{2.30}$$

$$m_a\text{[illegible]}_a + \text{[illegible]}_a - \text{[illegible]}_p + \text{[illegible]}_a(\text{[illegible]}_a - \text{[illegible]}_p)) - \frac{k_t^2}{2R_{al} + \text{[illegible]}_{cl}}(\text{[illegible]}_a - \text{[illegible]}_p) = 0 \tag{2.31}$$

$$i = \frac{\text{[illegible]}}{2\text{[illegible]}_{cl} + \text{[illegible]}_{al}} \tag{2.32}$$

Chapter 3

System Parameter Identification

3.1 Primary System Parameters

To determine the parameters of the primary system a traditional method was employed. The magnets and primary mass were removed from the system and weighed individually. The mass of the primary system was determined to be $m_p = 0.917$ (kg). The structure was reassembled without the NES mass and the base locked. The primary structure was then struck and set into free vibration. The response was recorded and a Fast Fourier transform (FFT) applied. Figure 3.1(b) shows the response and the FFT. The natural frequency of the system was determined to be 11.6 (Hz). For a linear system the stiffness of the spring can be determined by:

$$k_p = \omega_p^2 m \tag{3.1}$$

This results in a stiffness of $k_p = 4870$ (N/m). To determine the damping coefficient, the positive peaks from the recorded response were determined and the logarithmic decrement method used [6].

$$\delta = \frac{1}{n} \ln \left(\frac{x(t)}{x(t+n)} \right) \tag{3.2}$$

n

$$\xi = \frac{\delta}{\sqrt{4\pi^2 + \delta^2}} \tag{3.3}$$

where $x(t)$ is a positive peak, $x(t + n\tau_d)$ is any integer number of successive peaks and ξ is the damping ratio. The damping ration for the primary system was found to be approximately 1.03 percent.

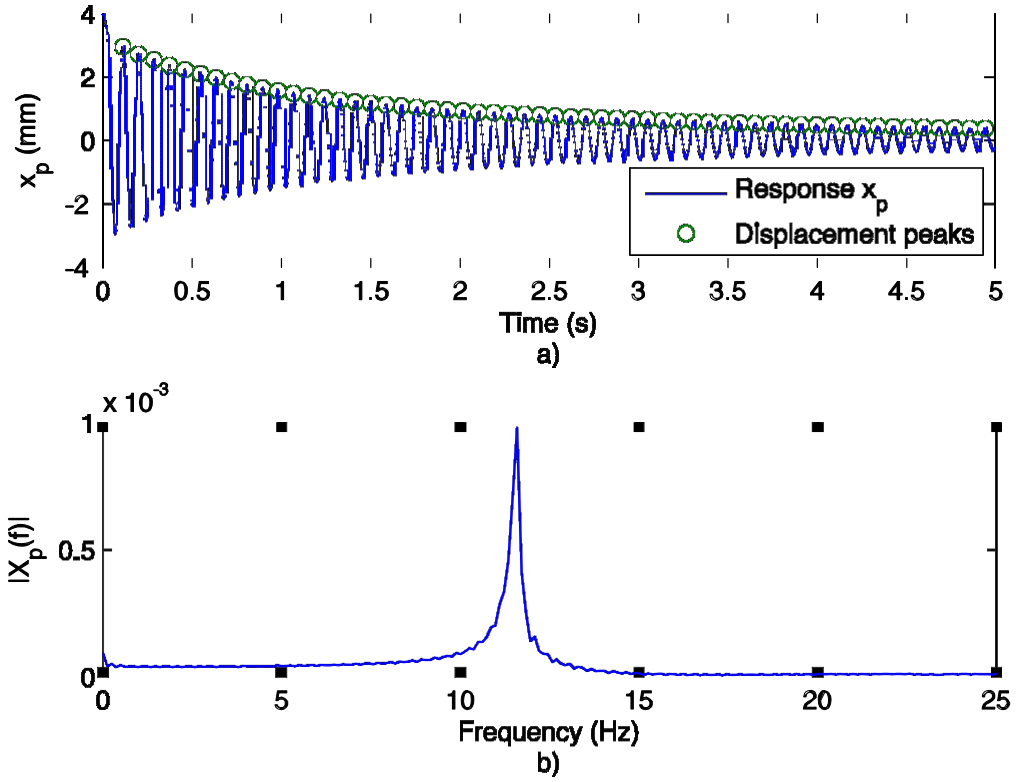

Figure 3.1: a) recorded free response of primary system with fitted damping curve, b) FFT plot of response with $m_p = 11.74$

$(H$

The damping coefficient is then determined using Eqn.(3.4), is approximately $c_p = 1.3747\ (N s/m)$. All of the determined primary system parameters are listed
in Table 3.1.

$$c_p = 2\zeta\omega_n m_p \tag{3.4}$$

Table 3.1: Estimated primary system parameters

Parameter	Estimated value
m_p	0.917 (k)
k_p	4870 ($^{-1}$)
$$	1.3747 (N^{-1})
$$	11.6 (H)

3.2 Transduction Factor – Electrical Damping Coefficient

In Section 2.3 the transduction factor k_t which couples the mechanical and electrical systems was derived. The remaining component is to calculate the radial magnetic flux average over the area of the cross sectional area of coil. To perform this calculation the finite element method is used to determine the radial magnetic flux for the magnet.

$$B_a = \frac{1}{A} \int_{A} B_a(r, z)\, dA \qquad (3.5)$$

Illustrated in Fig. 2.9, the system has two magnets in line attached to the beam in attractions. This model can be simplified by considering a single magnet of length 2. The magnet was modeled using the free commercially available soft-
ware FEMM [39], using the axis symmetric orientation for models in cylindrical coordinates. The results were imported to Matlab for analysis. Figure 3.2 shows the results of the FEMM results for the magnets.

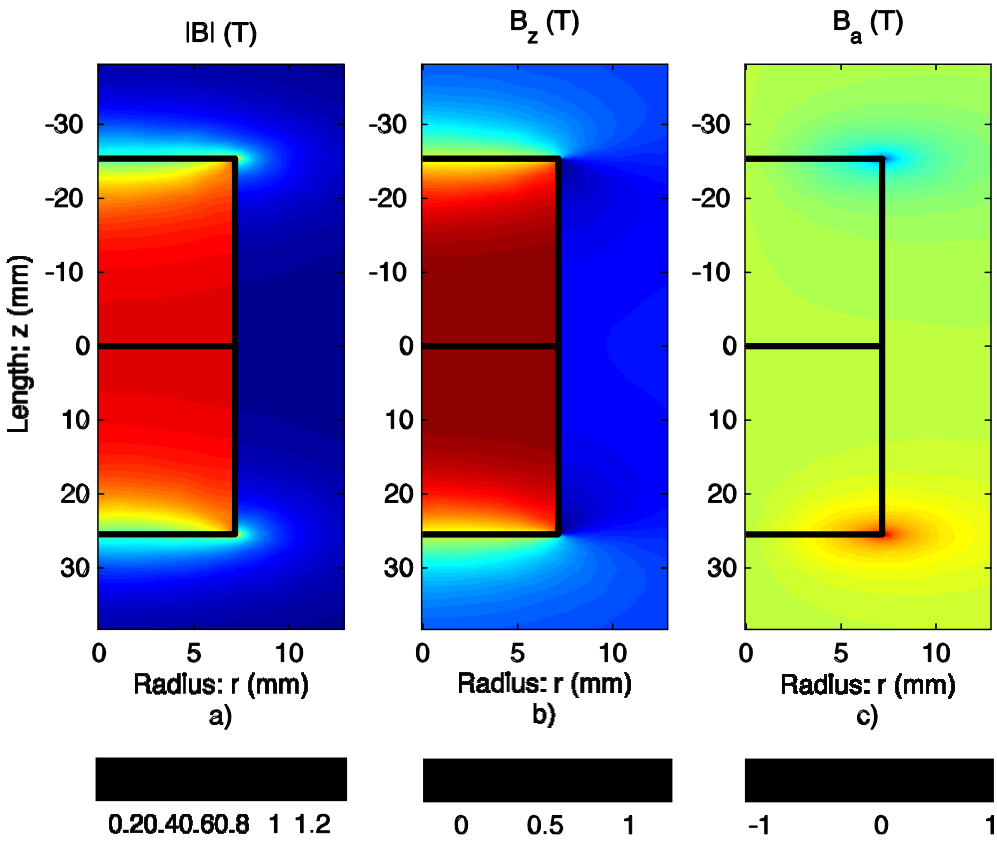

Figure 3.2: FEMM analysis results: a) magnitude of flux density b) axial component of the flux density c) radial component of the flux density. Black boxes signify the outer dimension of the magnets.

To evaluate the average radial flux density through a single coil, a separation distance S was defined as the distances from the center of the two magnets to the center of a coil shown in Fig. 3.3(a). The only magnetic field components of concern are the radial components shown in Fig. 3.2(c). From this data, the only portions that will induce a voltage in the coil lie within the area of the coil the entire length of H was created lying within the bounds of r_1 and r_2 and are shown in Fig. 3.3(b). It can be seen that there are two peaks (maxima and minima) that occur over the length of ◆◆, corresponding to the ends of the magnets. ◆◆◆

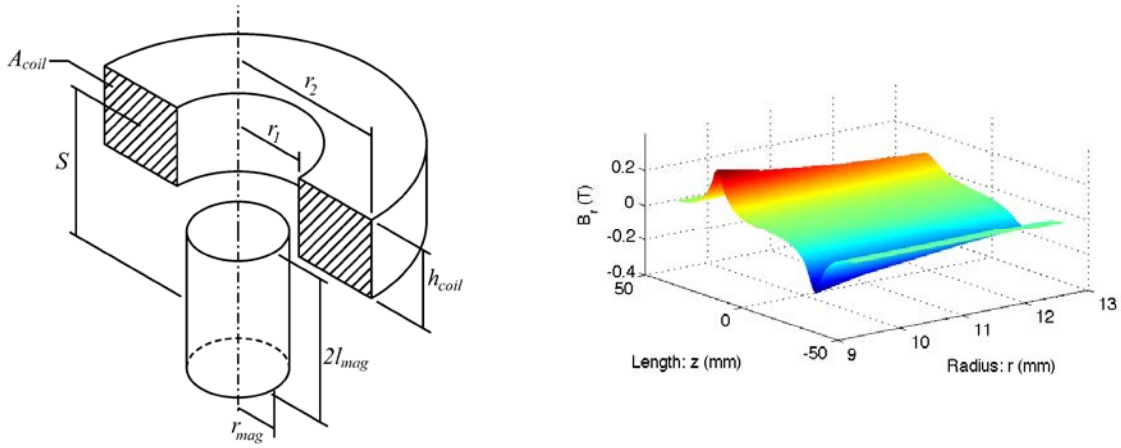

a) b)

Figure 3.3: a) diagram of coil and magnet, b) B_a data within the region of $r_1 - r_2$ over the length of magnet.

The magnetic flux was numerically integrated over the area of the coil at discrete distances of S over the entire length of l_w. Averaging of the discrete areas and multiplying by length of the wire gives the transduction factor for separation distance S.

$$k_{v1}(S) = -\frac{l_{wire}}{A_{coil}} \int_{r_1}^{r_2} \int_{S-\frac{h_{coil}}{2}}^{S+\frac{h_{coil}}{2}} B_a(z, r)\, dz\, dr \qquad (3.6)$$

$$z_1 = S - \frac{h_{coil}}{2}, \qquad z_2 = S + \frac{h_{coil}}{2} \qquad (3.7)$$

The results of the numerical integration for the entire length of the two magnets are presented in Fig. 3.4(a). The transduction factor reaches a maximum value of approximately $k_{max} = 5.4\ V/m/s$ when the coils are at equilibrium of $H = 0$. As mentioned previously, the coils will be connected such that the induced voltages will be summed, and due to the symmetry of the curves the value for $k_v = k_{v1} + k_{v2} = 2k_{v1}$, depicted in Fig. 3.4(b) for the full range of motion of S.

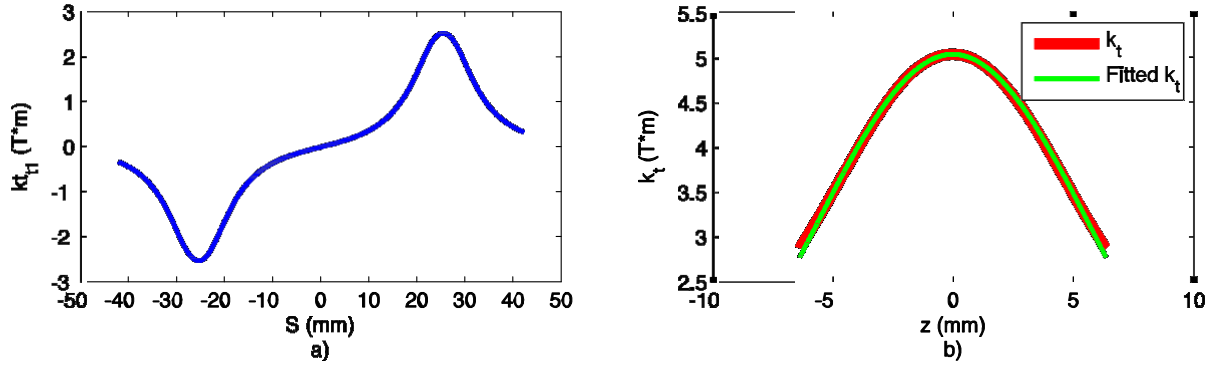

Figure 3.4: a) transduction factor k_{t1} for a single coil. b) total transduction factor k_t and the fitted data of for the data.

The data for k_t was fitted using an exponential function and was overlaid the in Fig. 3.4(b) with good agreement and can be expressed as Eqn.(3.8) with a maximum of $k_t = 5.03(n \cdot m)$.

$$k_t(z) = ae^{bz^2} \tag{3.8}$$

$$\begin{aligned} a &= 5.029 \\ b &= -1.474 \times 10^4 \end{aligned} \tag{3.9}$$

3.3 Nonlinear Stiffness and Damping

As discussed in the previous sections, there were two components generating the restoring force for the NES: 1) the preloaded beam and 2) the collinear repelling magnets. The reasoning behind this configuration was to be able to change the nonlinear stiffness of the absorber by changing the distance between the fixed and oscillating magnets. This concept was used by [32], where repelling magnets were used to generate all of the restoring force. The effects of the magnets and beam will be examined individually.

3.3.1 Effect of Repelling Magnets.

To understand the effects of the restoring force created by the magnets, a series of static tests measuring the force generated between the magnets were conducted. One oscillating magnet was placed in a holder connected to a S-type load cell which was fixed rigidly to ground. One repelling magnet was place inline separated by distance d_0, shown in Fig. 3.5.

a)

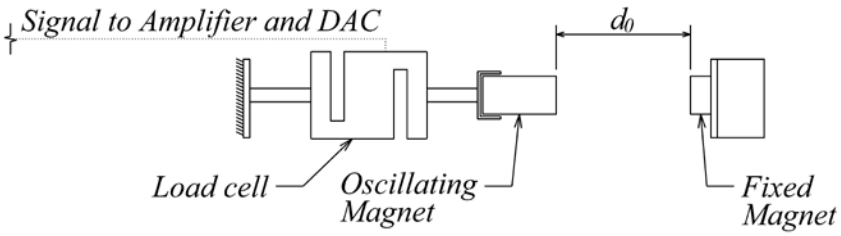

b)

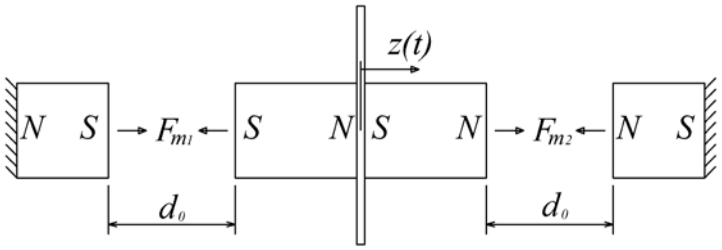

Figure 3.5: a) static test arrangement for determining force displacement relationship, b) force diagram of magnet arrangement.

The force and displacement measurements were recorded and fitted to the exponential function Eqn.(3.10) and is shown in Fig. 3.6(a). The nonlinear force generated by the magnets can be clearly seen, becoming more pronounced as d_0 decreases. Considering Fig. 3.5, the total magnetic restoring force F_m for symmetric magnet spacing can be expressed as the sum of forces. The total force for different magnet spacings are shown in Fig. 3.6(b).

$$F_{mag}(x) = ce^{dx} \tag{3.10}$$

$$\begin{aligned} c &= 0.0001647 \\ d &= -2.174 \end{aligned} \tag{3.11}$$

$$F_m(x) = F_{m2}(x) - F_{m1}(x) = c(d_l - x)^l - c(d_l + x)^l \tag{3.12}$$

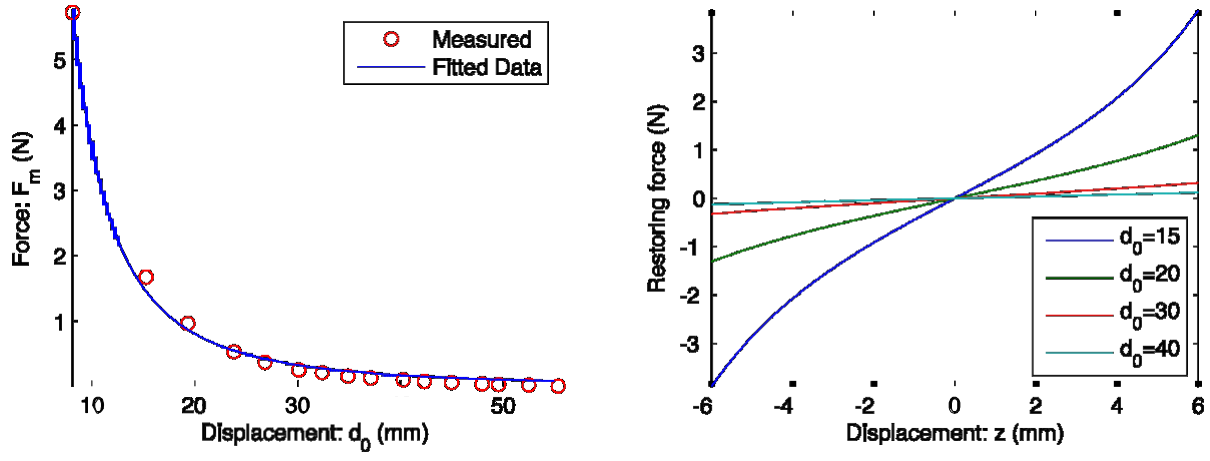

Figure 3.6: a) magnetic force displacement measurements and fitted data, b) total force displacement relationship for different magnet spacings.

Recalling the definition for an effective NES, the design goal was to reduce or eliminate the presence of a linear restoring force, Fig. 3.6(b) shows that for the displacement range in H, the main contributing component of the magnetic restoring force is linear. Although the force is nonlinear over large displacement ranges, for this design reducing the distance d_0 to increase the nonlinearity results in a significant linear stiffness component. Therefore the magnets will be used solely to balance the forces from the preloaded beam, and will be placed at the furthest distance possible from the oscillating magnets. The optimal distance was found to be approximately $d_0 = 40\ (m\text{}).$

3.3.2 Beam Nonlinear Stiffness and Damping

The identification of the stiffness and damping of the NES system will use the commonly employed restoring force method [40, 41]. The restoring force method is an application of Newton's second law from the force diagram of Fig. 2.7 for the NES such that

$$m_a\text{} + \text{}_a - \text{}_p, \text{}_a - \text{}_p\text{} = 0 \qquad (3.13)$$

$$\text{}(\text{}, \text{}) = -m_a\text{}_a \qquad (3.14)$$

Recalling the relative displacement as $H = ◻◻_a - ◻◻_p$, the force can be equated in terms of relative displacement and velocity and NES acceleration with the knowledge of absorber mass. The system can be excited and the time histories for displacement recorded to determine velocity and acceleration in ◻◻ and H at regular sampled intervals, spaced Δt. Denoting the sampled displacements, velocities and accelerations as ◻◻$_k$ = ◻◻(◻◻$_k$), ◻◻$_k$ = ◻◻(◻◻$_k$)… where ◻◻$_k$ is the ◻◻th sampling instant such that ◻◻$_k = (k-1)\Delta$◻◻. Thus one can find the restoring force at each time sample ◻◻$_k$.

$$◻◻(◻◻_k, ◻◻_k) = -m_a ◻◻_{a_k} \tag{3.15}$$

For each of the sampled points ◻◻$_k$ there now is a triplet of data of forces for the NES system. Using a simple method outlined by [42], the force data can be mapped to the phase plane. The phase plan is then divided into small grid squares, and the forces lying within the square are averaged to give a force at the center of the grid square. If a grid square has no force values but has three or more neighboring force values, the average of the neighbors are used for the empty grid square. The process is repeated until no new grid squares are produced. This produced an average force map in the phase plane for the NES, which can be fitted using least squares procedures.

There are two critical requirements for the accuracy of this method, the selection of a way to excite the system and the calculation of the velocity and acceleration data. The excitation signal should be selected such that the phase plane has very good coverage [43]. Also being aware of the system general dynamics, one should select the excitation such that it forces the expected nonlinear phenomenon. Knowing that a NES can exhibit a strongly modulated response, a slowly modulated periodic signal will be used to excite the base. The frequency of the periodic signal was selected to be 14 Hz, close to the natural frequency of the primary system, but increased enough so as to not be dominated by the primary response. The slowly modulated response will ensure that the phase plane will have excellent coverage. The selected excitation signal is:

$$\text{[illegible]}(\text{[illegible]}) = Y\cos(0.1\text{[illegible]}) \cdot \cos(14 \cdot (2\text{[illegible]})) \quad (3.16)$$

The displacements of the system were recorded through the laser reflex sensors, meaning that the velocity and accelerations must be differentiated from the time data. The differentiation of recorded displacement signals are very susceptible to noise, being amplified with each differentiation. To filter the signals, the displacement responses are interpolated using cubic spline approximations for simplicity in Matlab®. Cubic spline interpolation was selected to make the data points continuous, allowing for good differentiation. The energy harvesting system allows for verification of the filtering, since the recorded voltage data is directly related to the relative velocity. The differentiated velocities are compared to the recorded voltage, and the degree of cubic smoothing adjusted for a good fit.

To identify the nonlinear stiffness and the mechanical damping of the NES system, the coils are removed from the range of motion of the oscillating magnets. The system was excited for 200 seconds to insure a good representation of the force and to provide good coverage in the phase plane. Figure 3.7 shows the results from the surface force mapping.

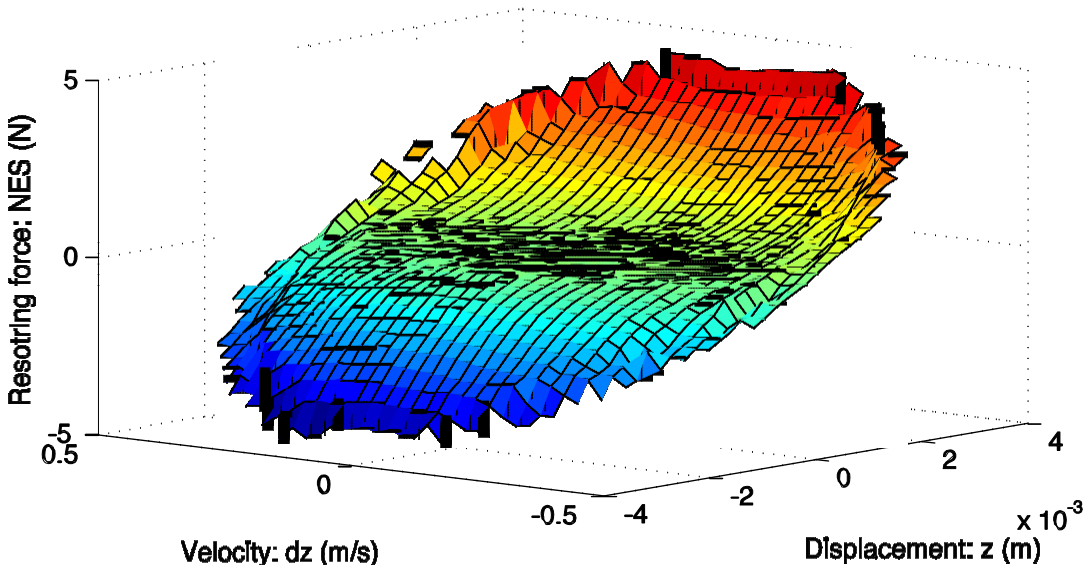

Figure 3.7: Surface force map for the NES in the phase plane.

The results of the force surface map reveal the nature of the nonlinear stiffness generated by the beam. It can be seen that the choice of the exciting signal

provided a representation in the phase plane. It is clear that the beam provides a nonlinear stiffness, the force increasing dramatically as displacement increases. The NES also exhibits low mechanical damping, the force along the velocity axis being generally flat. To have a better understanding of the force displacement-velocity relationships, the curves are examined at (0) for displacement and $(0,)$ for the velocity. At these points the force will be purely due to either displacement or velocity.

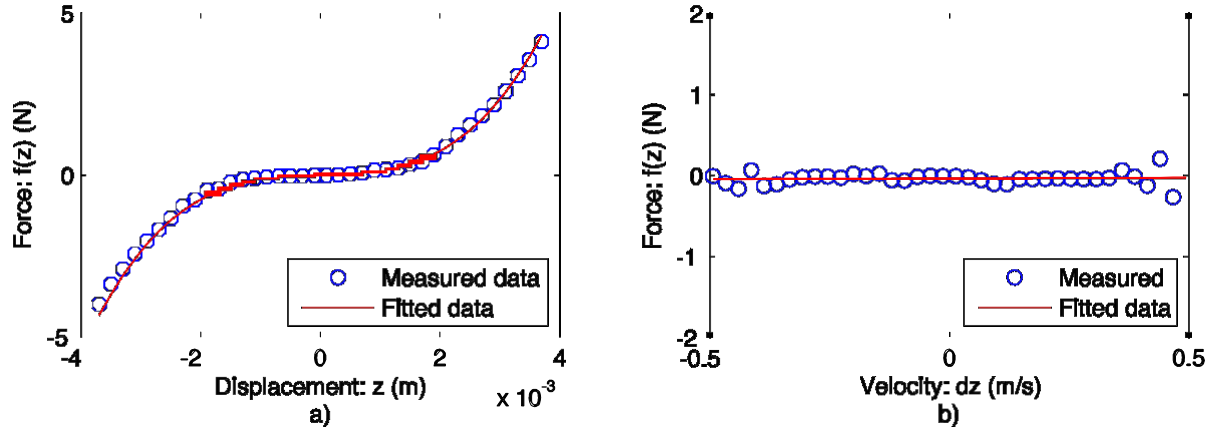

Figure 3.8: a) NES: force-displacement relationship at (0), b) NES: force-velocity relationship at $0,$

$$$$

Figure 3.8(a) depicts the force-displacement relationship for the NES at $= 0.$ It can be seen here that the constructed NES exhibits the desired design goals; that the NES stiffness would be essentially nonlinear. Within the region of $H = \pm 1.5\ (m)$ the curve is almost flat, indicating a very low linear stiffness, critical component for an effective vibration absorption. For larger displacements the restoring force increases quickly exhibiting a high degree of nonlinearity. Figure 3.8(b) illustrates that the NES has an extremely low damping coefficient, another critical design goal.

The nonlinear restoring force and damping were estimated using least squares parameter estimation. The restoring force was related to Eqn.(3.17), to provide for greater fit flexibility [44], where k_a is the NES linear stiffness, k_α is the nonlinear stiffness and α is the degree of nonlinearity. The damping related to Eqn.(3.18) where c_m is the mechanical damping of the NES.

$$\text{[illegible]}(\text{[illegible]}0) = \text{[illegible]}_a H + \text{[illegible]}_n \cdot \text{sign}(\text{[illegible]}) \cdot |\text{[illegible]}|^{\alpha} \quad (3.17)$$

$$\text{[illegible]}(0, \text{[illegible]}) = \text{[illegible]}_{\text{[illegible]}m} \text{[illegible]} \quad (3.18)$$

The obtained values from the curve fitting are listed in Table 3.2. The results of the parameter estimation fit are overlaid in Fig. 3.8, and show good correlation. It is interesting to note that the NES contains a linear component. Although it is an undesirable for a NES, the low value such that $k_a \ll k_p$ indicates that the NES and the primary system will be weakly coupled. The linear natural frequency for the NES can be calculated as $\text{[illegible]}_{a_{lcn\text{[illegible]}a\text{[illegible]}}} = \overline{\text{[illegible]}k_a/m_a}$,

approximately
4.59(Hz). This value corresponds to the frequency displayed in the WT plot of the NES free response in Fig. 2.6 for small displacements. The degree of nonlinearity [illegible] is also very close to a cubic approximation, an aim of the overall design.

Table 3.2 Estimated parameters of NES identified using restoring force surface method

Parameter	Estimated Value
m_a	0.061 (k[illegible])
k_a	50.81 ([illegible]/[illegible])
k_n	9.539×10^7 ([illegible]/[illegible]$^{3.027}$)
α	3.027
[illegible]$_{\text{[illegible]}m}$	0.017 (N[illegible]/[illegible])

The restoring force surface method can be extended to multiple degrees of freedom systems [45]. Applying this extension to the primary system will allow for verification of the method. Applying Newton's second law to the primary system and noting $w = \text{[illegible]}_p - y$ as the relative displacement between the base and primary mass, the same procedure can be applied.

$$m_p \text{[illegible]}_p + \text{[illegible]}_p - \text{[illegible]}_p \text{[illegible]}_p - \text{[illegible]} - \text{[illegible]}_a - \text{[illegible]}_p, \text{[illegible]}_a - \text{[illegible]}_p \text{[illegible]} = 0 \quad (3.19)$$

$$\frac{d}{dt}(m\dot{w}) = -m_p g_p + \frac{d}{dt}(m\dot{w}) \quad (3.20)$$

Evident in Fig. 3.9, the restoring force surface method produced a very linear stiffness and damping for the primary system, generating a flat disc shape surface. As with the NES the stiffness is fitted with least squares parameters, with an estimated linear stiffness of $k_a = 4910(\text{N/m})$. The estimated value has a 0.82% error from the previously calculated value from section 3.1, evidence of the accuracy for the restoring force surface method.

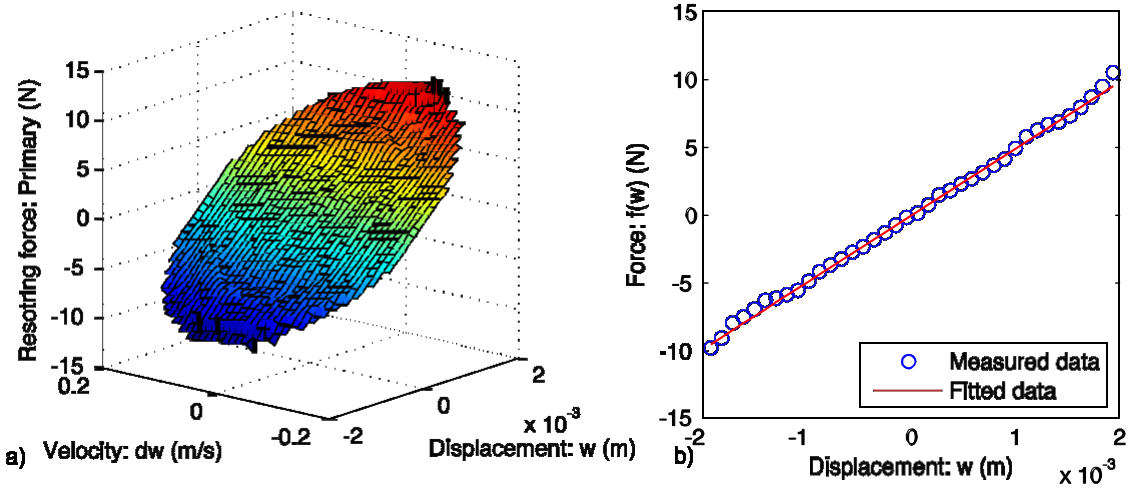

Figure 3.9: Primary system: a) Surface force map of the primary in the phase plane, b) force-displacement relationship at $\dot{w} = 0$.

3.3.3 Electrical Damping

The above method can also be used to determine the validity of the estimation of the transduction factor found through the FEM estimation. Two tests were conducted with different load resistances. The first $R_{load} = 10(\Omega)$, will apply a large amount of damping and the second $R_{load} = 50(\Omega)$, a moderate amount of damping. The damping coefficient will be found using the restoring force method, and by re-arranging Eqn. (2.26), one can find the approximate for the electromechanical coupling in terms of damping [46].

$$\zeta_t = \frac{k_a}{2(\omega_a - \omega_{am})\omega_{load}} - \zeta_{load} \tag{3.21}$$

Figure 3.10 shows the results from a load resistance of $10\,\Omega$. The damping coefficient was found to be fairly linear with an approximate value of ζ_a

=

$1.136\ (N\text{••}/\text{••})$. Using Eqn. (3.21) the approximate transduction factor is $k_t = 4.9617\ (n \cdot \text{••})$, very close to the predicted maximum value of 5.03. The results for the load resistance of $50\ (\Omega)$, shown in Fig. 3.11, have a calculated damping of $\text{••}_a = 0.4231\ (N\text{••}/\text{••})$. The approximate transductionfactor is $k_t = 5.0178\ (n \cdot \text{••})$, again very close to predicted value.

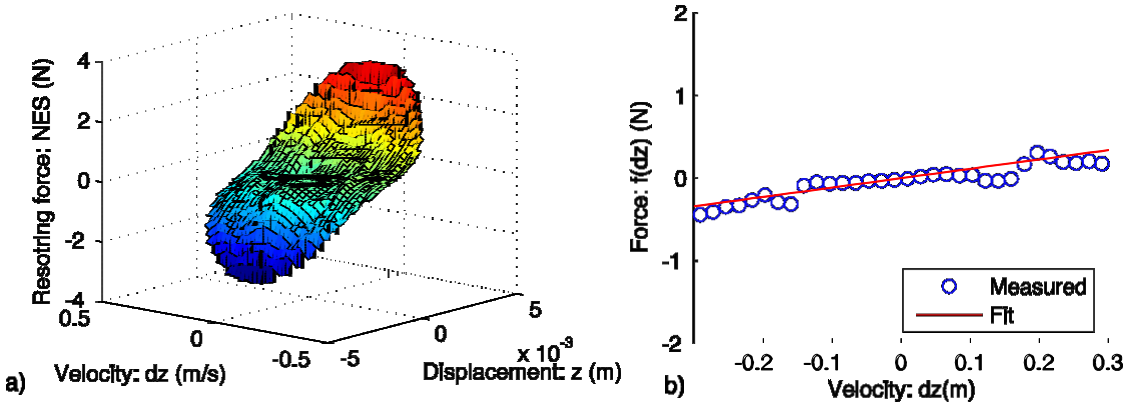

Figure 3.10: NES with load resistance of $10(\Omega)$; a) Surface force map of the primary in the phase plane; b) force-velocity relationship at $\text{••}(0, \text{••})$.

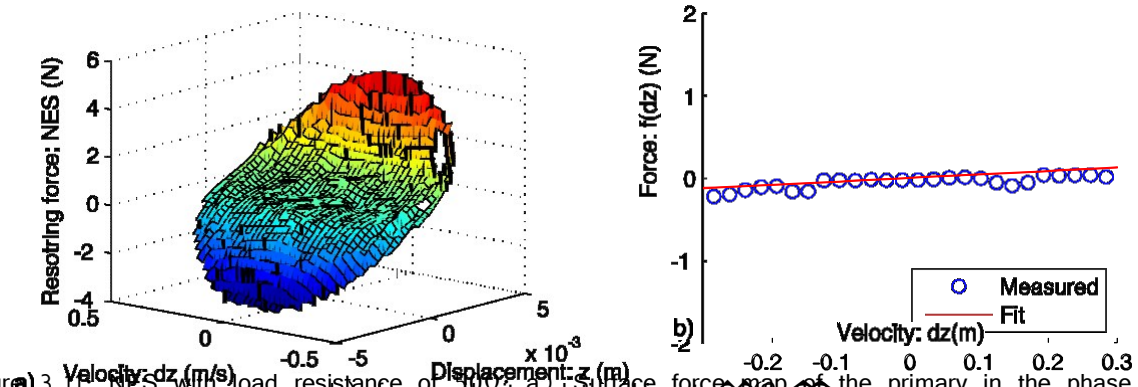

Figure 3.11: NES with load resistance of $50(\Omega)$; a) Surface force map of the primary in the phase plane; b) force-velocity relationship at $\text{••}(0, \text{••})$.

This analysis makes a large assumption in the verification of the transduction factor; that the Lorentz force applied to the system is linear. This is contradictory to the nonlinear coupling calculated in Section 3.2, which should be a function to the displacement ••. It is important to note that the displacement and velocity of

the

absorber are 90 degrees out of phase from each other. This implies that when the displacement magnitude is at a maximum the velocity magnitude is at a minimum. The lower values of k_t corresponding to large displacements, will have little effect due to the low velocity component. Therefore the damping will be dominated by the higher values of k_t where the displacement is small but the velocity is high. It stands to reason then that the transduction factor can be made linear and approximately the value of the maximum value of k_t.

To further explore this, the restoring force surface method can be modified for the recorded voltage time series. Here instead of Newton's second law, one can apply Kirchoff's Law from Eqn.(2.28) such that:

$$\frac{V_{\blacksquare\blacksquare\blacksquare\blacksquare al}(2\blacksquare\blacksquare_{\blacksquare\blacksquare\blacksquare\blacksquare} + \blacksquare\blacksquare_{\blacksquare\blacksquare\blacksquare\blacksquare al})}{\blacksquare\blacksquare_{\blacksquare\blacksquare\blacksquare\blacksquare al}} = \blacksquare\blacksquare(\blacksquare\blacksquare) \tag{3.22}$$

In this way the left hand side of Eqn.(3.22) represents the EMF voltage induced within the coil. The voltages are mapped and plotted over the relative velocity in Fig. 3.12. It is apparent that the relationship is linear, more importantly the slope of this line is an approximate value for k_t.

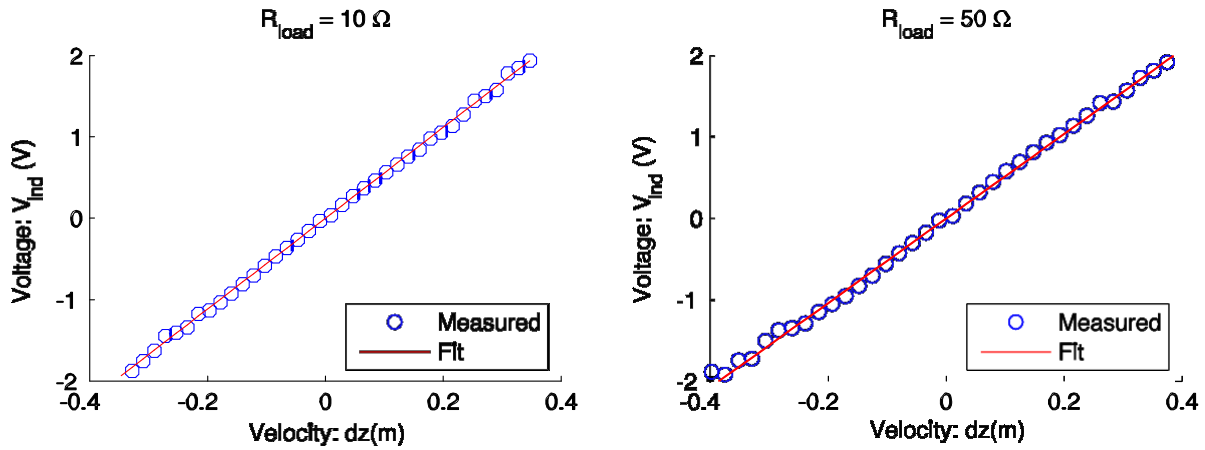

Figure 3.12: Approximate induced voltages

For a load resistance of $10\,(\Omega)$ the slope correspondes to a value of $k_t = 5.584\,(n \cdot \blacksquare\blacksquare)$, and for $50\,(\Omega)$ the slope corresponds to a value of

$k_t = 5.191\ (n \cdot ⬚)$. Again these values very close to the predicted maximum value of k_t.

3.4 Conclusion

From this chapter the major components of the system were identified using the various techniques. The transduction factor was found through the use of a semi-analytic method employing the finite element method. This electromechanical coupling was found to act in a linear way, despite the dependence on displacement. Using the resorting force surface method the stiffness of the NES was found to exhibit a cubic nonlinearity with a small linear component. The force contributed by the repelling magnets were found to be predominantly linear when place in close vicinity to the oscillating magnets. They will be used to balance the beam forces but will be kept at a maximum distance from the oscillating magnets. With this information the final equations of motion can be written for the system

$$m_p ⬚_p + ⬚_p(⬚_p - ⬚) + ⬚_p(⬚_p - ⬚) - ⬚_a(⬚_a - ⬚_p) - ⬚_m ⬚_a - \frac{k_t^2}{⬚_p ⬚} - ⬚_m(⬚_a - ⬚_p) - \frac{⬚_{⬚⬚⬚⬚}}{\frac{c⬚⬚⬚⬚}{2R}} + ⬚_{⬚⬚⬚⬚}(⬚_a - ⬚_p) = 0 \quad (3.23)$$

$$m_a ⬚_a + ⬚_a ⬚_a - ⬚_p ⬚ + ⬚_m ⬚_a - \frac{k_t^2}{⬚_p ⬚} + ⬚_a ⬚_a + \frac{⬚_{⬚⬚⬚⬚}}{2⬚_{⬚⬚⬚⬚} + ⬚_{⬚⬚⬚⬚}}(⬚_a - ⬚_p) = 0 \quad (3.24)$$

$$i = \frac{⬚_t ⬚}{2⬚_{⬚⬚⬚⬚} + ⬚_{⬚⬚⬚⬚}} \quad (3.25)$$

Chapter 4

System Analysis

4.1 Transient Response

Many previous works have found that the NES is an excellent transient vibration absorber [10, 19, 47-49], both theoretically and experimentally. The main phenomenon behind the effectiveness of the NES is attributed to energy pumping or targeted energy transfer (TET). During TET, vibrational energy is transferred to a passive sink (NES), where the energy is localized and diminished due to damping. An essential component of TET is 1:1 resonance capture between the NES and the primary system, where the NES passively tunes itself to oscillate close to or at the frequency of the primary system, resulting efficient energy transfer.

The NES is capable of 1:1 resonance capture due to the lack of linear stiffness or more importantly a lack of dominant natural frequency. This was briefly demonstrated in Fig. 2.6, where the oscillating NES exhibited a wide range of frequencies. In section 3.3.2, the stiffness of the experimental NES consisted of a nonlinear and an unwanted linear component. Many studies [20, 22] have found similar results when trying to generate a purely cubic stiffness, that a small linear component will exist. It is a common practice to dismiss this term during simulations; this work will retain this term to examine its effects.

4.1.1 Vibration Absorption

To analyze the system defined by Eqns.(3.23)-(3.25), it is useful to define some parameters that will make clear the performance of the NES and to illustrate the phenomenon of TET and 1:1 resonance capture. To be comparable to the physical apparatus, the system will be set into oscillation by displacing the primary mass and releasing it, giving the initial conditions of the system equal to $x_p(0) = x$, $x_a(0) = x$, $\dot{x}_p(0) = 0$, $\dot{x}_a(0) = 0$. The relative displacement in this case
will be zero, and all the initial energy is stored in the primary system. To that end it is useful to define system outputs and inputs in terms of energy. The total initial input energy to the system is equal to the potential energy stored in the primary system:

$$E_{input} = E_{input}(0) = \frac{k x^2}{2} \tag{4.1}$$

The total energy present at time t within the NES can be found as the sum of potential and kinetic energies:

$$E_{NES}(t) = \frac{m_a \dot{x}_a^2}{2} + \frac{k_a (x_a - x_p)^2}{2} + \frac{k_n (x_a - x_p)^4}{4} \tag{4.2}$$

Likewise, the total energy present within the primary system can be written as the sum of the potential and kinetic energies:

$$E_p(t) = \frac{m_p \dot{x}_p^2}{2} + \frac{k_p x_p^2}{2} \tag{4.3}$$

A very useful measure to evaluate the effectiveness of the NES and to determine if TET has been realized is the percentage of the instantaneous total energy stored within the NES, which can be written as the energy present within the NES over the total system energy at time t.

$$\eta(\omega) = \frac{P_{sig}(\omega)}{P_{sig}(\omega) + P_{sig-NR}(\omega)} \times 100 \quad (4.4)$$

To obtain a quantitative view of the vibration absorption, a series of simulations are presented at different initial energy levels. For each of the simulations the load resistance is $R_{load} = 50\,(\Omega)$, which corresponds to a maximum total damping of $B_{max} = 0.4249\,(N/V)$ when $H = 0$. The simulations will include the changing transduction factor from Eqn. (3.8).

The first simulation will represent a low level of initial energy, with the initial displacement being $X = 6 \times 10^{-4}\,(m)$ or an initial energy value of E_{cnt} $8.766 \times 10^{-4}\,(J)$, with results in Fig. 4.1. The response for the system is dominated by the primary system oscillating at its natural frequency. The NES contributes in a minimal way, with most of the energy being remaining in the primary system. The most important factor is that the system does not engage in 1:1 resonance, the primary system and NES being completely out of phase, which prevents the efficient transfer of energy to the NES. Although the vibration absorption is poor, there is still some voltage induced in the coil, due to the systems oscillating relative to one another.

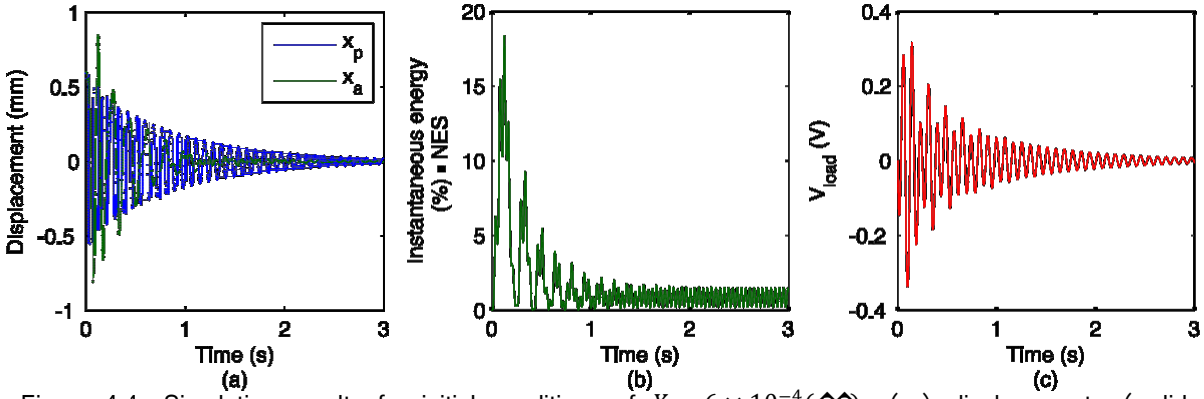

Figure 4.1: Simulation results for initial conditions of $X = 6 \times 10^{-4}(m)$: (a) displacements (solid line: primary system; dashed line: NES); (b) percentage of the instantaneous total energy in the NES and (c) voltage across load resistor.

In the second simulation the energy level is increased to a mid-level value. Here the initial displacement is $X = 1 \times 10^{-3}\,(m)$ or an initial energy value of $E_{cnt} = 2.4^{-3}\,(J)$, with the results shown in Fig. 4.2. It can be seen from the response that at this energy level the NES has been engaged, resulting in large

amplitudes, and better vibration absorption. The energy of the system becomes localized to the NES for a short period, but the energy flows between the primary system and NES in a reversible nature. This reversible energy transfer is a result of nonlinear beating phenomenon, where the system does not enter into 1:1 resonance, but is very close. As the energy is exchanged between the systems, it is subject to more damping, dissipating more energy and resulting in excellent vibration absorption. This is the phenomenon of TET working at its best. The energy becomes quickly localized in the NES or the target, and is then dissipated through damping. Repeated successions of this result in good vibration attenuation. The absorber also shows a wide range oscillating frequencies, a key characteristic of an essentially nonlinear device. With the increase in initial energy, there is an additional increase in voltage across the load.

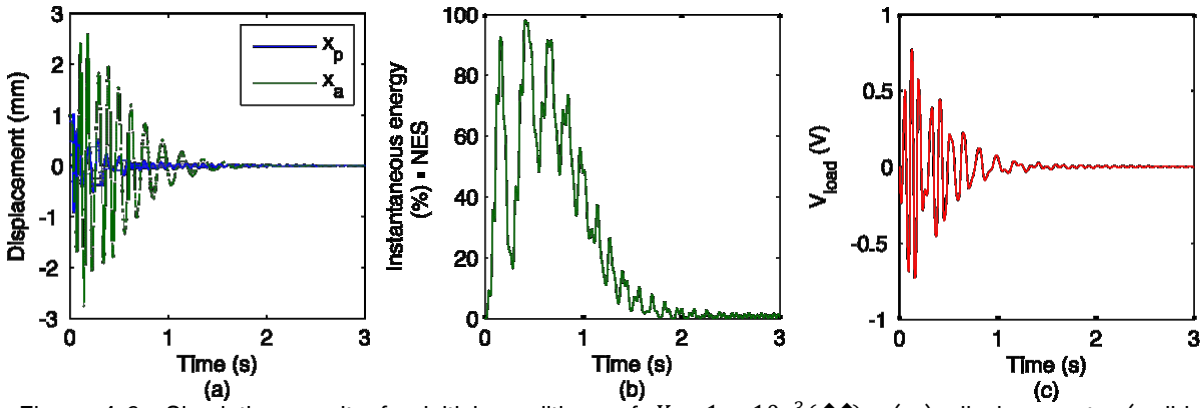

Figure 4.2: Simulation results for initial conditions of $X = 1 \times 10^{-3}$(□□): (a) displacements (solid line: primary system; dashed line: NES); (b) percentage of the instantaneous total energy in the NES and (c) voltage across load resistor.

Figure 4.3 shows the response for an increased initial displacement of $X = 2 \times 10^{-3}$ (□□), or an initial energy of □□$_{ent} = 9.7 \times 10^{-3}$ (□□) for a mid-high energy. The beginning of the response contains a nonlinear beating phenomenon, less dramatic than the previous case. Following this, the system enters into a 1:1 resonance capture resulting in an irreversible energy localization to the NES. Again this is the phenomenon of TET at work. The two systems are synchronized, vibrating with the same frequency. The energy then begins to be released back to the primary system at approximately $t = 1.80$ (□□), but the total energy is minimal at

this

point. The voltage across the resistor has also been greatly increased, with the additional initial energy. The nonlinear beating and 1:1 resonance regimes can be clearly seen in the voltage response being a function of the relative velocity.

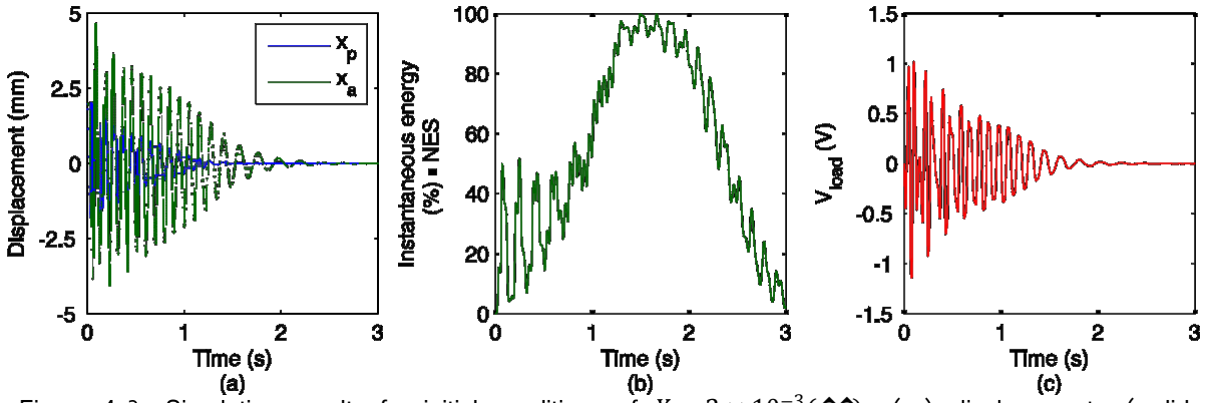

Figure 4.3: Simulation results for initial conditions of $X = 2 \times 10^{-3}$(**): (a) displacements (solid line: primary system; dashed line: NES); (b) percentage of the instantaneous total energy in the NES and (c) voltage across load resistor.

To further see TET in action, a final simulation with high initial energy, $X = 5 \times 10^{-3}$ (**) is conducted and shown in Fig. 4.4. Here the initial energy corresponds to $**_{cnt} = 60.7 \times 10^{-3}$ (**). One can see the dramatic effects of TET; the system having the same overall dynamics as the previous simulation, but with a clear indication of the irreversible energy transfer to the NES.

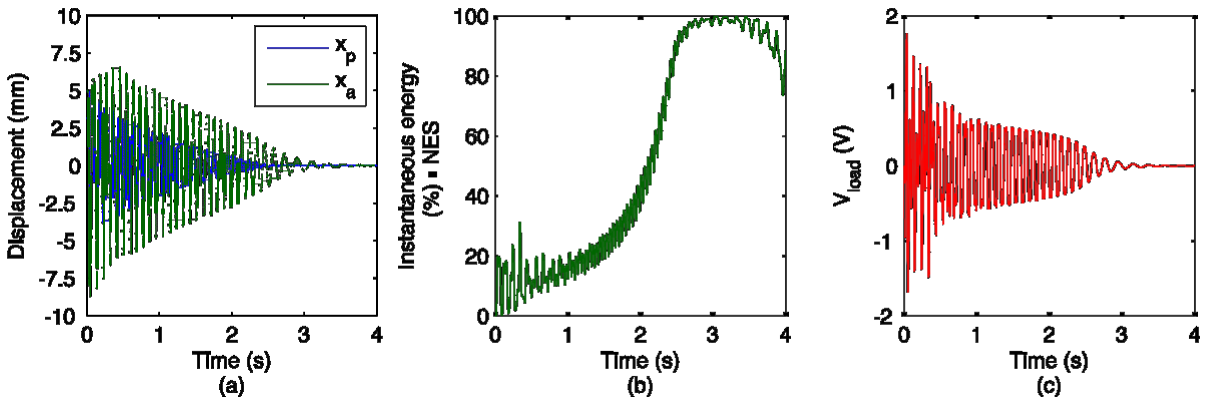

Figure 4.4: Simulation results for initial conditions of $X = 5 \times 10^{-3}$(□□): (a) displacements (solid line: primary system; dashed line: NES); (b) percentage of the instantaneous total energy in the NES and (c) voltage across load resistor.

Because of the increased amount of initial energy, the system takes a longer time to dissipate the energy. The response also contains little nonlinear beating, entering into 1:1 resonance very quickly.

To better understand the performance of these simulations, a good measure is to look at the total percentage of energy that is dissipated by the NES. This value is the percentage of the initial energy dissipated through the total NES damping for the duration of the response and provides a good reference for performance. The dissipated energy is defined as:

$$□□_{D\,□□□□N} = \frac{□□_a \int_0^t □□□_a(□□) - \quad ^2 □□t}{□□□□_p(□□)□} \times 100 \qquad (4.5)$$

$$□□_{D\,□□□□N} = \frac{(□□_{am} + □□_w)}{□□□_a} \frac{\int_0^t □□□_a(□□) - \quad ^2 □□t}{□□□□_p(□□)□} \times 100 \qquad (4.6)$$

The dissipated energy was calculated for all four simulations and shown in Table 4.1. An extensive series of simulations were conducted to show the dissipated energy as a function of initial displacement in Fig. 4.5, with four simulations shown as points.

Table 4.1: Calculated results of dissipated energy percentage for four simulations.

Level		X (□□)	□□$_{cnt}$ (□□)	□□$_{D}$ □□□□N
Low	(A)	6×10^{-4}	8.766×10^{-4}	42.9
Mid	(B)	1×10^{-3}	2.4×10^{-3}	80.8
Mid-High	(C)	2×10^{-3}	9.7×10^{-3}	61.2
High	(D)	5×10^{-3}	60.7×10^{-3}	29.2

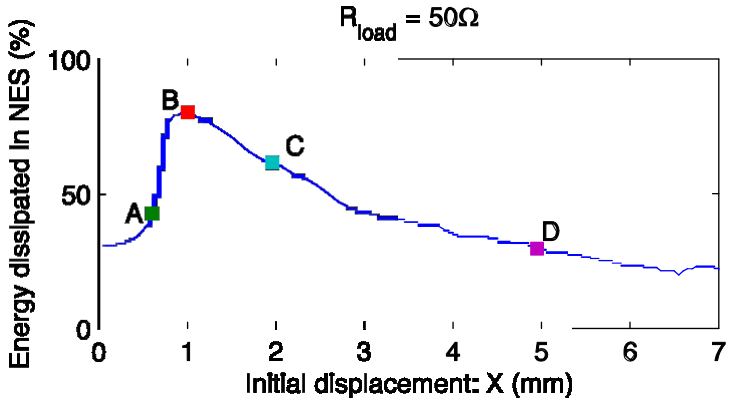

Figure 4.5: Percentage of the dissipated energy as a function of the initial displacement; points refer to four specific simulations.

The results from Fig. 4.5 illustrate that there is a region in the mid to mid-high initial energy range where the NES performs well as a passive vibration absorber. There is a well-defined critical threshold of initial energy before the NES will be engaged. Although high energy levels show a decrease in performance, the NES nonetheless is capable of targeted energy transfer localizing much of the energy. It is important to highlight here that this system required no a priori tuning. The essential nonlinearity is able to self-tune to the natural frequency of the primary system.

For comparison two simulations with varying primary system parameters are shown. The first one will have an increase of the primary mass, which will result in a lowering of the natural frequency. The second will have an increase of the primary stiffness giving a higher natural frequency. Both will be given an initial displacement of $X = 1 \times 10^{-3}\,(m)$. The parameters are given in Table 4.2.

Table 4.2: Parameters for comparison simulations: 1) change in primary mass, 2) changing in primary stiffness.

	m_p (k??)	k_p (??/??)	??$_p$ (H??)	??$_{cnt}$
1	2	4870	7.85	8.7660^{-4}
2	0.917	7000	13.9	3.5×10^{-3}

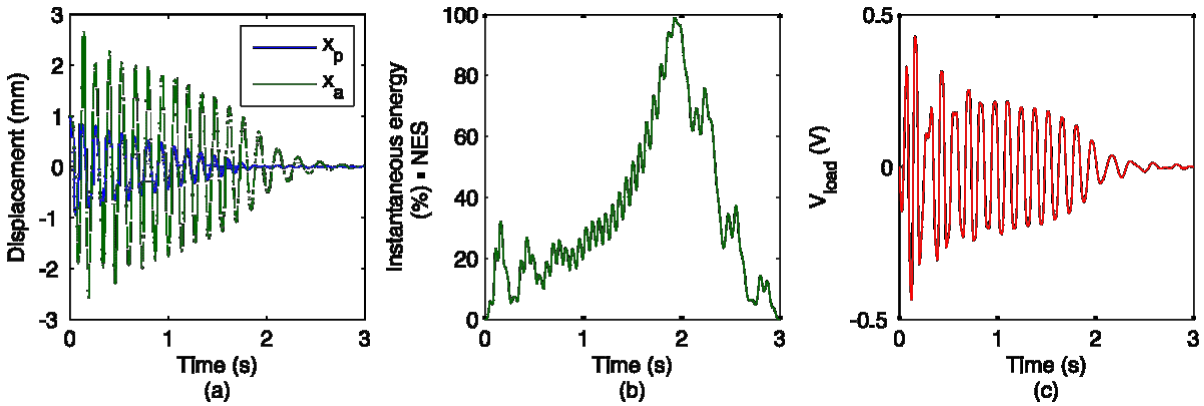

Figure 4.6: Simulation results for increase in ??$_p$ with initial conditions of $X = 1 \times 10^{-3}$(??): (a) displacements (solid line: primary system; dashed line: NES); (b) percentage of the instantaneous total energy in the NES and (c) voltage across load resistor.

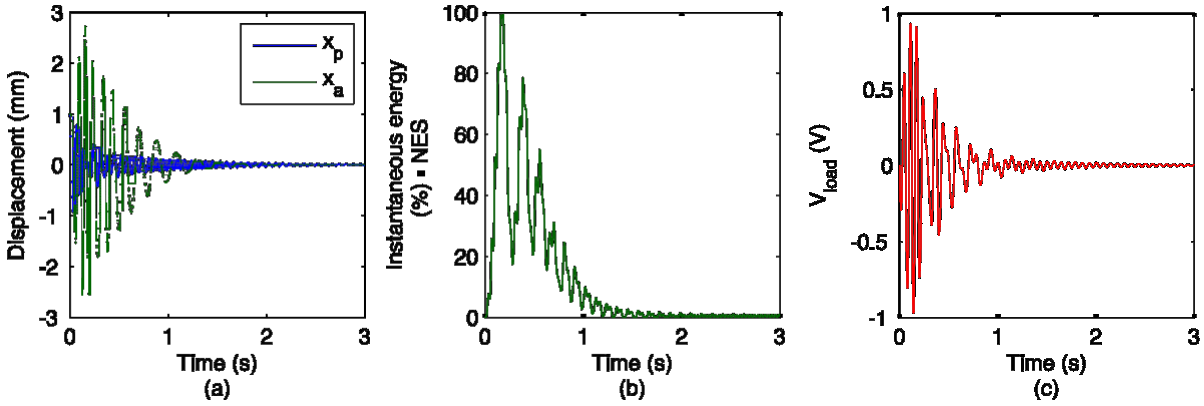

Figure 4.7: Simulation results for increase in ??$_p$ with initial conditions of $X = 1 \times 10^{-3}$(??): (a) displacements (solid line: primary system; dashed line: NES); (b) percentage of the instantaneous total energy in the NES and (c) voltage across load resistor.

From the results in Figs 4.6-4.7, the robustness as a vibration absorber can be seen. Although the system is completely passive, the essential nonlinearity performs actively, being able to oscillate at a wide range of frequencies. This ability to perform without tuning for a variety of primary system parameters makes it preferable over the traditional tuned mass damper with linear stiffness.

4.1.2 Frequency Energy Plots

It has been shown that the NES has a threshold of energy before the NES will be engaged. This threshold marks the beginning of 1:1 resonance and energy transfer. From this one can assume that there is a relationship between frequency and energy. To better understand this relationship a brief study in the nonlinear normal modes (NNM) and periodic orbits can be used to develop this coupling. It begins by look at the underlying Hamiltonian system of Eqns.(3.23)-(3.25):

$$m_p\ddot{x}_p + c_p\dot{x}_p - c_a(\dot{x}_a - \dot{x}_p) - k_n(x_a - x_p)^3 = 0 \quad (4.7)$$

$$m_a\ddot{x}_a + c_a(\dot{x}_a - \dot{x}_p) + k_n(x_a - x_p)^3 = 0 \quad (4.8)$$

The study is performed by applying the complexification technique [14], where the system is broken into fast-slow dynamics through the introduction of complex variables

$$\psi_1 = x_p + j\tilde{x}_p \quad \text{and} \quad \psi_2 = \frac{}{} \quad x_a + j\tilde{x}_a \quad (4.9)$$

where ω will be the dominant frequency and $j = \sqrt{-1}$. The displacements and accelerations can then be expressed in terms of the new complex variables:

$$x_p = \frac{\psi_1 - \bar{\psi}_1}{2j\omega}, \quad \dot{x}_p = \frac{1}{2}(\psi_1 + \bar{\psi}_1), \quad \ddot{x}_p = \dot{\psi}_1 \frac{j\omega}{2}(\psi_1 + \bar{\psi}_1) \quad (4.10)$$

$$x_a = \frac{\psi_2 - \bar{\psi}_2}{2j\omega}, \quad \dot{x}_a = \frac{1}{2}(\psi_2 + \bar{\psi}_2), \quad \ddot{x}_a = \dot{\psi}_2 \frac{j\omega}{2}(\psi_2 + \bar{\psi}_2)$$

$_2$ ($\blacklozenge\blacklozenge_2 + \psi\blacklozenge_2$) (4.11) —

where the bar denotes the complex conjugate. Since periodic orbits are sought, the assumption can be made that two oscillators will vibrate at the same dominant frequency, similar to the 1:1 resonance. The oscillation can be expressed in terms of [illegible] modulated by slowly varying amplitudes of $[illegible]_k$, $k =$

1,2:

$[illegible]_1 = [illegible]_1 [illegible]^{[illegible]}$ and $[illegible]_2 =$

$\phi_2 [illegible]^{[illegible]}$ (4.12)

Equations (4.10)-(4.12) can be inserted into Eqns.(4.7) and (4.8) giving the system described in complex (fast and slow) dynamics, yielding:

$m_p [illegible] \frac{d}{[illegible]} [illegible]_1 ([illegible]) [illegible]^{[illegible]} [illegible] - \frac{j\,\omega}{2} [illegible]_1 ([illegible]) [illegible]^{[illegible]} + \bar{\phi}_1 ([illegible]) e^{-[illegible]} [illegible]$

$[illegible] [illegible]_1 ([illegible]) [illegible]^{[illegible]} - \bar{\phi}_1 ([illegible]) e^{-[illegible]} [illegible]$

$- \frac{[illegible]_p}{2\omega} + \frac{j [illegible]_a}{2\omega} [illegible] [illegible]_1 ([illegible]) [illegible]^{[illegible]} - \bar{\phi}_1 ([illegible]) e^{-[illegible]} [illegible] + [illegible]\phi_2 ([illegible]) [illegible]^{[illegible]} - \bar{\phi}_2 ([illegible]) e^{-[illegible]} [illegible]^3$ (4.13)

$+ \frac{jk_n}{2\omega} [illegible] [illegible]_1 ([illegible]) [illegible]^{[illegible]} - \bar{\phi}_1 ([illegible]) e^{-[illegible]} [illegible] + [illegible]\phi_2 ([illegible]) [illegible]^{[illegible]} - \bar{\phi}_2 ([illegible]) e^{-[illegible]} [illegible]$

$= 0$

$m_a [illegible] \frac{d}{[illegible]} [illegible]\phi_2 ([illegible]) [illegible]^{[illegible]} [illegible] - \frac{j\,\omega}{2} [illegible]\phi_2 ([illegible]) [illegible]^{[illegible]} + \bar{\phi}_2 ([illegible]) e^{-[illegible]} [illegible]$

$+ \frac{j [illegible]_a}{2\omega} [illegible] [illegible]\phi_2 ([illegible]) [illegible]^{[illegible]} - \bar{\phi}_2 ([illegible]) e^{-[illegible]} [illegible] + [illegible]_1 ([illegible]) [illegible]^{[illegible]} - \bar{\phi}_1 ([illegible]) e^{-[illegible]} [illegible]^3$ (4.14)

$+ \frac{jk_n}{2\omega}$

$$\left(-\phi_2(\omega)e^{-j\omega t} - \phi_2^*(\omega)e^{-j\omega t}\right) + \left(\phi_1(\omega)e^{j\omega t} - \phi_1^*(\omega)e^{j\omega t}\right) = 0$$

The equations are then simplified, averaging them over the dominant frequency ω, ignoring the higher order frequency terms of $e^{\pm 3j\omega t}$ and $e^{\pm 5j\omega t}$ and collecting the coefficients only of $e^{\pm j\omega t}$, leads to a set of complex modulated equations:

$$m_p\dot{\phi}_1 + \frac{3}{8\omega_n^2}\left(k_1\phi_2^2 + \phi_2^2 k_2 - \phi_1^2 k_1 - \phi_1^2 k_2\right) + \frac{3\omega_n}{4\omega^3}\left(k_1\phi_1^2\phi_2 - k_1\phi_2\phi_2^2\right) + \frac{j}{2\omega}\left(-k_p k_1 - k_d k_1 + k_d k_2 + m_p k_1\omega\right) = 0 \quad (4.15)$$

$$m_a\ddot{\phi}_2 + \frac{3}{8}\frac{k_n}{\omega^3}(-\ddot{a}_1\phi_2 - \dot{\phi}_2\dot{a}_2 + \dot{\phi}_1\dot{a}_1 + \phi_1\phi_2) + \frac{3j}{4\omega^3}(-\dot{a}_1\dot{\phi}_1\dot{a}_2 + \dot{a}_1 \quad \frac{j}{2\omega}(\dot{a}_a\dot{a}_1 - \dot{a}_a\phi_2) \phi_2\dot{\phi}_2) + + \dot{a}m_a\phi_2\omega = 0 \tag{4.16}$$

where the dot indicates the derivative with respect to time. The polar form of the complex amplitudes are introduced as $\dot{a}_1 = \dot{a}(\dot{a})\dot{a}^{\dot{\phi}(\dot{a})}$ and $\dot{a}_2 = \dot{a}(\dot{a})\dot{a}^{j\dot{a}(\dot{a})}$, where a and b are the real amplitudes of the primary mass and NES mass, and α and β are the real phases. Substituting the polar forms in Eqns.(4.15) and (4.16), and separating into the real and imaginary parts, four equations expressing the real amplitudes and phases of the system are obtained:

$$\dot{a}=\frac{1}{8m_p\omega^3}(-3\dot{a}_n\omega^3 - 3\dot{a}_n\omega^2 b - 4\dot{a}_a\dot{\phi}^2)\sin(\alpha - \dot{a}) + \frac{3}{8m_p\omega^3}(\dot{a}_n\dot{\phi}^2)\sin(2\alpha - 2\dot{a}) \tag{4.17}$$

$$\dot{a}=\frac{1}{8\omega m_a}(-9\dot{a}_n\omega^2 b - 4\dot{a}_a\dot{\phi}^2 - 3\dot{a}_n\omega^3)\cos(\alpha - \dot{a}) + \frac{3}{8m_p\omega^3}(\dot{a}_n\omega^2)\cos(2\alpha - \quad \frac{1}{8\omega m_p}(6\dot{a}_n 2\dot{a}) + \omega^3 \dot{\phi}^2 + 4\dot{a}_p\dot{\phi}^2 + 4\dot{a}_a\dot{\phi}^2 - 4m_p\dot{\phi}^4 + 3\dot{a}_n\omega^3) \tag{4.18}$$

$$\dot{b} = \frac{1}{8m_a\omega^3}(3\dot{\omega}\dot{\omega}^2 + \omega^3 + \dot{\phi}^2)\sin(\alpha - {}_n \quad 3\dot{a}_n \quad 4\dot{a}_a \quad \dot{a}) - \frac{3}{8m_p\omega^3}(\dot{a}_n\omega^2\dot{a})\sin(2\alpha - 2\dot{a}) \tag{4.19}$$

$$\dot{\omega}_a = \frac{1}{8 m_a r_a^3}\left(-9 r_a^2 - r_a a - r_a^3\right)\cos(\alpha - \beta)$$

$$+ \frac{3}{8 m_p r_a^3}\left(4 r_a^2 - 8 m_p r_a^3 \cos(2\alpha - 2\beta) + r_a^3 r_a^2 - 4 m_a r_a^4 + 6 r_n r_a^2 b + 3 r_n r_a^3\right) \quad (4.20)$$

Since we are looking for the periodic solutions, the solutions to all the equations shall be steady state and the derivatives with respect to time are set

equal to zero. Equations (4.17) and (4.19) are trivially solved if we assume the system oscillates in phase by letting $\alpha = \beta$, resulting in two equations describing the amplitudes of the two systems.

$$0 = \frac{1}{8\,\square\square m_a\,\square\square^3}(-9\square\square_n\square\square^2 b - 4\square\square_a\square\square\square\square^2 - \frac{3}{8m_p\,\square\square^3}(\square\square_n \quad 3\square\square_n\square\square^3) + \square\square^2) + \frac{1}{8\square\square m_p\,\square\square^3}(6\square\square_n\square\square\square\square^2 + 4\square\square_p\square\square\square\square^2 + 4\square\square_a\square\square\square\square^2 - 4m_p\square\square\square\square^4 + 3\square\square_n\square\square^3) \tag{4.21}$$

$$0 = \frac{1}{8\,\square\square m_a\,\square\square^3}(-9\square\square_n\square\square\square\square^2 - 4\square\square_a\square\square a - \frac{3}{8m_p\,\square\square^3}\square\square_n \quad 3\square\square_n\square\square^3) + \square\square^2 + \frac{1}{8\square\square m_p\,\square\square^3}(4\square\square_a\square\square\square\square^2 - 4m_a\square\square\square\square^4 + 6\square\square_n\square\square^2 b + 3\square\square_n\square\square^3) \tag{4.22}$$

The two equations that describe the amplitudes of the primary and the NES at a given frequency, can be solved numerically for a range of frequencies. In general the periodic responses can be given by:

$$\square\square_p(\square\square) \approx \square\square_p \cos\frac{\square\square_1 - \psi\square_1}{2j\omega} \cong \frac{a}{\omega}\cos\omega\square\square \quad \omega t = \tag{4.23}$$

$$\square\square_a(\square\square) \approx \square\square_a \cos\frac{\square\square_2 - \psi\square_2}{2j\omega} \cong \frac{b}{\omega}\cos\omega\square\square \quad \omega t = \tag{4.24}$$

Recalling that the goal was to define the relationship between energy and frequency, the total energy of the system can be defined as the potential energy of the system (zero velocity):

$$E = \frac{1}{2}\square\square_{pp}\square\square^2 \frac{1}{2}\square\square_a\square\square\square_a - {}^2 + \frac{1}{4}\square\square_n\square\square\square_a - {}^4\square\square_p\square \tag{4.25}$$

Figure 4.8 shows the results of Eqns.(4.21)-(4.25), for a range of frequencies, and depict the energies and frequencies of periodic solutions. The two curves are the so-called symmetric backbone curves [14], where the '+' indicates the system in phase, and the '-' indicates out of phase. At the low energy levels

the two curves represent the natural frequencies of the two systems, S11- ending at the natural frequency of the primary at 11.6 Hz, and S11+ the linear natural frequency of the NES approximately 4.5 Hz.

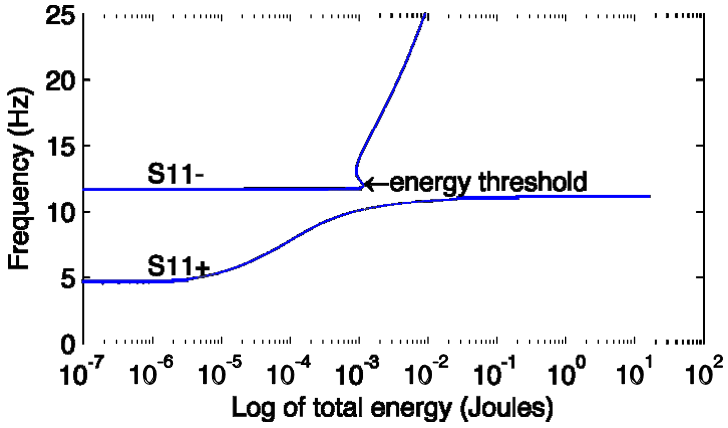

Figure 4.8: Analytic approximations of frequency energy plot: backbone curves S11±

The energy threshold of the system shown in Fig. 4.8, indicates the minimum energy required for the system to oscillate at the S11+ curve, if any lower than that the system will be attracted to the S11- curve. To illustrate this, a WT was applied to the relative response ($\diamond\diamond_a - \diamond\diamond_p$) of the four initial energy level
simulations. At each moment in time the total energy level was determined, and was matched to the corresponding frequencies at that moment in time determined from the WT. The results were combined into a frequency energy plot (FEP) with the S11± curves overlaid. For the low energy level in Fig. 4.9(a), it can be seen that energy has not passed the threshold, and the system tends to oscillate about the S11- curve. The dynamics show that the system is weakly nonlinear, being dominated by the linear primary system. Energy is still exchanged and damped through the NES, noting the existence of lower frequencies present from the NES.

Increasing the energy level in Fig. 4.9(b) for $X = 1 \times 10^{-3}$(◆◆), the energy has passed the critical threshold. In this case the vibration damping is high, as discussed earlier due to the nonlinear beating and high percentage of energy localization. The initial frequency is very close to the natural frequency of the primary system, which causes the strong beats. After most of the energy has been dissipated, the system is quickly attracted to the S11+curve, the frequency decreasing to the NES linear frequency.

The final two simulations in Fig. 4.9(c-d), where the energy levels are again increased, the presence of higher frequency components can be seen at the higher energy levels. Having a greater difference from the natural frequency of the primary system, there is less of the beating phenomenon, causing less damping. Both responses result in 1:1 resonance and are attracted to the S11+ backbone curve where energy is gradually localized to the NES.

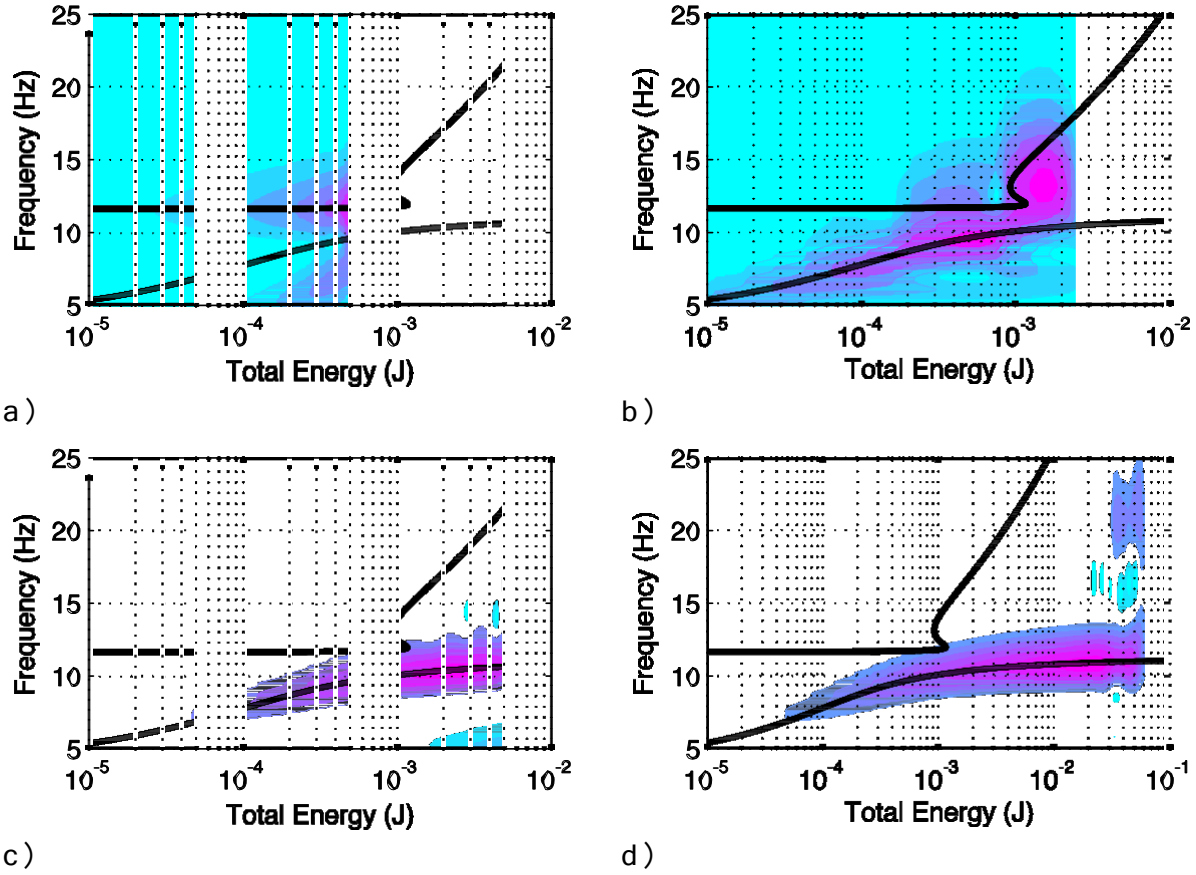

Figure 4.9: Frequency energy plots of wavelet transforms of the relative response $x_2 - x_1$ of the four simulations with superimposed backbone curves. S11+ a) low initial energy $X = 1 \times 10^{-4}$ (m), b) mid initial energy $X = 1 \times 10^{-3}$ (m), c) mid high energy level $X = 5 \times 10^{-3}$ (m) and d) high energy level $X = 2 \times 10^{-2}$ (m).

It has been found through simulations that the proposed NES is capable of vibration absorption. From the simulations and examining the frequency energy plots there exists an initial energy region where the NES has good performance, due to

strong nonlinear beating. Increasing the initial energy level will result in energy localization from 1:1 resonance but will take longer to dissipate energy.

4.1.3 Effects of Damping

The proposed NES in this work has a unique feature that can be changed very easily to change the overall performance; namely the damping. The load resistance can be changed which in turn changes the induced current in the electrical system which is directly related to the Lorentz force or damping. It stands to reason that with increasing of the damping the system can dissipate more energy.

To examine this effect, a series of simulations were conducted to determine the energy dissipated by the NES defined by Eqn.(4.6) for a range of load resistances and initial displacements. Figure 4.10 shows the results, demonstrating that an increase in damping does indeed improve absorption. The critical threshold still remains at approximately $X = 6 \times 10^{-4}$ (□□), being determined by the nonlinear beating dynamics, but for greater initial energies the increase in damping results in better performance.

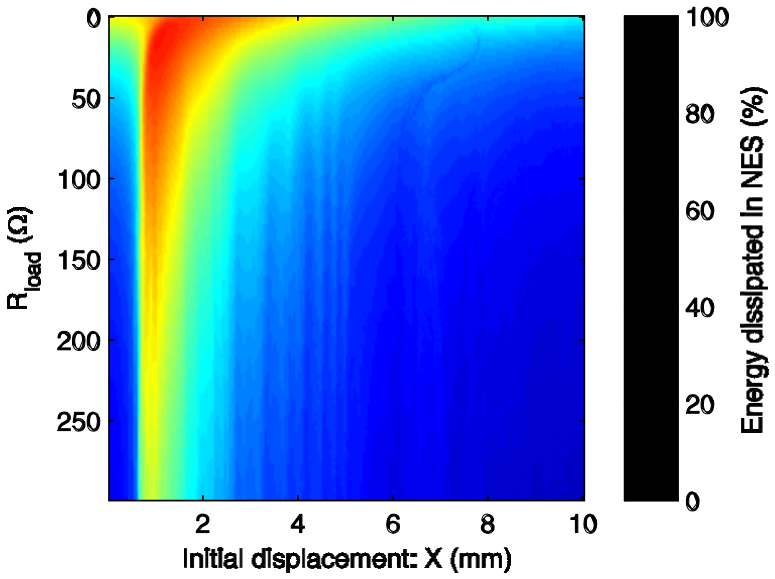

Figure 4.10: Energy dissipated by NES as a function of initial displacement and load resistance.

The simulation of the high initial energy level is repeated with a lower load resistance of $R_{load} = 10\ (\Omega)$. This corresponds to a maximum damping level of

$\lambda_{max} = 1.66\ (N s/m)$. For the same displacement of $X = 5 \times 10^{-3}$ (m), the oscillations are reduced to approximately $t = 1.8$ (s) in Fig. 4.11, as compared to approximately $t = 3$ (s) in Fig. 4.4. In addition to a reduction in oscillation time, there is a dramatic reduction in the voltage across the resistor. Clearly there is a relationship between the damping and the voltage.

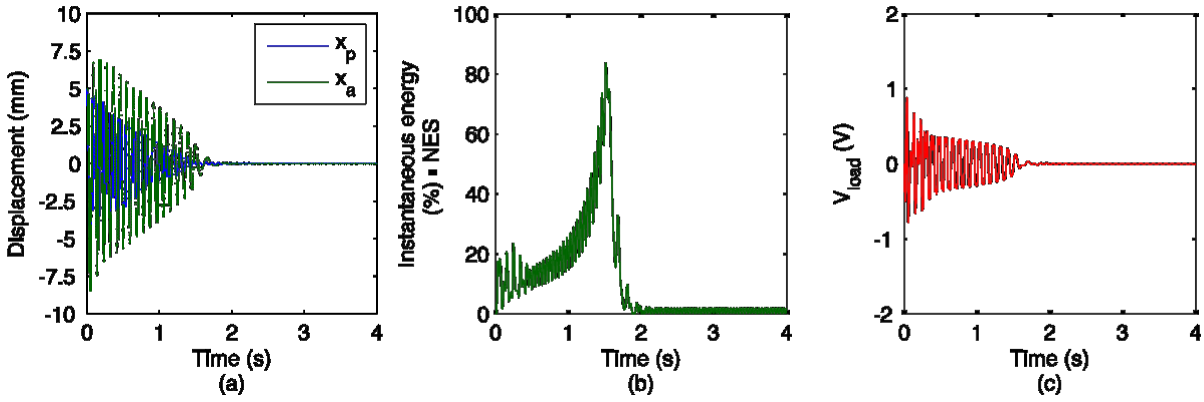

Figure 4.11: Simulation results for initial conditions of $X = 5 \times 10^{-3}$(m) and $R_{load} = 10(\Omega)$:

(a) displacements (solid line: primary system; dashed line: NES); (b) percentage of the instantaneous total energy in the NES and (c) voltage across load resistor.

4.1.4 Transient Energy Harvesting

As seen in the last simulation, increasing the damping by changing load resistance impacted the voltage across the load resistor. To investigate this, the amount of energy in Joules consumed by the resistor can be calculated. It can be defined as the summation of the power dissipated by the load resistor during time t.

$$E_{load} = \int_0^t P_{load}\, dt \qquad (4.26)$$

For comparison to the amount of energy dissipated by the NES, this energy can be expressed as a percentage of the total initial energy in the system as:

$$\eta_{load\%} = \frac{1}{E_0} \int_0^t P_{load}\, dt \times 100 \qquad (4.27)$$

where P_{load} is given by Eqn.(2.29), giving the total percentage of initial energy consumed by the load as:

$$\eta_{load\%} = \left(2\zeta_e + \frac{k^2 R_{load}}{\omega_n (R_{load} + R)^2}\right) \frac{\int_0^t x_a(\tau)^2 d\tau}{E_0} \times 100 \qquad (4.28)$$

Equation (4.28) bears a striking resemblance to Eqn.(4.6) being almost the same to the percentage of energy dissipated through the electrical damping η_{elec}.

Expressing Eqn.(4.6) in terms of only electrical damping and the transduction factor one gets:

$$\eta_{DNES} = \left(2\zeta_e + \frac{k^2 R_{load}}{\omega_n (R_{load} + R)^2}\right) \frac{\int_0^t x_a(\tau)^2 d\tau}{E_0} \times 100 \qquad (4.29)$$

which is almost identical to the $\eta_{load\%}$, the main difference being the terms:

$$\zeta(\zeta_{load}) = \frac{R_{load}}{2R\left(\frac{R_{load} + R}{R_{coil} + R_{load}}\right)} \qquad (4.30)$$

The term $\zeta(\zeta_{load})$ is a nondimensional factor that will express the amount of power available for harvesting from the amount of energy damped by the NES. Figure 4.12 shows how $\zeta(\zeta_{load})$ changes with the load resistance. A larger resistance indicates that more power could be extracted from the damping. Unfortunately this is contrary to Fig. 4.10, where the maximum damping occurs at lower load resistance.

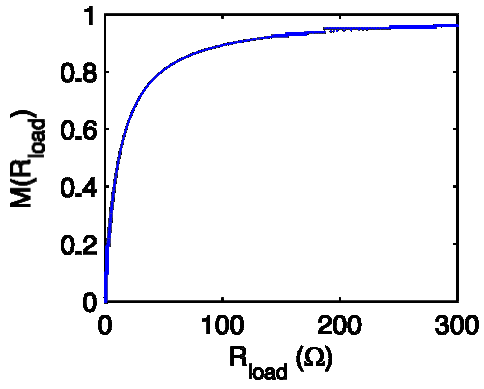

Figure 4.12: $M(R_{load})$ as a function of load resistance.

Evidently there is a tradeoff between the amount of damping and the extracted power in the transient regime. Applying Eqn.(4.28) for a series of simulation for varying load resistances and initial displacements, Fig. 4.13 shows the percentage of initial energy available for harvesting.

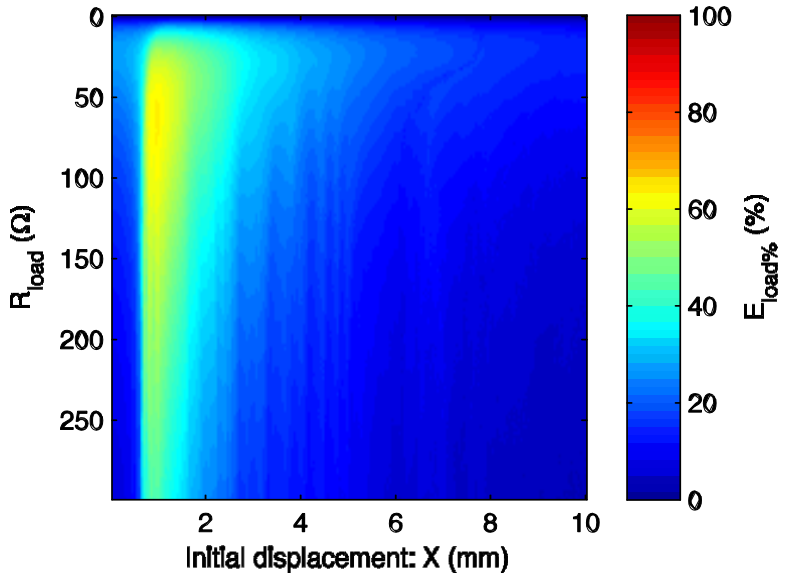

Figure 4.13: Energy across load resistor as a function of initial displacement and load resistance.

The effects of $M(R_{load})$ are visible and the shift between vibration performance and harvested energy exposed. Fortunately the tradeoff is not too large, especially for the large initial displacements.

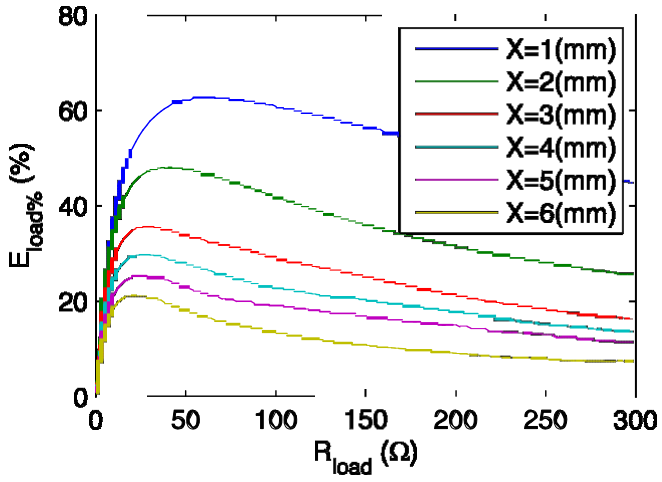

Figure 4.14: Energy across load resistor as a function and load resistance for different initial displacements.

Remarkably, for the ideal initial energy and with the proper selection of load resistance, the system is capable of harvesting approximately 62% of the initial energy. It is feasible then that if a designer knew the level of transient input energy to the system, an optimal energy harvesting device could be made to absorber and collect energy.

4.2 Harmonically Forced Responses

The study of the nonlinear dynamics of a harmonically forced NES poses some interesting problems due to the small (or non-existent) linear stiffness as well as the nonlinear stiffness and damping. As discussed in Section 1.2.3, the response of a NES may experience saddle node and hopf bifurcations, where saddle nodes mark the existence of multiple solutions while hopf bifurcations indicate strongly modulated responses.

The approach taken to analyze the harmonically forced system is to use the method of complexification [14, 50, 51]. In this method the dynamics are broken in the slow and fast parts similar to the steps taken in Section 4.1.2. Assuming a response of 1:1 frequency matching, a harmonic balance method is used to average

the response, and bifurcation analysis then performed. Although an accurate method to determine the response of the system, the method is tedious to implement and due to a few coordinate changes the response difficult to interpret.

A recent paper [52] applied a more traditional method of multiple scales coupled with a harmonic balance method (MSHBM). The elegance of this method is that the final equations are described in the real coordinate system, and variations to them are easily performed. The results also proved to be highly accurate for the purposes of describing saddle node and hopf bifurcations. The method below follows the proposed scheme.

The main equations of motion are defined as Eqns.(4.31)-(4.32). For the purposes of simplicity the damping of the NES will be considered linear, taking the maximum value of k_t corresponding to the maximum relative velocity.

$$m_p\ddot{x}_p + c_p\dot{x}_p + c_p\dot{x}_p - c_a\dot{x}_a - c_p\dot{x} - c_a\dot{x}_a - c_p\dot{x} - c_n(\dot{x}_a - \dot{x}_p)^3 = c_p\dot{y} + k_p y \tag{4.31}$$

$$m_a\ddot{x}_a + c_a\dot{x}_a - c_p\dot{x} + c_a\dot{x}_a - c_p\dot{x} + c_n\dot{x}_a - c_p\dot{x}^3 = 0 \tag{4.32}$$

where the forcing term can be expressed as $y = Y\sin(\Omega t)$, a harmonically moving base with Y as amplitude and Ω as frequency. Using trigonometric identities the forcing term on the right hand side of Eqn.(4.31) can be expressed in the simplified form:

$$c_p\dot{y} + k_p y = \sqrt{(\quad)^2 + (\quad)^2}\cos(\Omega t + \phi) = f\cos(\Omega t + \phi) \tag{4.33}$$

Combining equations (4.31)-(4.33) gives the main simplified equations of motion:

$$m_p\ddot{x}_p + c_p\dot{x}_p + c_p\dot{x}_p - c_a\dot{x}_a - c_p\dot{x} - c_a\dot{x}_a - c_p\dot{x} - c_n(\dot{x}_a - \dot{x}_p)^3 = f\cos(\Omega t + \phi) \tag{4.34}$$

$$m_a \ddot{x}_a + c_a \dot{x}_a - c_p \dot{x} + c_a \dot{x}_a - c_p \dot{x} + c_n \dot{x}_a - c_p \dot{x}^3 = 0 \qquad (4.35)$$

Equations (4.34) and (4.35) are then scaled by the mass of the primary. The equations are then converted into a simplified form, as well as changing the time scale. First the forcing frequency is made into a frequency ratio by setting:

$$\omega = \frac{\Omega}{\omega_p} \qquad (4.36)$$

where ω_p is the primary natural frequency. A new time scale is defined, such that:

$$\omega_p t = \tau \qquad (4.37)$$

Taking the derivative of Eqn. (4.37) with respect to time one can equate that:

$$\frac{d\tau}{dt} = \omega_p \qquad (4.38)$$

Introducing a general dummy coordinate $\alpha(\beta)$, the derivatives of $\alpha(\beta)$ with respect to time t may be expressed as:

$$x' = \frac{d}{dt}\alpha(\beta) = \frac{d\alpha(\beta)}{d\tau}\frac{d\tau}{dt} = \frac{d\alpha(\beta)}{d\tau}\omega_p \qquad (4.39)$$

$$x'' = \frac{d^2}{dt^2}\alpha(\beta) = \frac{d^2\alpha(\beta)}{d\tau^2}\left(\frac{d\tau}{dt}\right)^2 = \frac{d^2\alpha(\beta)}{d\tau^2}\omega_p^2 \qquad (4.40)$$

Noting that $(\cdot)'$ is the derivative with respect to time τ. The time scale transformation can be completed by using:

$$\dot{x} = x'\omega_p, \qquad \ddot{x} = x''\omega_p^2$$

$''\diamondsuit\diamondsuit^2$ (4.41)

Equations (4.34)–(4.41) can be combined to describe the system in a simplified form with respect to time ⬚:

$$\ddot{\square}_p + \Lambda\dot{\square}_p + \square_p - \dot{\square}\dot{\square}_a - \square_p - \square\square_a - \square_p - \mathrm{K}\square_a - \square_p = F\cos(\omega\tau + \square) \quad (4.42)$$

$$\rho\ddot{\square}_a + \dot{\square}\dot{\square}_a - \square_p + \square\square_a - \square_p + \mathrm{K}\square_a - \square_p = 0 \quad (4.43)$$

where:

$$\Lambda = \frac{\square_p}{m_p\square_p}, \quad \lambda = \frac{\square}{\square_a}, \quad \kappa = \frac{\square}{\square_a}, \quad \mathrm{K} = \frac{\square_n}{m_p\square_p^2}$$

$$\rho = \frac{m_a}{m_p}, \quad F = \frac{f}{m_p\omega_p^2}, \quad \omega = \frac{\Omega}{\square_p}, \quad \square_p = \sqrt{\frac{\square_p}{m_p}}$$

To ensure that the dynamics of both equations capture the whole system dynamics, it is convenient to introduce the relative displacement between the main structure and the NES, where $H = \square_a - \square_p$, so that Eqns.(4.42) and (4.43) be-
come:

$$\ddot{\square}_p + \square_p + \Lambda\dot{\square}_p - \square(H) - \square(\square) - \mathrm{K}(\square) = F\cos(\omega\tau + \square) \quad (4.44)$$

$$\square(\square'' + \square_p)\dot{} + \square(H) + \square(\square) + \mathrm{K}(\square) = 0 \quad (4.45)$$

In the new time scale the natural frequency of the primary system is equal to unity. A detuning parameter σ is introduced to relate the closeness of the excitation frequency to that of the natural frequency in the new time scale so that $\sigma = 1 - \square^2$:

$$\ddot{\square}_p + (\omega^2 + \square)\square_p + \Lambda\dot{\square}_p - \square(H) - \square(\square) - \mathrm{K}(\square) = F\cos(\omega\tau + \square) \quad (4.46)$$

$$\square(\square'' + \square_p)\dot{} + \square(H) + \square(\square$$

$$) + K(\blacksquare\blacksquare) \qquad = 0 \qquad (4.47)$$

Following the method of multiple scales [8], the equations are scaled with the small parameter $\varepsilon \ll 1$, according to the degree of cubic nonlinearity. Remaining

terms which are assumed small (all remaining have been divided by primary mass and natural frequency) are also scaled by ε, and results in:

$$\ddot{q}_p + \omega^2 + \varepsilon\hat{c}_{pp}\dot{q}_p + \varepsilon\Lambda_{pp} - \varepsilon\hat{c}_{pp}(H) - \varepsilon\hat{c}_{pp}(\dot{q}) - \varepsilon K(q)^3 = \varepsilon F\cos(\omega\tau + \phi) \quad (4.48)$$

$$\varepsilon\rho(\ddot{q} + \ddot{q}_p) + \varepsilon\hat{c}_{pp}(H) + \varepsilon\hat{c}_{pp}(\dot{q}) + \varepsilon K(q)^3 = 0 \quad (4.49)$$

According to the method of multiple scales, one begins by introducing a new set of time variables according to:

$$n_n = \varepsilon^n\tau \quad n = 0,1,2,\ldots \quad (4.50)$$

It follows then that the derivatives with respect to τ become an expansion of partial derivatives with respect to n_n:

$$\frac{d}{d\tau} = \frac{\partial n_0}{\partial\tau}\frac{\partial}{\partial n_0} + \frac{\partial n_1}{\partial\tau}\frac{\partial}{\partial n_1} + \frac{\partial n_2}{\partial\tau}\frac{\partial}{\partial n_2} + \cdots = D_0 + \varepsilon D_1 + \varepsilon^2 D_2 + \cdots \quad (4.51)$$

$$\frac{d^2}{d\tau^2} = D_0^2 + 2\varepsilon D_0 D_1 + \varepsilon^2(D_1^2 + 2D_0 D_2) + \cdots \quad (4.52)$$

A solution can then be assumed of Eqns.(4.48) and (4.49) by the expansion having the form of

$$q_p(\tau,\varepsilon) = q_{p0}(n_0,n_1,n_2,\ldots) + \varepsilon q_{p1}(n_0,n_1,n_2,\ldots) + \cdots \quad (4.53)$$

Substitution of Eqns. (4.51)-(4.53) into (4.48)(4.49), and collecting terms of the same order in ε, lead to the following perturbation equations:

Order ε^0:

$$D_0^2 q_{p0} + \omega_{p0}^2 q_{p0} = 0 \quad (4.54)$$

Order ε^1:

$$D_0^2 q_{p1} + \omega_{p0}^2 q_{p1} = -2D_0 D_1 q_{p0} - \hat{c}_{pp}(H)D_0 q_{p0} - \hat{c}_{pp}(\dot{q})D_0 q_{p0} - \Lambda_{pp} - K(q)^3$$

$$\omega_0 \omega_{p1} + \omega_{p1} \mp \omega_{p1} + 2\omega_0 \omega_1 \omega_{p0} + \Lambda\omega_0 \omega_{p0} - F\cos(\omega_0 n_0) \equiv 0 \quad (4.55)$$
$$\omega_0 \omega_0 - \omega_0 - K\omega_0$$

$$\varepsilon^2(\omega_0 x_{02}' + \omega_0 x_{02}) + \omega_0^2 x_{02} + \Lambda x_{01}^3 + \mathrm{K} x_{02} = 0 \quad (4.56)$$

Order ε^2:

$$\omega_0^2 x_{02}'' + \omega_1^2 x_{02} + \Lambda x_{01}^3 + \Lambda x_{01} x_{00}^2 + \omega_0^2 x_{02} + 2\omega_0 \omega_1 x_{01}' + \omega_1^2 x_{01} - \omega_1^2 x_{01} - 3\mathrm{K} x_{01}^2 x_{00} - \omega_1^2 x_{00} = 0 \quad (4.57)$$

$$\omega_0^2 x_{01}'' + \omega_0^2 x_{01} + 2\omega_1 \omega_0 x_{p0}' + 2\omega_1 \omega_0 x_{p0} + \omega_1^2 x_{00} - 3\mathrm{K} x_{00}^2 x_{01} - \omega_1^2 x_{01} = 0 \quad (4.58)$$

It is apparent that at the order of ε^0 there are no nonlinear terms or damping. Equation (4.54) describes the motion of an undamped primary system which has a solution of the form:

$$x_{p0}(n_0, n_1, \ldots) = A(n_1, n_2, \ldots) e^{i\omega n_0} + cc \quad (4.59)$$

where $A(n_1, n_2, \ldots)$ is an unknown complex function, i is the imaginary unit and cc stands for the complex conjugate. From this point an important assumption must be made concerning the dynamics of the NES. Similar to the transient response, one can expect that the NES will have a 1:1 internal resonance, and will oscillate with frequency ω. Applying this fact, an assumed solution for the first order relative motion is:

$$x_{01}(n_0, n_1, \ldots) = B_1(n_1, n_2, \ldots) e^{i\omega n_0} + cc \quad (4.60)$$

where $B_1(n_1, n_2, \ldots)$ is a first order unknown complex function. The ε^1 problems can

now be addressed. Equations (4.59)-(4.60) can be used in (4.56). The harmonic balance method is then used for frequency components of $e^{i\omega n_0}$. Higher order frequencies $(3\omega, 5\omega, \ldots)$ are not considered at this level of approximation, again being attributed to 1:1 internal resonance. This leads to:

$$i\omega B_1' - \rho\omega^2 B_1 + 3\mathrm{K} B_1^2 \bar{B}_1 + \omega_1^2 - \omega^2 = 0 \quad (4.61)$$

where the bar ($\bar{B}_1$) signifies the complex conjugate. Equation (4.61) describes the first order algebraic resonant amplitudes between the primary system and the NES. The equations can be further expressed in real form by substituting in (4.62) and (4.63):

$$\text{[illegible]}(n_1, n_2, \ldots) = \frac{1}{2}\text{[illegible]}(n_1, n_2, \ldots \text{[illegible]} \tau_0 \quad (4.62)$$

$$)e \quad \text{[illegible]}\tau_0 \quad (4.63)$$

$$\text{[illegible]}_1(n_1, n_2, \ldots) = \frac{1}{2}\text{[illegible]}(n_1, n_2, \ldots)e$$

which describe the real amplitudes of the primary system and the relative displacement ([illegible]), and the phase of the each ([illegible]) respectively. After substitution, the equation is then separated into real and imaginary parts giving:

$$\cos(\alpha - \text{[illegible]}) = \frac{1(-4\kappa b + 4\text{[illegible]}^2 b -}{3\text{[illegible]}^3 \mathrm{K})} \quad (4.64)$$

$$- \qquad 4 \qquad \rho\text{[illegible]}$$

$$\text{[illegible]}^2$$

$$\sin(\alpha - \text{[illegible]}) = \frac{\text{[illegible]}}{\frac{b}{\omega\rho a}} \quad (4.65)$$

Squaring both equations and summing them give:

$$\frac{(-4\kappa b + 4\rho\text{[illegible]}^2 b - 3\text{[illegible]}^3\mathrm{K})^2}{\text{[illegible]}^2\text{[illegible]}^2\text{[illegible]}^4} + \frac{\text{[illegible]}^2\text{[illegible]}^2}{\text{[illegible]}^2\text{[illegible]}^2\text{[illegible]}^2} - 1 = 0 \quad (4.66)$$

Equation (4.66) describes the constraints between the two amplitudes of the system, known as a nonlinear manifold. Equation (4.66) does not fully describe the dynamics of the system, but only the slow time scale motions. To capture the faster dynamics further perturbation is required. To do this the assumed solutions of (4.59) and (4.60) are inserted into (4.55):

$$\text{[illegible]}_{p1} + \text{[illegible]}^2\text{[illegible]}_{p11} - \text{[illegible]}$$

$$\mathrm{K}\text{[illegible]}^3 e \qquad \text{[illegible]}\tau_0 \qquad \frac{1}{\text{[illegible]}} \qquad 2$$

$$+ \text{[illegible]}A - i\text{[illegible]}_1\omega + i\Lambda\text{[illegible]}\omega + 2\text{[illegible]}_1 \quad - 3\text{K}\text{[illegible]}_1 \qquad (4.67)$$

$$\text{[illegible]}\omega - \frac{}{2}\text{[illegible]}e \qquad \text{[illegible]}_1$$

$$- \text{[illegible]}_1\text{[illegible]}e^{\text{[illegible]}T_0} + \text{[illegible]}\varepsilon = 0$$

Returning to the method of multiple scales, the objective is to obtain a solution to [illegible]_1, which is done by applying the solvability condition. The condition is

that any secular terms containing ⬚, should be caused to vanish by setting them to zero, resulting in:

$$\frac{1}{-i\omega e}\left(2i\sigma A + 2\Lambda A\,\omega - 6iK\,B^2 - 2i\,B\right) \qquad (4.68)$$

Equation (4.68) as well as its the complex conjugate of are inserted into (4.67) resulting in a solvable ordinary differentiable equation (4.69):

$$D_0 D_{p1} + D^2 D_{p11} - \frac{3}{K e} + c = 0 \qquad (4.69)$$

Solving the above equations results in 2 components, a homogenous and a particular solution based upon the principle of superposition. In the case of the multiple scales method the homogenous solution is not included as it is present at the order of D^0. Therefore the particular solution to (4.69) follows as:

$$D_{p1}(n_0, n_1, n_2, \ldots) = \frac{1}{8D^2}\,\frac{3}{K e} + c \qquad (4.70)$$

To proceed to the next order of perturbation D^2, it is necessary to again assume a solution for the response for the relative displacement. As before, it is assumed that there will be a 1:1 internal resonance:

$$D_1(n_0, n_1, \ldots) = D_2(n_1, n_2, \ldots)e^{\omega T_0} + c \qquad (4.71)$$

Substituting Eqns. (4.71),(4.70),(4.59) and (4.60) into (4.58) and applying the second harmonic balance for terms of ⬚ (neglecting the higher order terms) the following equation is achieved:

$$D_1 D_1 + D_2^2 + 3K D_1 B^2 + 6K D_1 B_1 D_2 + 2i D_1 D\omega + 2i D_1 D_1\omega - D_2 D^2$$

$$+ i\lambda \mathrm{B}_2 \omega = 0 \tag{4.72}$$

which describes the second order dynamics of the constrained system. In order to gain a full comprehensive description of the dynamics Eqns. (4.72) and (4.61) are summed:

$$(\lambda + 2i\rho\omega)\omega_1\omega_1 + 2i\omega\omega_1\omega\omega + 3\mathrm{K}(B_2 + B_1)\omega_1 + (\kappa - \omega^2 + 6\mathrm{K}B_1\omega_2 + i\omega\omega_1 + (-\rho\omega^2 + i\omega\omega + \omega)\omega_2 - \rho\omega^2 = 0 \quad (4.73)$$

Using the definition of the expansion of $B = \omega_1 + \omega\omega_2$, and noting that $\varepsilon \ll 1$, it can be concluded that the dominant part of $B = \omega_1$. Therefore Eqn. (4.73) can be simplified by setting $\omega_2 = 0$:

$$(\lambda + 2i\rho\omega)\omega_1 B + 2i\rho\omega_1\omega\omega + 3\mathrm{K}\omega^2 B + (-\rho\omega^2 + i\omega\omega + \omega)B - \rho\omega^2 = 0 \quad (4.74)$$

From the two harmonic balances at different orders of ε, Eqn.(4.74) describes the changing amplitude of B with respect to the n_1 time scale. Truncating the perturbation at order ω^1 for the primary system, Eqn.(4.68) also describes the changing amplitude of A with respect to the n_1 time scale. The presence of $\omega_1 A$ in (4.74) dictates that the response of the relative displacement is dependent on the response of the primary system. Substitution of the polar form of $\omega(n_1, \ldots) = \frac{1}{2}\omega(\omega)\omega^{\iota\alpha\omega}$ and $\omega(n_1, \ldots) = \frac{1}{2}\omega(\omega)\omega^{-\iota\alpha\omega}$ into these equations and noting that $(\dot{\circ}) = \omega_1(\circ)$, Eqns(4.68) and (4.74) can be written as

$$8(\omega + \iota\dot{a}\omega)\omega e^{\omega\alpha t} = \omega(-3i\mathrm{K}\omega^3 + (4\omega\omega - 4i\omega)\omega)e^{\omega\omega t} + 4(i\sigma - \Lambda\omega)e^{\omega\alpha t} - 4i\omega\omega e^{\omega\alpha t} \quad (4.75)$$

$$\frac{1}{4b}\omega 8\omega\omega - \frac{1}{2}\omega\omega + \omega\omega\omega - \omega\omega\omega\omega e^{-\omega(\omega - \omega)t} + 4(-2\rho\omega + i\omega\omega)\dot{\beta} + (4\lambda + 8i\rho\omega)\dot{b} + 4\omega\frac{3}{4}\omega^2\mathrm{K} - rho\,\omega^2 + \kappa + i\omega\omega\omega\omega\omega = 0 \quad (4.76)$$

From the above equations it can be seen that they describe the amplitude

( ) as well as the phase ( ) of the primary system and the relative dis-
placement as they change over time. Separating the equations into the real and imaginary parts and solving for the derivatives of each term, four first-order coupled nonlinear equations describing the amplitudes and phase of the system can be obtained:

$$\dot{\theta} = \frac{1}{8}(-3\,\theta^3 \mathrm{K} - 4\,\kappa) + \frac{1}{8}\lambda\, b\, \theta\, \theta \cos(-\beta + \theta) + \frac{1}{8}(4\,F\,\theta \sin(-\alpha + \theta) - 4\,\Lambda \tag{4.77}$$

$$\dot{\theta} = -\frac{1}{2}\lambda\, b\, \theta \sin(-\beta + \theta) + \frac{1}{8}(-3\,\theta^3 \mathrm{K} - 4\,\kappa\,\theta)\,\theta \cos(-\beta + \theta) + \frac{1}{8}(4\,\sigma\,a - 4\,F\cos(-\alpha + \theta)) \tag{4.78}$$

$$\dot{b} = -\frac{1}{4\,\theta^2 + 4\,\theta^2\theta^2}\Big(-8\,\rho\,\theta^2\Lambda + \frac{1}{2}\,\theta\,\theta(\theta^2 + \theta)\,\theta a\cos(-\beta + \theta) - 8\,\rho\omega a\,\theta(\theta^2 + \theta)\rho - \frac{1}{2}\theta\Lambda\theta\theta\sin(-\beta + \theta) + 4\,\theta\rho\,F\cos(-\beta - \theta + 2 + \theta) + 8\,\theta^2\omega F\sin(-\beta + \theta) + 3\,b\,\theta\frac{8}{3}\theta^2\theta^2 + \frac{4}{3}\theta^2 - \theta\theta\rho + \frac{4}{3}\theta\theta\theta\theta\theta\theta + \theta\mathrm{K}\theta^2 + \frac{4}{3} + \frac{4}{3}\mathrm{K}\theta^2 + \Big) \tag{4.79}$$

$$\dot{\theta} = \frac{1}{2\,\theta^2 + 4\,\theta^2\theta^2}\Big(-4\,\rho a^2 + \theta)\rho - \frac{1}{2}\theta\,\theta\Lambda\theta\theta\omega\cos(-\beta + \theta) + \theta(\omega + 4\,\rho a\,\theta\rho\theta^2\Lambda + \frac{1}{2}\,\theta\theta(\theta^2 + \theta)\theta\sin(-\beta + \theta) + 4\,\theta^2\theta F\cos(-\beta + \theta) - 2\,\theta\rho\,F\sin(-\beta + \theta) + 3\,\omega b\,\theta\frac{4}{3}\kappa + \mathrm{K}\theta^2\frac{4}{3}\theta^2\theta\theta^2 + \frac{4}{3}\kappa - \frac{2}{3}\theta^2\theta\rho\frac{2}{3}\theta^2\theta - \frac{2}{3}\mathrm{K}\theta^2 + \frac{2}{3}\Big) \tag{4.80}$$

Equations (4.77)–(4.80) describe the amplitude and phase of the system

in terms of periodic motions. Thus the equations need to be solved such that the derivatives of the four equations are equal to zero. The choice of using this modified multiple scale method was to retain the physical coordinates, making it easy to compare directly with numerical and experimental results. The equations can then be returned to main system parameters, shown in Appendix A due to the length.

Once solutions for Eqns.(4.77)-(4.80) are determined, the steady state response can be reconstituted from the solutions by means of:

$$\text{[illegible]}(\text{[illegible]}) = a\cos(\Omega t + \text{[illegible]}), \qquad \text{[illegible]}(\text{[illegible]})$$

$$= b\cos(\Omega t + \text{[illegible]}) \qquad (4.81)$$

In addition to describing the coupled system, the equations can also describe the uncoupled primary system. Setting $b = 0$, and $\beta = 0$, a Eqns.(4.82) and (4.83) express the motion of a harmonically forced single degree of freedom system.

$$\text{[illegible]} = \frac{1}{\text{[illegible]}}\frac{(4F\sin(-\alpha + \text{[illegible]}) - 4\Lambda a}{8 \qquad \omega} \qquad (4.82)$$

$$\text{[illegible]} = \frac{1}{\text{[illegible]}}\frac{\text{[illegible]}4(1 - \text{[illegible]}^2)\text{[illegible]}a - 4F\cos(-\alpha +}{8 \qquad a\,\omega} \qquad (4.83)$$

which can be reduced to:

$$\Lambda^2\frac{\text{[illegible]}^2\text{[illegible]}^2}{\text{[illegible]}^2} + \frac{(1 - \text{[illegible]}^2)^2\text{[illegible]}^2}{\text{[illegible]}^2} = 1 \qquad (4.84)$$

Returning to the main system parameters, Eqn. (4.84) can be arranged to describe the so called displacement ratio:

$$\frac{a}{Y} = \frac{\sqrt{\text{[illegible]}_p^2 + \text{[illegible]}^2}}{\sqrt{\left(\text{[illegible]}_p - m_p\Omega^2\right)^2 + \left(\text{[illegible]}_p\Omega\right)^2}} \qquad (4.85)$$

which is an identical representation of the displacement transmissibility ratio of the standard base excited single degree of freedom system [6]. It is important to note that the displacement transmissibility ratio remains constant despite any change in excitation amplitude.

4.2.1 Validation of the Solutions

Equations (4.77)-(4.80) are four coupled highly nonlinear equations with multiple solutions at various points, to efficiently solve these equations it necessary to use numerical methods. For this work the continuation software Matcont [53] will be used. The use of the software involves finding steady state solutions to the

system equations, and then finding neighboring equilibrium points by continuing with a single parameter, in this case the forcing frequency. In this way one can construct the so called frequency response plots (FRP). The advantage of such a software lies in the fact that during continuation, stability can be determined from the eigenvalues of the system equations, as well as determining the type of bifurcation at points of lost stability.

Figure 4.15 shows the FRP for the values of $Y = 0.005$ (��) and ��$_{����}$ $= 50$ (Ω). The blue lines indicate stable solutions with respect to periodic solutions, while red lines indicate unstable solutions with respect to periodic solutions. The green triangles represent limit points in the response, marking the existence of multiple solutions. The unstable region that lies between the limit points is achievable only through numerical integration, being an unstable saddle region. In real world applications, system responses will be attracted to one of the other two points at the same frequency. The black squares denote Hopf bifurcation points. The response of the system within this unstable region is a modulated periodic orbit.

To verify the outcomes of the FRP from Eqns.(4.77)-(4.80), and to determine if the effect of assuming k_t to be constant, an assumption made at the beginning of the MSHBM method, Eqns.(3.23)-(3.24) were numerically integrated at points of stability where the transduction factor changes with ��. The steady state response was recorded and the maximum amplitude of primary and relative displacement plotted on the FRP. Figure 4.15 shows that Eqns.(4.77)-(4.80) are in good agreement with numerical results, indicating that the MSHBM method works correctly, and that keeping k_t constant has no significant effects.

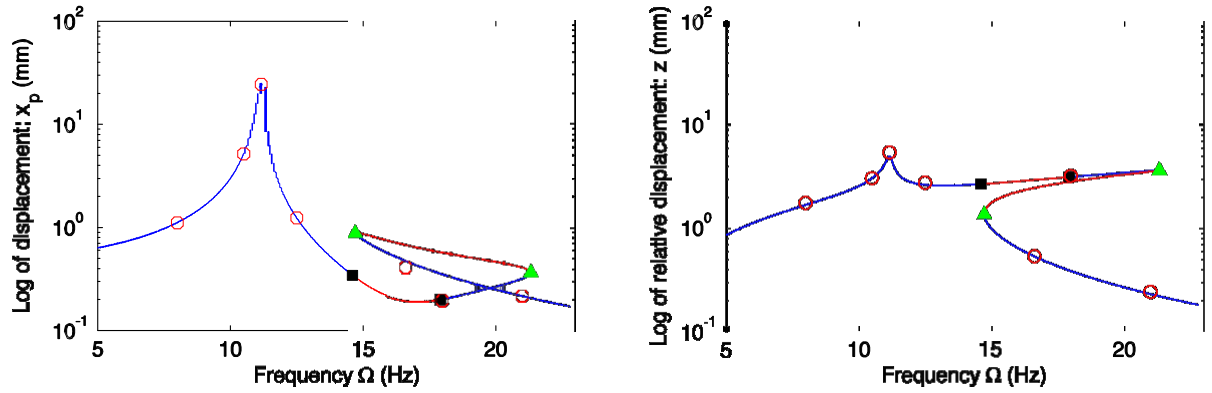

Figure 4.15: FEP for $Y = 0.005$ (m) and $\omega_n = 50(\Omega)$: a) primary displacement x_p, b) relative displacement z. Blue lines indicate stable periodic orbits. Red lines are unstable indicating non peri-odic orbits. Black squares indicate Hopf bifurcation points and green triangles limit points. Red circles are responses from numerical integration of equations (3.23),(3.24).

The dynamics within the unstable region of Hopf bifurcation represent a far departure from periodic solutions. As noted by many works [14, 16, 54, 55], a harmonically excited NES and linear oscillator may experience weakly modulated responses or the more interesting strongly modulated response (SMR). SMRs can be considered as a repeated form of TET. It was seen during the transient analysis that the most efficient vibration absorption occurred when the energy level induced a frequency close to the primary frequency causing a nonlinear beating. SMRs are in effect an extension of that principle. The beating phenomenon causes rapid exchanged of vibrational energy between the systems, which must be passed in part through damping.

Two frequencies are considered within the region of Hopf bifurcation with the aim to explore the response and to further validate the used method. Figures 4.16 and 4.17 show the response of the system excited at $\Omega = 14.4$ (H) and $\Omega = 16.5$ (H). The first row are the amplitudes computed from equations (4.76)-(4.79), the second row the reconstituted responses from equation (4.80) and the final the numerically integrated responses from the original equations (3.23) and (3.24). The responses are both clearly modulated, which can be seen from the predicted amplitudes b. The reconstituted responses show good agreement with the numerically integrated response.

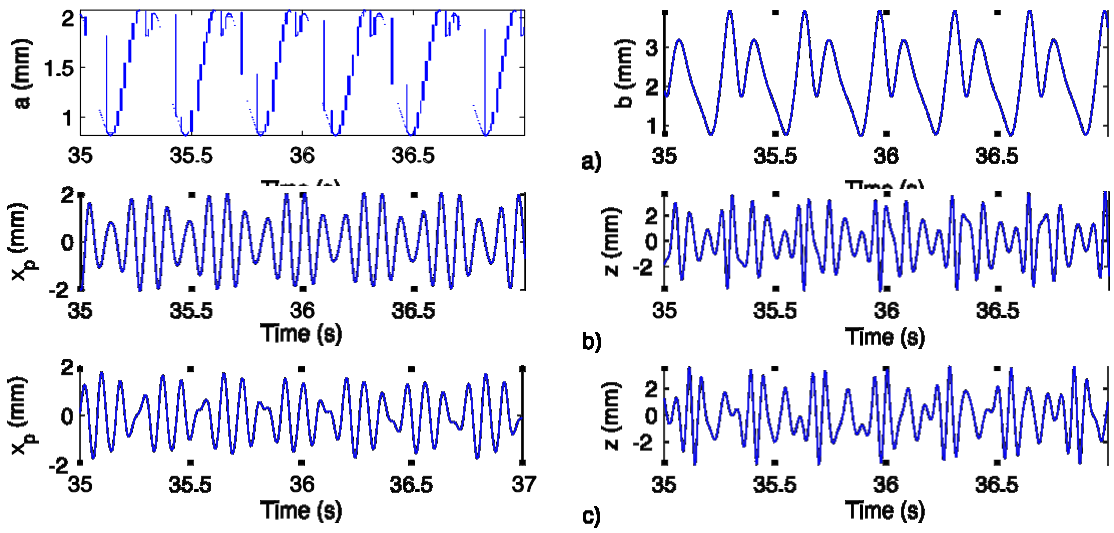

Figure 4.16: SMR when $Y = 0.005$ (��), ��$_{n}$ = 50(Ω) and Ω = 14.4 H(��) a) amplitudes computed from equations (4.77)-(4.80); b) reconstituted responses from equation (4.81); c) numerically integrated responses from original equations (3.23),(3.24).

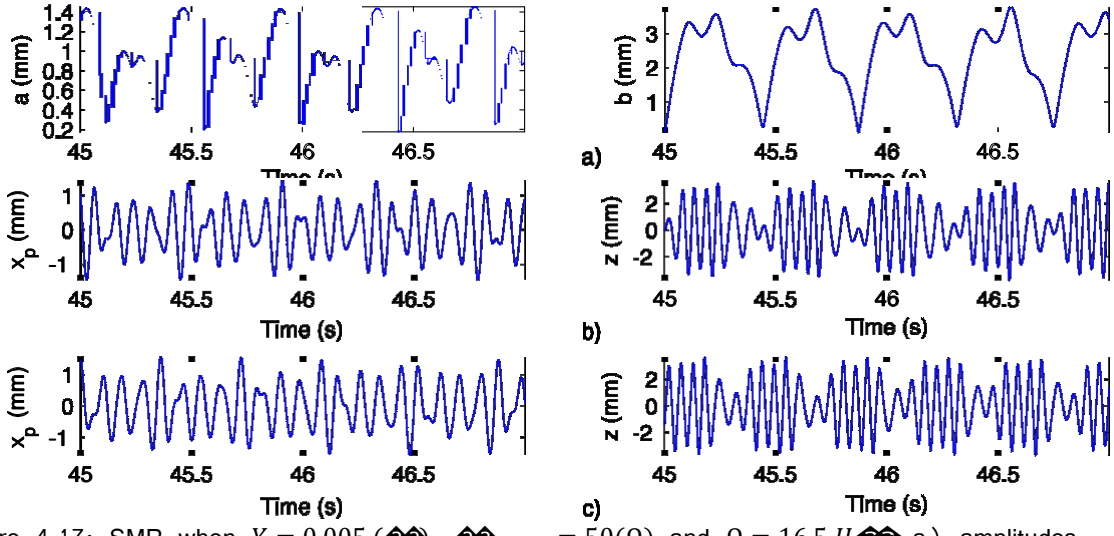

Figure 4.17: SMR when $Y = 0.005$ (��), ��$_{n}$ = 50(Ω) and Ω = 16.5 H(��) a) amplitudes computed from equations (4.77)-(4.80); b) reconstituted responses from equation (4.81); c) numerically integrated responses from original equations (3.23),(3.24).

4.2.2 Interpretation of FRPs

Having verified the solutions of Eqns. (4.77)-(4.80), it is important to understand the significance of the generated responses. The unstable area lying between the limit points indicated by green triangles is a physically unachievable response. Therefore at the frequencies lying within this region there are two solutions that can be realized, one being more attractive than the other depending on system conditions.

The spontaneous switching from one realizable solution to another is known as the so called jump phenomenon [8], and can be visualized through monotonically increasing or decreasing frequency sweeps, during which the forcing amplitude remains constant. Figure 4.18 shows the increasing sweep, the response path indicated by arrows. Best seen in the relative displacement plot the response will follow along the upper branch until the rightmost limit point is reached, where an increase in frequency will cause a jump to the lower branch. The primary system experiences the same jump in response at the rightmost limit point. Reversing the process in Fig. 4.19, the decreasing sweep shows the same jump occurring at the other limit point. In the case of the relative displacement the jump is from the lower branch to the upper, while the primary again jumps from a higher to a lower.

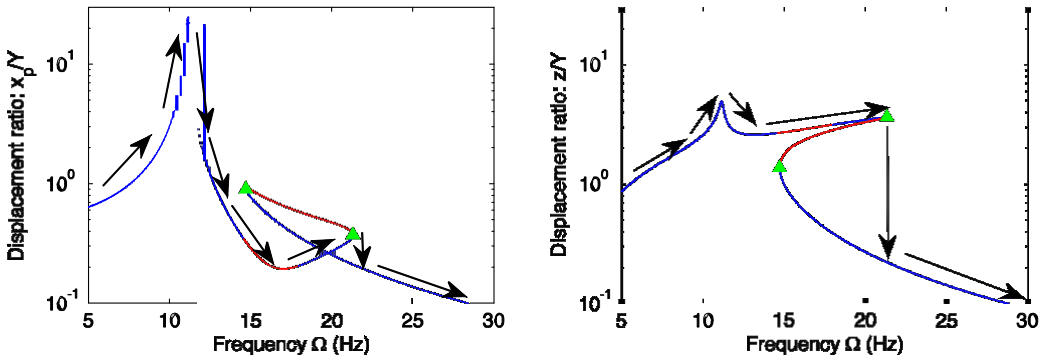

Figure 4.18: Increasing frequency sweep. Arrows indicate response path as frequency is increased.

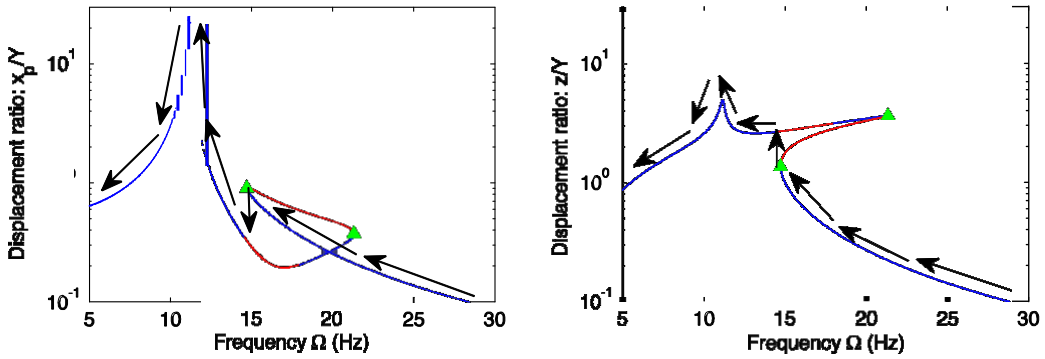

Figure 4.19: Decreasing frequency sweep. Arrows indicate response path as frequency is decreased.

The jump phenomenon is not determined solely by limit point bifurcations. Numerically, the attraction to one response over another is dictated by the initial conditions of the equations. Physically, the jump can occur at any frequency within the range between limit points. The likelihood of a jump occurring increases as the response approaches the nearest limit point. Within this region the system becomes sensitive to external disturbances; an applied force can cause a spontaneous jump, or a moment of increased damping can also cause a jump.

4.2.3 Response Analysis

The study of the performance of a NES is very involved, due to the highly nonlinear nature. In the transient analysis it was found that the NES performance is dependent on initial energy, introduced through initial conditions. It is reasonable then to expect a similar relationship for the harmonic regime. Figure 4.20 depicts the two extremes of the response that can be achieved. Line (A) corresponds to a large amplitude excitation of $Y = 1.5 \times 10^{-4}$ (m), while line (B) shows a low amplitude excitation of $Y = 9 \times 10^{-5}$ (m).

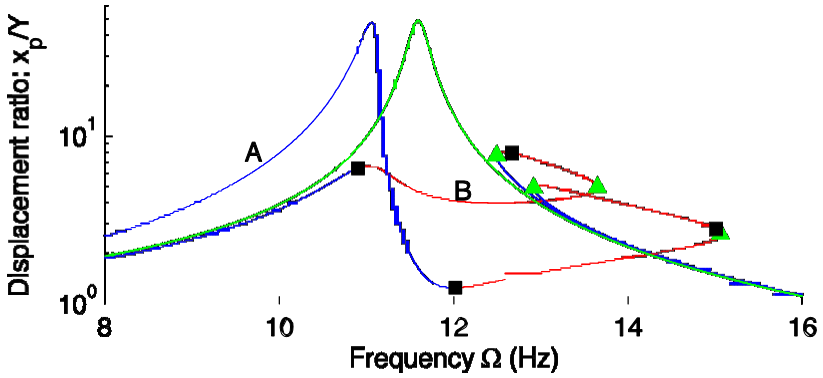

Figure 4.20: Comparison of two types of response regimes. A) high amplitude excitation, B) low amplitude excitation. Green line represents primary system with NES disengaged.

The analysis will examine the system in two general categories: 1) low amplitude excitation and 2) high amplitude excitation.

4.2.3.1 Low Amplitude Excitation

Figure 4.21 shows the FRP for $Y = 8 \times 10^{-5}$ (m) and $\Omega_{nonlinear} = 50$ (Ω). The green line represents the displacement transmissibility ratio of the primary system if the NES were detached. For the region between approximately 9-12.5 (Hz), the NES absorbs a large portion of the vibration. The region of highest vibration attenuation corresponds to the region of SMRs, a desirable trait for good vibration reduction. There exists a small region where multiple solutions may exist, indicated by the limit points. Although at this level of base amplitude the response is quite good, it does not show the full dynamics of the system.

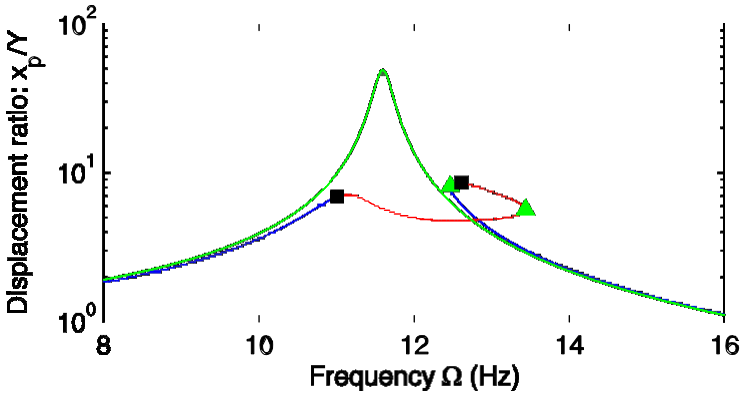

Figure 4.21: FRP for $Y = 8 \times 10^{-5}$(□□) and □□$_{□□□□} = 50(\Omega)$: Blue lines indicate stable periodic response and red lines unstable response. Black squares indicate Hopf bifurcation points and green triangles limit points. Green line represents primary system with NES disengaged.

Figure 4.22 shows the full dynamics of the system. In addition to the previous response, there exists a closed island of extremely high amplitude, comparable to that when the NES is not attached. The island consists of a single stable solution for the region 8.1-11 (Hz), and poses a significant problem in terms of vibration suppression performance.

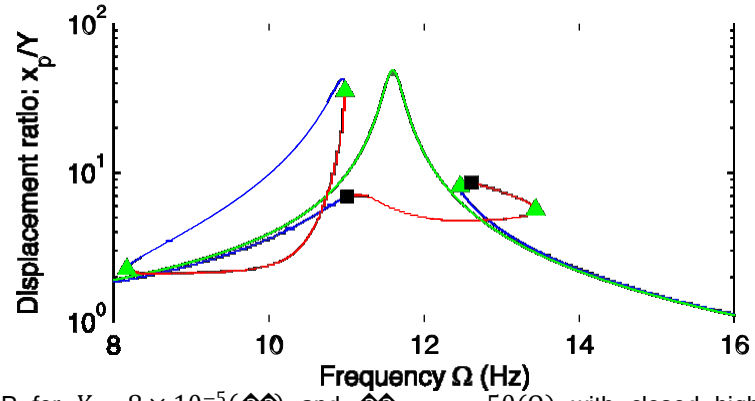

Figure 4.22: FRP for $Y = 8 \times 10^{-5}$(□□) and □□$_{□□□□} = 50(\Omega)$ with closed high amplitude island: Blue lines indicate stable periodic response and red lines unstable response. Black squares indicate Hopf bifurcation points and green triangles limit points. Green line represents primary system with NES disengaged.

Fortunately at this level of excitation amplitude this island is unrealizable. Numerical integration of the main system equations were conducted using a wide

variety of initial conditions, and the system was never induced to have islands amplitude. This conclusion is supported by [14], where Monte Carlo simulations were conducted for numerous frequencies and initial conditions; concluding that the steady state amplitude solutions were always attracted to lower amplitude values. In addition the high amplitude response has no full connection to the entire system over all frequencies making it completely disconnected to a full range of frequencies.

Assuming that the higher amplitude branches play no significant role, the load resistance can be varied to determine its contribution. Figure 4.23 shows the response for resistance values of 12, 25, 50 and 100 (Ω), corresponding to damping from high to low values respectively. At the first peak, the increase in damping yields no significant increase in amplitude for the primary system, and absorption isolation remains good. Beyond the first peak higher damping results in an increase in amplitude. It also has the result of minimizing the region of multiple responses due to limit point bifurcations. For $R_{load} = 100\Omega$, the response can be
significantly reduced but may still result in high amplitudes in locations of multiple responses.

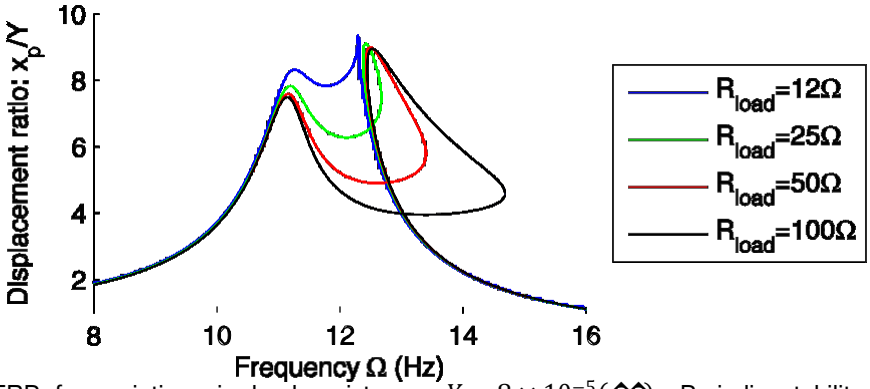

Figure 4.23: FRP for variations in load resistance. $Y = 8 \times 10^{-5}$(). Periodic stability and bifurcation points not shown for clarity.

Overall the vibration absorption is excellent at this level of excitation amplitude. At all damping levels, the overall response shape remains the same, the main difference being the extension of the region of multiple solutions. This does not affect the overall performance, but may have implication for the energy harvesting.

The main problem for this system is to determine the point at which the upper amplitude levels will become main attractors for the response. This work proposes a simple method to determine a maximum excitation amplitude that will induce the higher branch response. First a frequency must be selected corresponding to the peak amplitude ratio for the lower branch, in this case 11.02 (Hz). Equations (4.77)-(4.80) are then evaluated in terms of primary displacement ratio to force amplitude at the chosen frequency.

Figure 4.24 shows the results for the continuation with respect to excitation amplitude at $\Omega = 50\ (\Omega)$. Two limit points are encountered, marking a region that
is physically unattainable. These points are significant as they relate directly to the joining of the upper and lower branches. Any excitation amplitude to the left of the leftmost limit point, lying in the 'safe region', can be considered an acceptable amplitude, due to there being a singular solution, or a point where the high amplitude island has yet merged with the main response. Any excitation amplitude greater than leftmost limit point will allow the system to jump to the higher amplitude.

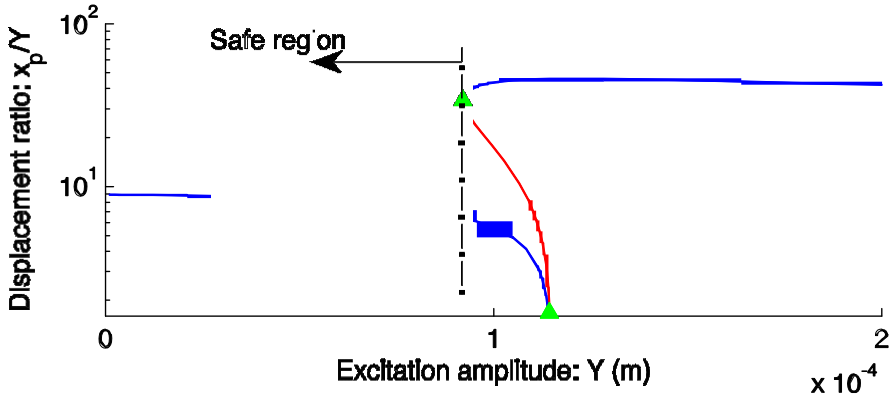

Figure 4.24: Primary displacement ratio as a function of force amplitude for $\Omega = 50(\Omega)$.

Figure 4.25 shows the FRPs at the force amplitudes of $Y = 9.22 \times 10^{-5}\ (m)$ and $Y = 1.143 \times 10^{-4}\ (m)$, corresponding to the two limit points from Fig. 4.24. In Fig. 4.25(a), the large amplitude island is disconnected and has no smooth transitions to the lower branch, indicating that it will not be a strong attrac-

tor. Numerical integrations for many initial conditions always found the lower ampli-

tude level to be dominant. In Fig. 4.25(b), the two response amplitudes have switched, the lower amplitude not becoming an island within the large amplitude response. This implies that the larger amplitude branch is the main attractor for the response. Again, many numerical integrations with various initial conditions were conducted, where it was found that the response always was attracted to the higher amplitude.

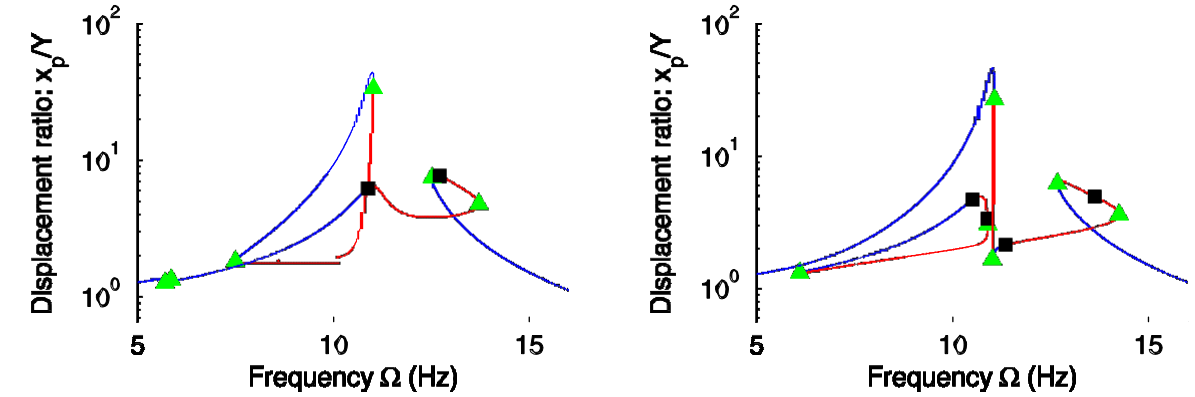

a) b)

Figure 4.25: FRP for $R_{load} = 50(\Omega)$: a) $Y = 9.22 \times 10^{-5}$(m), b) $Y = 1.143 \times 10^{-4}$(m)

Figure 4.26 shows the displacement ratio as a function of excitation amplitude for different load resistances. For high load resistances giving low damping the safe region is decreased, while higher resistances and damping will extend the operating range. Table 4.3 lists the maximum excitation amplitudes Y_{max} for the four plotted load resistances.

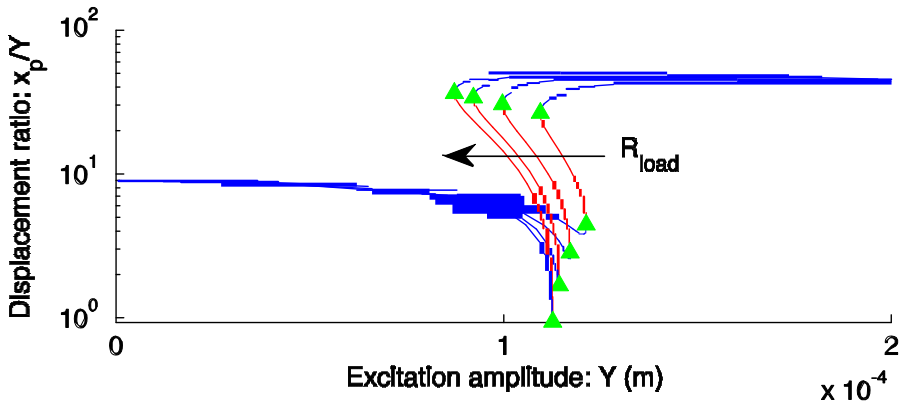

Figure 4.26: Primary displacement ratio as a function of force amplitude, arrow indicating an increase in load resistance. Lines correspond to a load resistance of 12, 25, 50 and 100 (Ω).

Table 4.3: Maximum excitation amplitudes for various resistances.

$R_{load}(\Omega)$	$Y_{max}(m)$
12	1.94×10^{-4}
25	9.961×10^{-5}
50	$9.218 \times^{-5}$
100	8.722×10^{-5}

As long as the excitation amplitude Y remains in the safe zone the NES performs as an excellent vibration absorber. The NES is capable of providing wide band vibration attenuation and may exhibit strongly modulated to periodic responses.

4.2.3.2 High Amplitude Excitation

Once the excitation amplitude increases past the safe region, wideband vibration absorption is lost. Figure 4.27 shows the FRP for an excitation amplitude of $Y = 0.001$ (m) for various load resistances. The effect of passing the safe region is clearly seen; when the system is close to the primary natural frequency there is minimal vibration absorption.

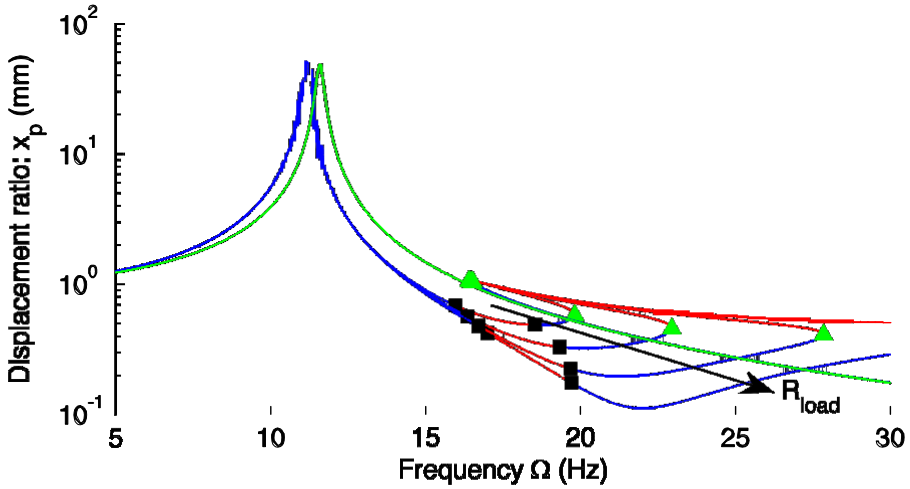

Figure 4.27: FRP for $Y = 0.001$ (��) with changing load resistance, arrow indicating an increase in load resistance. Response lines correspond to a load resistance of 12, 25, 50 and 100 (Ω). Green line represents primary system with NES disengaged.

A change in load resistance yields no improvement for the system at the first peak. At higher frequencies it has the same effect as in the low excitation amplitude, there is an extension of the region with multiple solutions, which can lead to either good or poor vibration absoption.

Although at the higher excitation amplitudes, the vibration absorption may be compromised, there still exists some regions of good absorption. Figure 4.28 depicts the FRP for $Y = 0.00015$ (��) and load resistances of 25, 50, and 100 (Ω). This represents a level of excitation amplitude just past the safe level. Regions lying to the left of the dashed lines show an increase in amplitude, but there is excellent vibration attenuation at frequencies lying to the right.

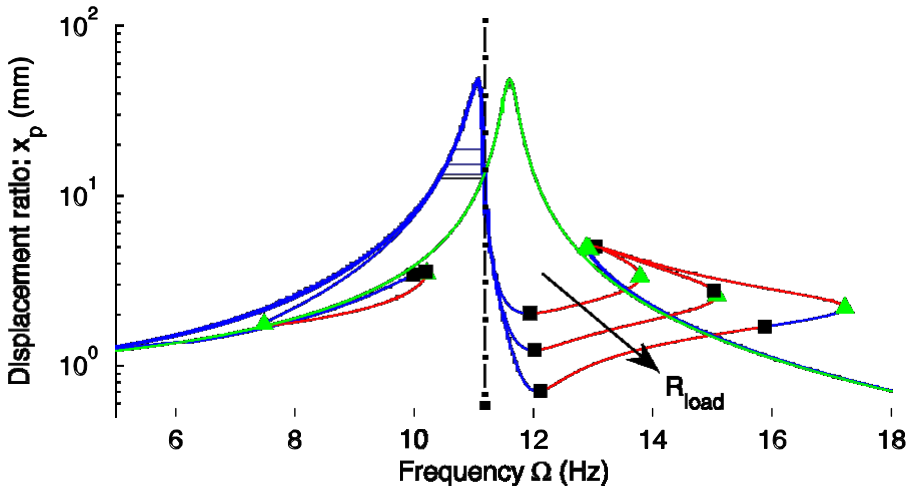

Figure 4.28: FRF for $Y = 0.00015(\Omega\Omega)$ with changing load resistance, arrow indicating an increase in load resistance. Response lines correspond to a load resistance of 25, 50 and 100 (Ω). Green line represents primary system with NES disengaged.

For high excitation amplitude levels, the choice of using a NES as a vibration absorber may be acceptable, if one knows the range of frequencies and amplitudes that will excite the system. It is critical though to be aware of these factors when choosing a design. It is interesting to note that this fact is not explicitly detailed in the existing NES literature, and no method for selecting a safe working amplitude has been described.

4.2.4 Energy Harvesting

Using the MSHBM method has another distinct advantage; that the relative amplitude of the system is explicitly described which is useful in determining power output. With the maximum amplitude described, the velocity can be approximated by taking the first derivative with respect to time of Eqn.(4.81), and the peak velocity determined by the amplitude:

$$\Omega\Omega(\Omega\Omega) = -\Omega\Omega\Omega\cos(\Omega t + \beta) \tag{4.86}$$

$$\Omega\Omega_{pw\Omega\Omega} = -\Omega\Omega\Omega \tag{4.87}$$

Combining this with Eqn.(2.29) the peak power across the load of the system can be defined as:

$$P_{pwr} = \frac{k^2 R_l}{(2\zeta_{tot} + \zeta_l)^2 b\,\Omega} \qquad (4.88)$$

The maximum theoretical power can be equated by setting:

$$\frac{dP_{pwr}}{d\zeta_l} = 0 \qquad (4.89)$$

which results in $\zeta_l = 2\zeta_{tot}$. This is known as resistance matching. Although this predicts a maximum power output at $R_l = 12\,(\Omega)$, it does not take into account the effect of damping or the nonlinear response of the system.

To examine the energy harvesting for low excitation amplitudes and the effect of the load resistance, the amplitude of excitation is set to the safe value for $R_l = 100\,(\Omega)$, insuring that the higher amplitude branch is not reached.

Figure 4.29 shows the FRP and the peak power for this input for varying resistances. Here the invalidity of Eqn.(4.89) reveals itself. As the load resistance is increased the peak power also increases, but with a change in frequency. The most reliable and best performing resistance is approximately $R_l = 25\,(\Omega)$, where there is minimal loss with some slight increases in frequency range.

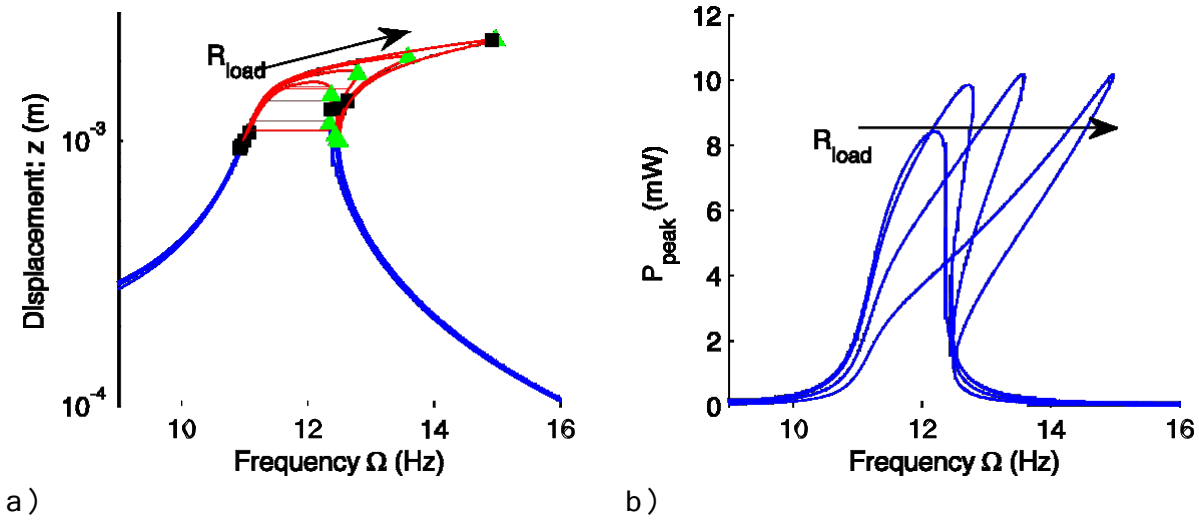

Figure 4.29: a) FRP for relative displacement and b) peak power as a function of frequency: $Y = 8.722 \times 10^{-5}$(□□) with changing load resistance, arrow indicating an increase in load resistance. Response lines correspond to a load resistance of 12, 25, 50 and 100 (Ω).

The power output represented in Fig. 4.29(b) is a very high approximation for the power output. Figure 4.29(a) shows that all of the locations of the highest output power are regions of SMRs, where the amplitude and phase of the system constantly change. This makes the assumption that the velocity can be estimated by Eqn.(4.86) invalid. The important fact is that the system achieved a design goal, that successful energy harvesting could be achieved without effecting vibration absorption.

To examine the high amplitude excitation, the values used in Fig. 4.28 ($Y = 0.00015$ (□□)) will be used to represent an excitation amplitude just past the safe amount. Figure 4.30(a) shows the FRP for various resistances. As with the previous example, as the resistance is increased the range of the frequency range is extended. In terms of power, it is clear that a decrease in resistance causes the power to increase but the frequency range is shortened.

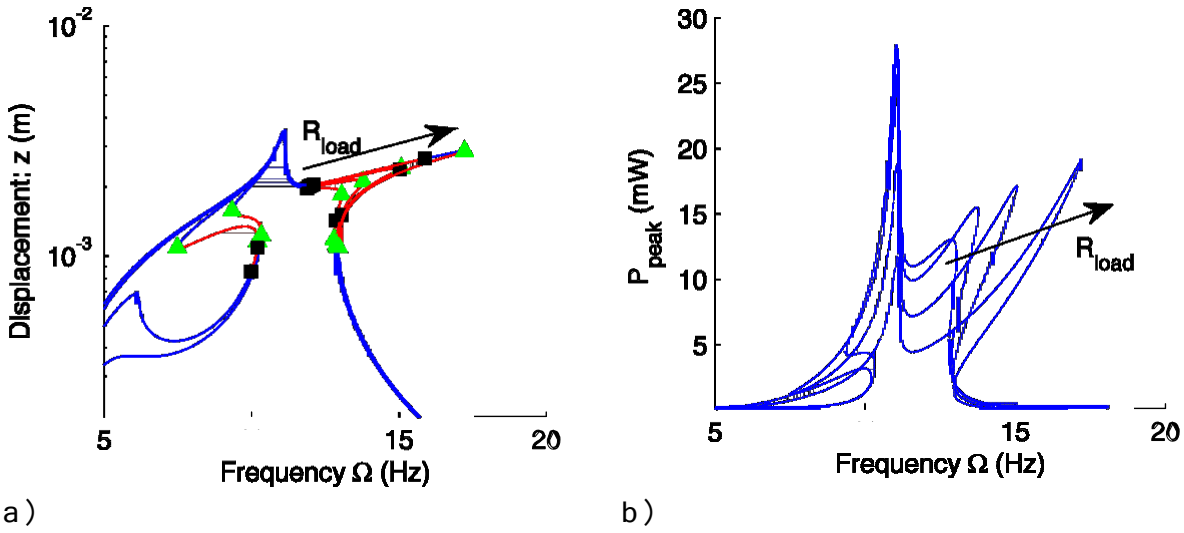

Figure 4.30: a) FRP for relative displacement and b) peak power as a function of frequency: $Y = 0.00015(\ddot{x})$ with changing load resistance, arrow indicating an increase in load resistance. Response lines correspond to a load resistance of 12, 25, 50 and 100 (Ω).

It is apparent that the energy harvesting ability of the NES does not interfere with overall performance. In fact the ability to change the damping of the system allows one to easily modify the system to match environmental conditions. If a broad range of frequencies are expected then the damping can be lowered to induce wider band energy harvesting, though this comes at the possibility of the jump phenomenon causing lower outputs.

4.3 Conclusion

The analytic analysis has showcased some of the very interesting features and attributes of the nonlinear energy sink. Furthermore it showed that theoretically a NES could be modified such that it is able to harvest energy. For the transient response, it was found that there is a critical energy threshold for the NES to be engaged, and initial energy levels just past that threshold resulted in excellent vibration and energy harvesting. At higher initial energy levels the system was still performed well, sinking vibrational energy to the NES where it could be harvested.

For the harmonically forced analysis, the performance of the NES was divided into two main responses, low and high excitation levels by deriving a set of four equations describing amplitudes and phases of the system. The low energy levels had excellent vibration absorption for all excitation frequencies while yielding harvestable power. The high excitation amplitude demonstrated a reduced region of vibration absorption, resulting in the loss of wideband vibrational attenuation, but still showing the capability of good vibration suppression. With the increase in excitation amplitude, there was also an increase in available output power.

These results verify the original idea for this work, and the method of introducing energy harvesting to a NES. The low mechanical damping of the beam allows for good vibrational energy transfer from mechanical to electrical while maintaining all the characteristics of a NES.

Chapter 5

Apparatus Testing

5.1 Testing Setup

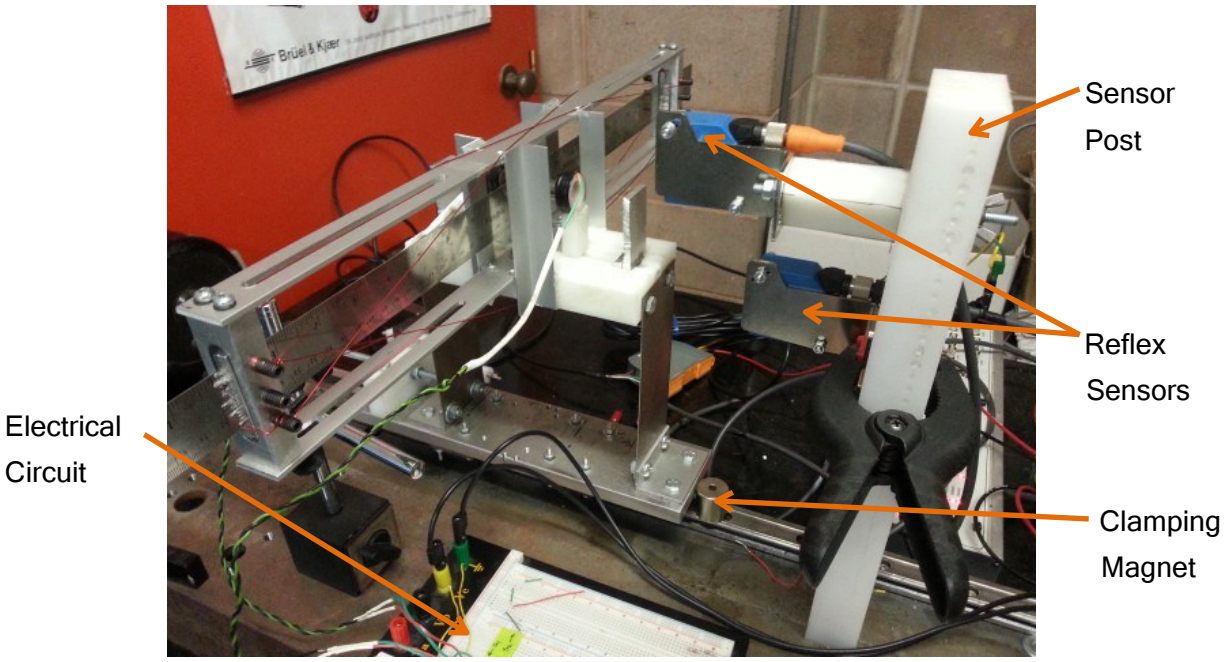

Figure 5.1: Image of the apparatus testing.

Figure 5.1 shows the basic setup for the testing of the apparatus. The reflex sensors which measure displacement (only two are shown), are mounted on a rigid sensor post which is rigidly fixed to ground. The electrical circuit is mounted

on a test breadboard so that the two coils are connected in series and connected to a load resistor, a $2000\,(\Omega)$ potentionmeter. For transient testing, two large clamping magnets are fixed to the linear track on either ends of the base fixing it, and are removed for harmonic testing.

5.2 Transient Response

Testing the transient response of the apparatus was conducted in the same method as the analytic analysis. The primary system was displaced by a distance ⬚, such that the initial conditions were equal to ⬚$_p(0) =$ ⬚, ⬚$_a(0) =$ ⬚, ⬚$_p(0) = 0$, ⬚$_a(0) = 0$. A bar with an adjustable set screw was placed between the primary mass and the sensor post, displacing it by ⬚. The bar was then quickly removed and the response recorded.

Figure 5.2 shows the recorded response for $X = 1.085 \times 10^{-3}\,(m)$ and ⬚$_{load} = 50\,(\Omega)$, close to the optimal initial energy level. The system shows very good vibration absorption, which can be attributed to the nonlinear beating that occurs at the beginning of the response.

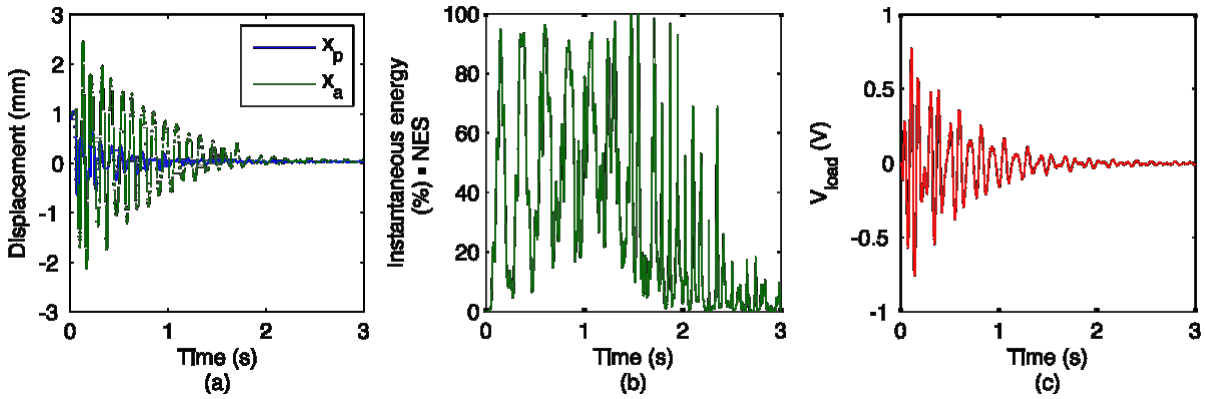

Figure 5.2: Experimental results for $X = 1.085 \times 10^{-3}$(⬚) and ⬚$_{load} = 50(\Omega)$: (a) displacements (solid line: primary system; dashed line: NES); (b) percentage of the instantaneous total energy in the NES and (c) voltage across load resistor.

The nonlinear phenomenon is clearly seen in the instantaneous energy within

the NES where rapid exchanges of energy from the primary system to the NES occur, here as with the simulation the energy must be consumed through the elec-

trical damping causing good vibration reduction. The measured voltage across the resistor is a good match to the simulation results shown in Fig. 4.2.

Figure 5.3 shows the response to an initial displacement of $X = 1.949 \times 10^{-3}\ (m)$ and $R_{load} = 50\ (\Omega)$. Here the first moments consist of the nonlinear
beating which causes a large reduction in the primary amplitude. The two systems then enter into 1:1 resonance and the energy is localized to the NES in an irreversible way, causing the amplitude of the primary system to decreases monotonically. The physical test also takes longer to eliminate the primary vibration as compared to the results in Fig. 4.3, indicating that the actual electrical damping may be less than the analytically derived quantity.

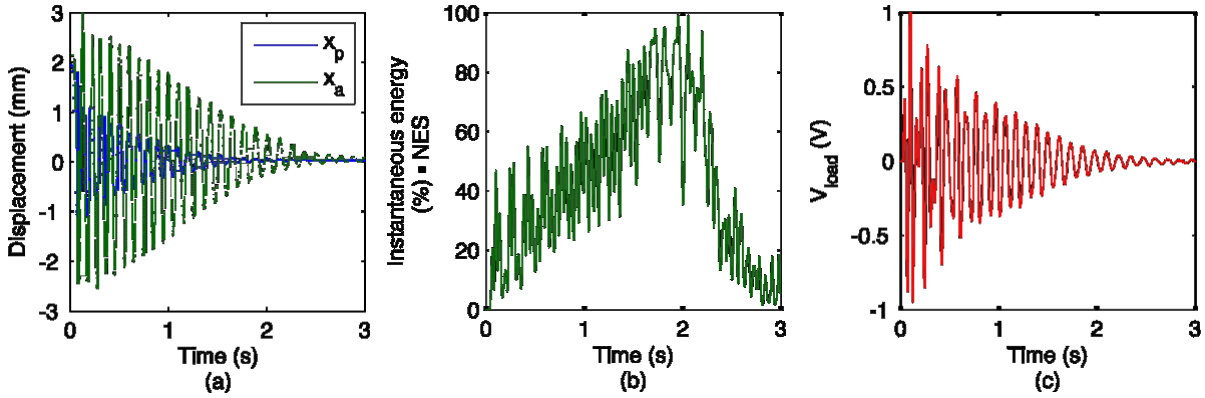

Figure 5.3: Experimental results for $X = 1.949 \times 10^{-3}$(m) and $R_{load} = 50(\Omega)$: (a) displacements
(solid line: primary system; dashed line: NES); (b) percentage of the instantaneous total energy in the NES and (c) voltage across load resistor.

Increasing the initial displacement to $X = 3.172 \times 10^{-3}$ (m) with R_{load} = $50\ (\Omega)$, Fig. 5.4 shows a similar response to that of Fig. 5.3. In this case the nonlinear beating is not as prominent, and the instantaneous energy to the NES is minimal. From the percentage of the instantaneous energy in the NES it is clear that TET is occurring, as the energy is being directed to the NES during the length of the response.

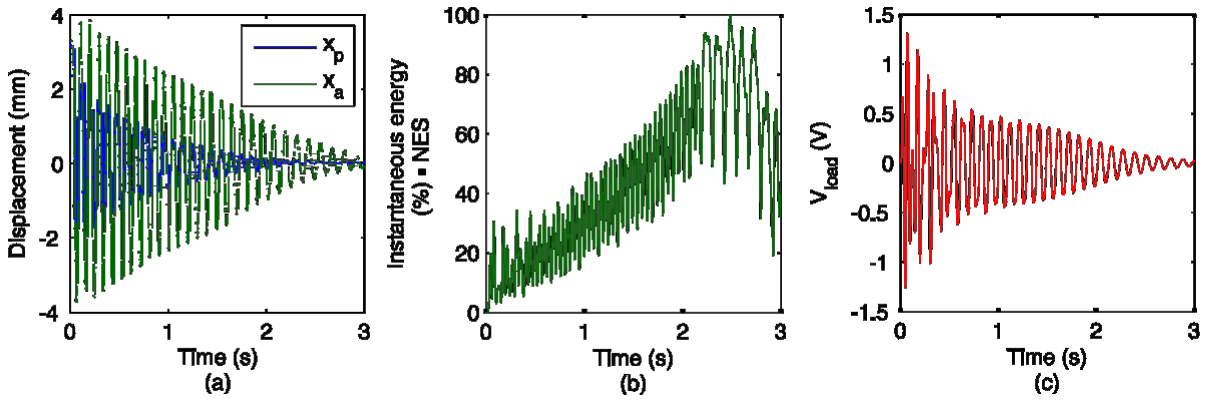

Figure 5.4: Experimental results for $X = 3.172 \times 10^{-3}$(m)and $R_{load} = 50(\Omega)$: (a) displacements (solid line: primary system; dashed line: NES); (b) percentage of the instantaneous total energy in the NES and (c) voltage across load resistor.

The wavelet transform was then applied to the relative displacements of the three test results and plotted with respect to the total system energy at each moment. The total system energy was fitted with an exponential function to remove noise, and the results given in frequency energy plots along with the back bone curve S11±, which were obtained analytically. Figure 5.5(a) shows the results for $X = 1.085 \times 10^{-3}\,(m)$ corresponding to an initial energy of $0.00287\,(\mathrm{J})$. Here as with the analytic results, the energy level is just past the critical threshold, resulting in strong nonlinear beating, after which the system is attached to the S11+ frequency curve. Figure 5.5(b) displays the results for the second test at $X = 1.949 \times 10^{-3}$ (m) with an initial energy of 0.00926 (J). With the increase in the initial energy there is less nonlinear beating and the response is quickly attracted to the S11+ curve when the system reaches 1:1 resonance. The response for Fig. 5.5(c) shows much less nonlinear beating, with higher frequencies being less dominant, resulting in the longer TET.

The most interesting feature of these plots are that at lower energy levels the frequency does not follow the S11+ curve exactly, but is attracted to a frequency of approximately $7.5\,(\mathrm{Hz})$. At the lower energy levels the displacement of the NES is small, engaging mainly the linear stiffness, implying that the linear stiffness may be slightly greater than the approximated value of 50 (N/m). This may be explained because the stiffness measurements were done through forced dynamic

testing, and might not have accurately captured the linear component. It appears that the slight increase in linear stiffness does not heavily affect performance.

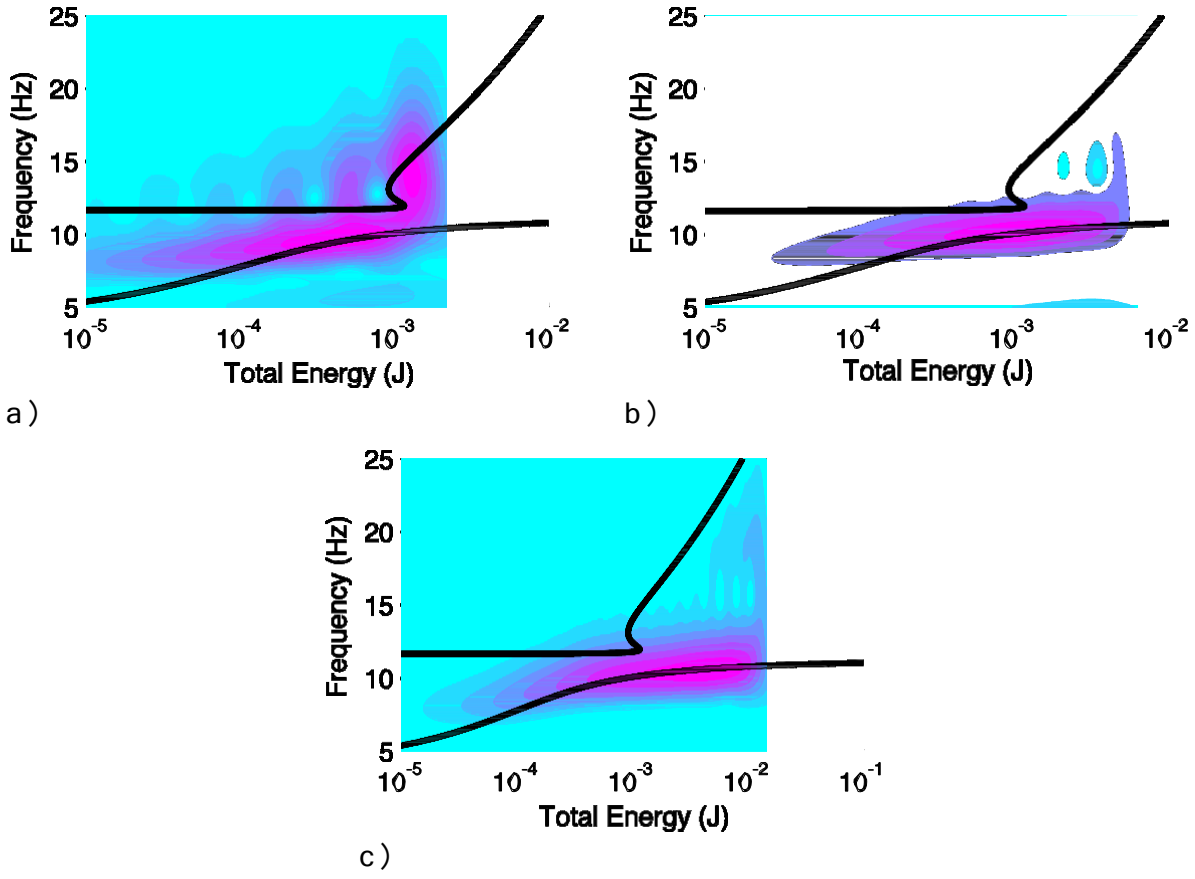

Figure 5.5: FRPs of WT from the relative response of the 3 tests with superimposed backbone curves SM± with $\hat{x} = 3.172 \times 10^{-3}$ (m), b) $\hat{x} = 1.949 \times 10^{-3}$ (m), and c) $\hat{x} = 3.172 \times 10^{-3}$ (m).

Lastly the potential for energy harvesting is investigated. The total energy consumed by the load resistor was calculated by Eqn.(4.26), as well as the initial energy for the three tests. The percentage of the energy through the load resistor was then expressed as a percentage of the initial energy, the results given in Table 5.1. The table also lists the values predicted by the simulations with the same initial conditions as the tests.

Table 5.1: Comparision of harvested energy to predicted harvested energy.

Initial Displacement	E_{init} (J)	E_{harv}	η_{harv}%	Predicted: η_{harv}%
$X = 1.085 \times 10^{-3}$	0.00287	0.0015	52.3	61.1
$X = 1.949 \times 10^{-3}$	0.00926	0.0037	40.0	47.73
$X = 3.172 \times 10^{-3}$	0.0245	0.0067	27.3	32.3

The results are a generally good agreement, all percentage of the initial energies consumed by the load resistor being within 15% of the predicted value. This variation may be explained by assumption in deriving the transduction factor; mainly that the coils were perfectly made. The coils were wound by hand and may have some inconsistences throughout.

The NES is still capable of good energy harvesting and vibration absorption, performing especially well when the initial energy is just past the critical threshold. With better constructed coils the NES may be capable of matching the predicted energy harvesting capabilities.

5.3 Harmonically Excited Testing

Testing the system with a harmonic excitation was conducted with a series of frequency sweeps, but provided some distinct challenges to overcome. The base of the system is driven by shaker, which in turn causes the entire system to vibrate. The problem with this arrangement is that the system is in fact a three-degree of freedom system, the additional degree being the base and shaker system which has its own stiffness and damping. This means that if the input voltage to the shaker amplifier is kept constant, the displacement of the base is not constant at all frequencies but will vary depending on the dynamics of the primary and NES system, making it difficult to compare to the analytic results which assumed a fixed excitation amplitude.

To overcome this, all results in the analytic and experimental outcomes are displayed in the displacement transmissibility ratio. Displaying results in this manner makes the analytic and experimental results directly comparable, as the primary amplitude will always be expressed with respect to the base amplitude.

Because the base excitation amplitude varies at different frequencies depending on system dynamics, it is important to keep the force applied to the system fixed to insure that energy levels remain constant. For an electronic shaker, the amount of force generated is proportional to the amount of current applied to the coil within the shaker. Therefore it is important to keep the current being delivered to the shaker constant at all frequencies. In the following tests the current was maintained at a constant value and the root mean square (RMS) value reported. The RMS current value will also be used as a way to distinguished between excitation levels, and to be comparable to the analytic results.

To test the validity of this, a FRP of the primary system displacement with detached NES was done at a constant RMS amperage of 0.7 (��) . Figure 5.6
shows the comparison of the analytic to the experimental displacement ratio. The good match indicates that the method is valid.

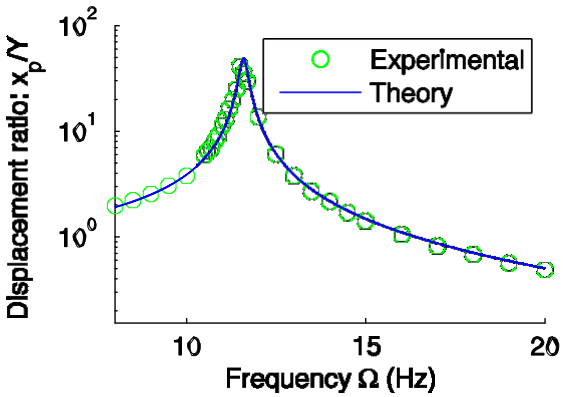

Figure 5.6: Comparison of the analytic and experimental frequency response of the primary system for shaker current of ??_{RRR} =

0.7(??

The tests were conducted using a forward frequency sweep, starting at a low excitation frequency and slowly increasing the frequency in 0.25 (Hz) increments. If a jump occurred, the frequency of the jump was recorded and the system was struck so as to bring the amplitude back to the original one before the jump, and, then the frequency sweep resumed. Once the system could no longer be made to jump back up to the original amplitude the forward sweep was concluded. The

same procedure was then followed for a backwards sweep, this time only noting the point where the system jumped to the higher frequency.

To calculate the displacement transmissibility ratios, the amplitude peaks of the base, primary, NES and relative displacement of the recorded response were determined and the average of those peaks taken. The average amplitude peaks were then divided by base peak average to find the displacement transmissibility ratio. If the response was modulated, an average of the modulated peaks was used.

The first test was conducted for a shaker current of $I_{rms} = 0.7$ (A)

and

$R_{load} = 50\ (\Omega)$, with the results shown in Fig. 5.7. The response shows good vi-

bration absorption around the natural frequency of the primary mass, which is the main area of concern. Similar to the high excitation analytic results, there is a shift in the peak natural frequency, so that the first peak occurs at 10 (Hz). Unlike the analytic results the displacement ratio of the primary system is lower than the analytic, giving better results than the predicted values for that peak. At higher frequencies the forward sweep revealed the first jump in amplitudes at 13.5 (Hz), while the backward sweep had a jump at 13 (Hz).

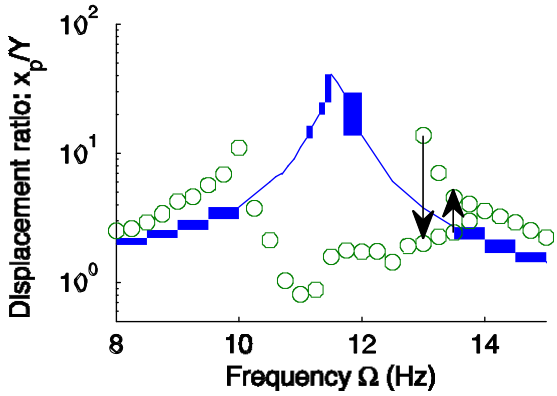

a)

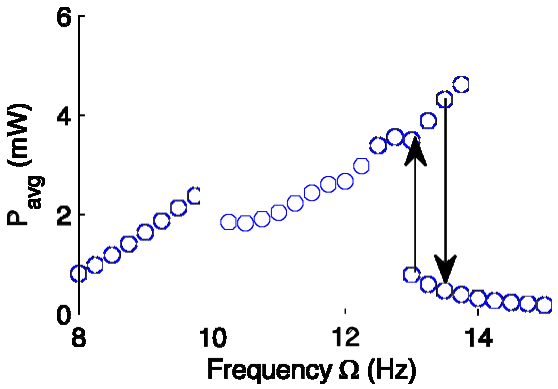

b)

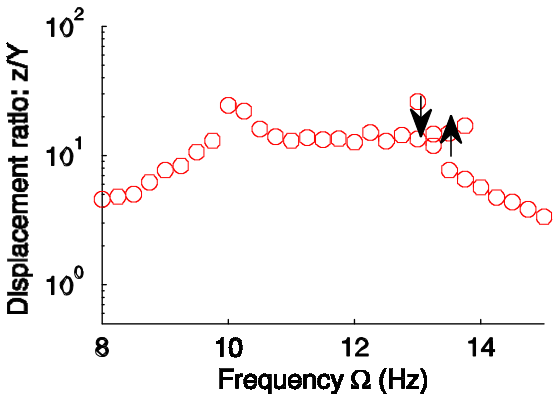

c)

Figure 5.7: Test results for a shaker current of $I_{RRR} = 0.7(A)$ and $R_{load} = 50(\Omega)$. a) displacement ratio, blue line experiment results with NES removed; b) average power consumed by the load resistor; c) relative displacement ratio.

Figure 5.7(b) shows the average power consumed by the resistor. The jump phenomenon is visible for the forward and reverse frequency sweeps, corresponding to the high and low branches of the relative displacement. The figure clearly shows the main goal of this work, that the absorber works effectively as a vibration absorber while being able to produce useable energy. At higher frequencies, more power is available but there is an increased chance of a jump and lower power levels realized.

In Fig. 5.8, the same current is used as the previous test but with a load resistance of $R_{load} = 26.3\ (\Omega)$. With the higher amount of damping, there is a reduction in the first peak as well as a greater shifting of the peak frequency to approximately 9.75 (Hz). The jump phenomenon is less significant in this case, as there is a single jump frequency for both forward and reverse sweeps at approximately 12.75 (Hz). This is confirmed by the analytical analysis where at higher damping the region of multiple solutions is greatly reduced. With the lower load resistance there is a slight increase in the average power, as it approaches the theoretical optimal power at $R_{load} = 2R_{coil}$. The importance here is that there is usable power being generated, while overall the vibration suppression is good, especially in the region of the primary resonance.

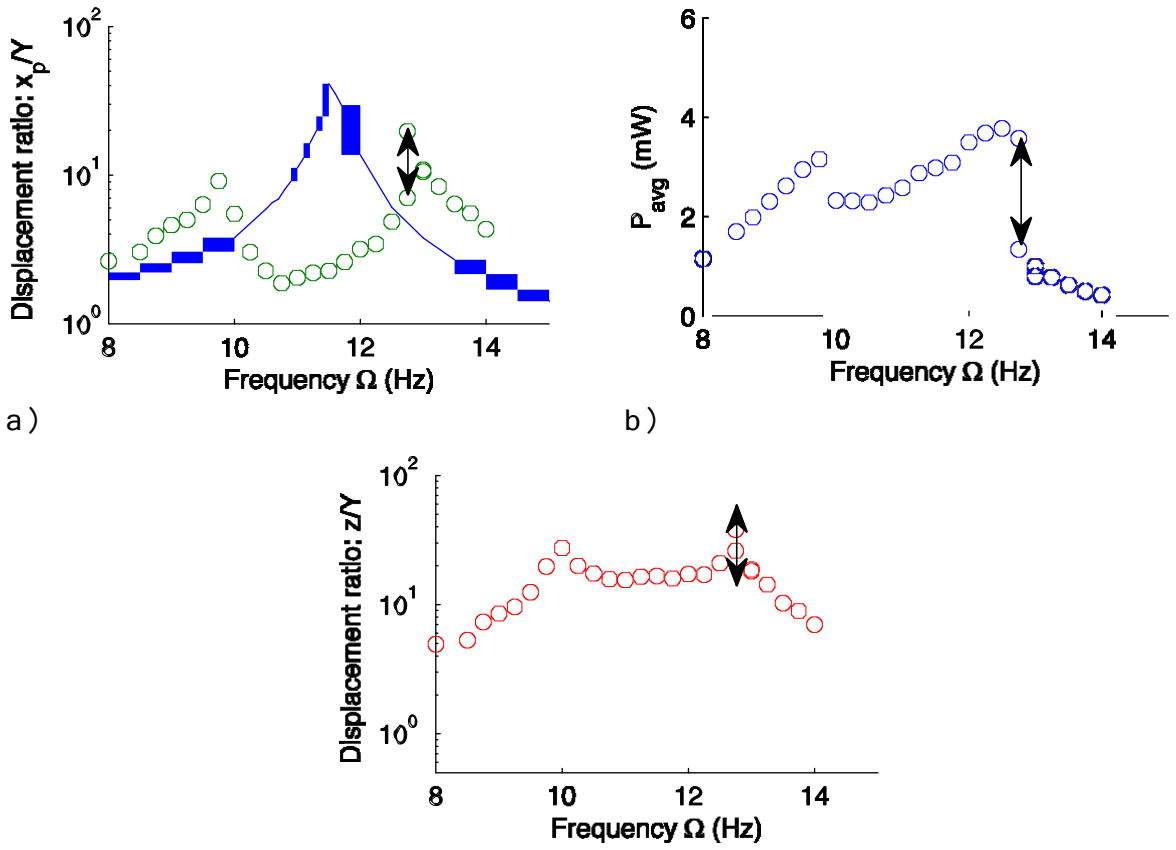

Figure 5.8: Test results for a shaker current of $I_{RRR} = 0.7(A)$ and $R_{load} = 26.3(\Omega)$. a) displace- ment ratio, blue line experiment results with NES removed; b) average power consumed by the load resistor; c) relative displacement ratio.

In both of these tests it is clear that there is some deviations from the analytic results. It seems that the displacement ratio responses of the primary system neither fit into the low or high excitation categories. This may be explained by the way that the tests were conducted with the devices available. The first problem is that the Brüel & Kjær type 4809 shaker used for the test, has a nonlinear force to frequency curve for frequencies below 10 (Hz) and for low amperage.

The second problem is due to the inertia of the system, and the definition of the 'safe' excitation amplitude to induce the low response. Considering that for a load resistance of $R_{load} = 50(\Omega)$ the maximum displacement for the low amplitude given from the analytic portion is $Y = 9.22 \times 10^{-4}(m)$, it is extremely hard to

achieve a force from the shaker that is proportional to this displacement. The shaker needs to provide enough force to overcome the dynamic friction of the linear slide bearing as well as the inertial mass, an unforeseen problem during the construction of the apparatus.

The first two tests can then be viewed as a mixture of high and low excitation amplitudes, displaying traits of both. Although these results seem somewhat different from the analytic results, it is the performance that is important. Even with these variations the NES still has a very robust response to varying inputs, greatly minimizing the primary amplitude at the resonant frequency. The amplitude gains at other frequencies may be acceptable depending on the application.

Figure 5.9 demonstrates the interesting phenomenon of SMRs; for the test $\varepsilon_{RR} = 0.7$ (Hz) and $\omega_{nom} = 26.3\ (\Omega)$. The response was recorded at the frequency
of 11.5 (Hz) and shows a strong modulation for the primary system while the relative response exhibits a weakly modulated response. During all system tests, SMRs would appear occasionally but not with the expanded range predicted by the analytic results. This may be explained in part by being limited to high excitation amplitudes, where regions of SMRs are greatly reduced.

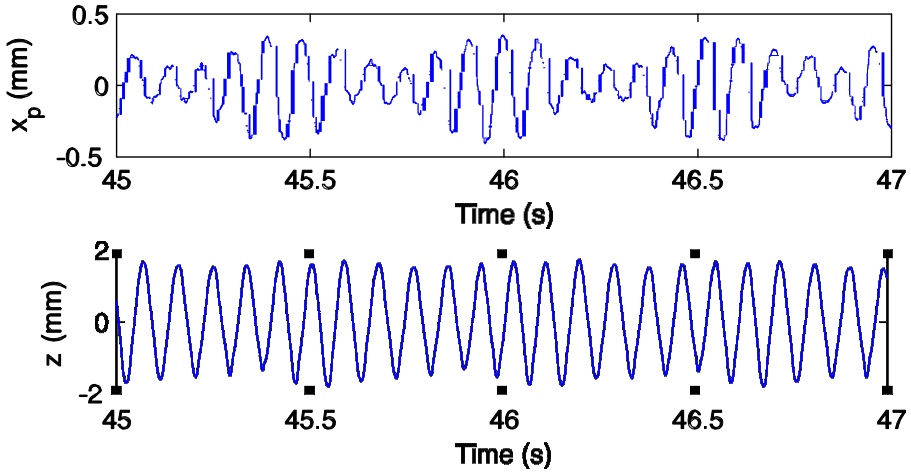

Figure 5.9: Recorded displacement response for $\varepsilon_{RR} = 0.7$ (Hz) and $\omega_{nom} = 26.3\ (\Omega)$ and a excitation frequency of 11.5 (Hz).

Increasing the shaker current to $\ddot{Y}_{RRR} = 1\ (\ddot{Y})$ and with a load resistance of $R_{load} = 26.3\ (\Omega)$, the response in Fig. 5.10(a) shows a closer match to the analytic results at high excitation level. As with the previous tests, there is a decrease in the first peak from the analytic prediction. There is some gain in the higher frequencies compared to the analytic results which should more closely follow the results from the removed NES response. On the forward sweep the system experienced the first jump at 15 (Hz) while the reverse sweep produced a jump at 14 (Hz). With the increase in driving force there is a corresponding increase in the power in the system.

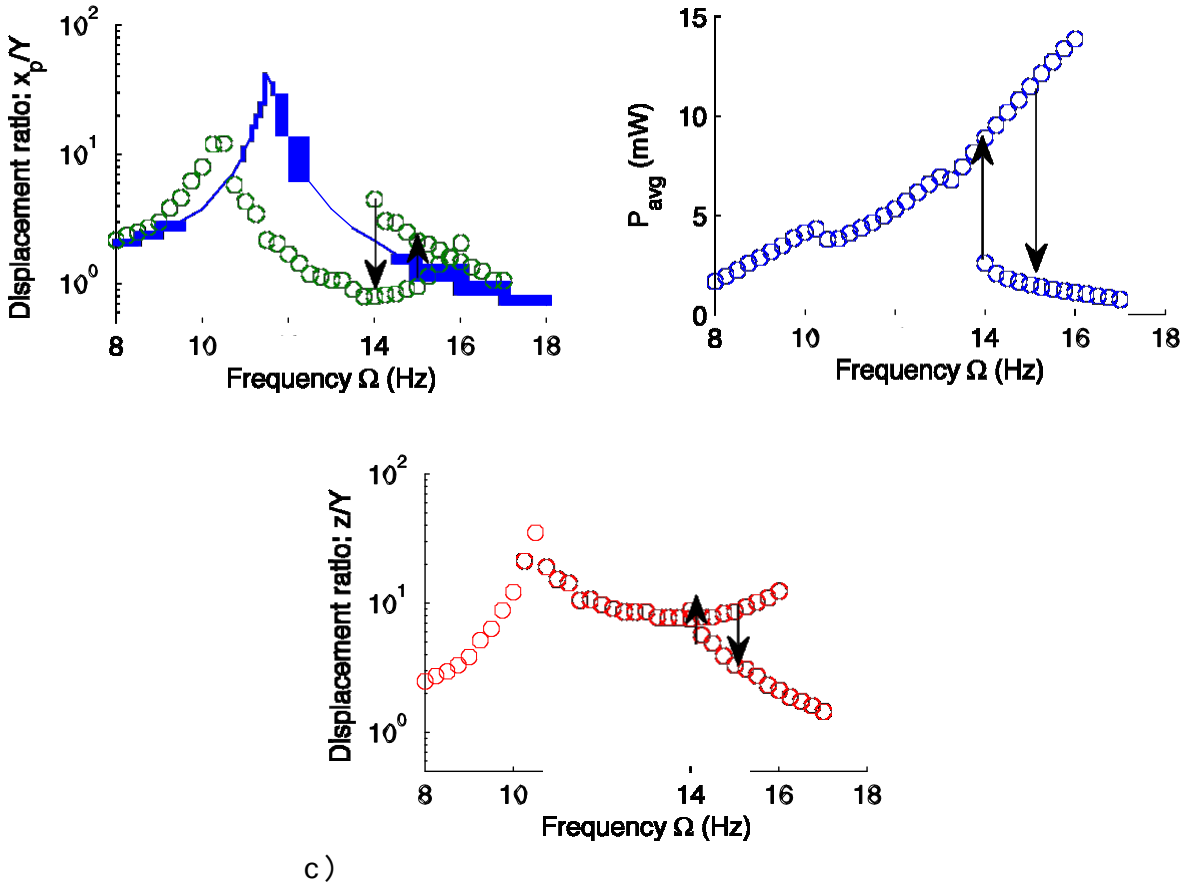

c)

Figure 5.10: Test results for a shaker current of $\ddot{Y}_{RRR} = 1(\ddot{Y})$ and $R_{load} = 26.3(\Omega)$. a) displace- ment ratio, blue line experiment results with NES removed; b) average power consumed by the load resistor; c) relative displacement ratio.

In the final test presented, the shaker was driven with a current of $I_{RMS} = 1.5$ (A) and $R_{load} = 26.3\ (\Omega)$. The response for the system is a good

match to the analytic results. The low frequencies as well as the high frequencies follow the response of the primary mass response very closely, with a slight offset in the first peak. The region of multiple solutions is very distinct, with the first jump occurring at 18 (Hz) for the forward sweep and the second occurring at 16.75 (Hz). Most impressive is the output power of the system, at low frequencies the system can output approximately 2.8 (mW) up to approximately 18.79 (mW) for the single response point at 16 (Hz). Passing this point the system can induce higher power outputs but may result in a jump to lower values.

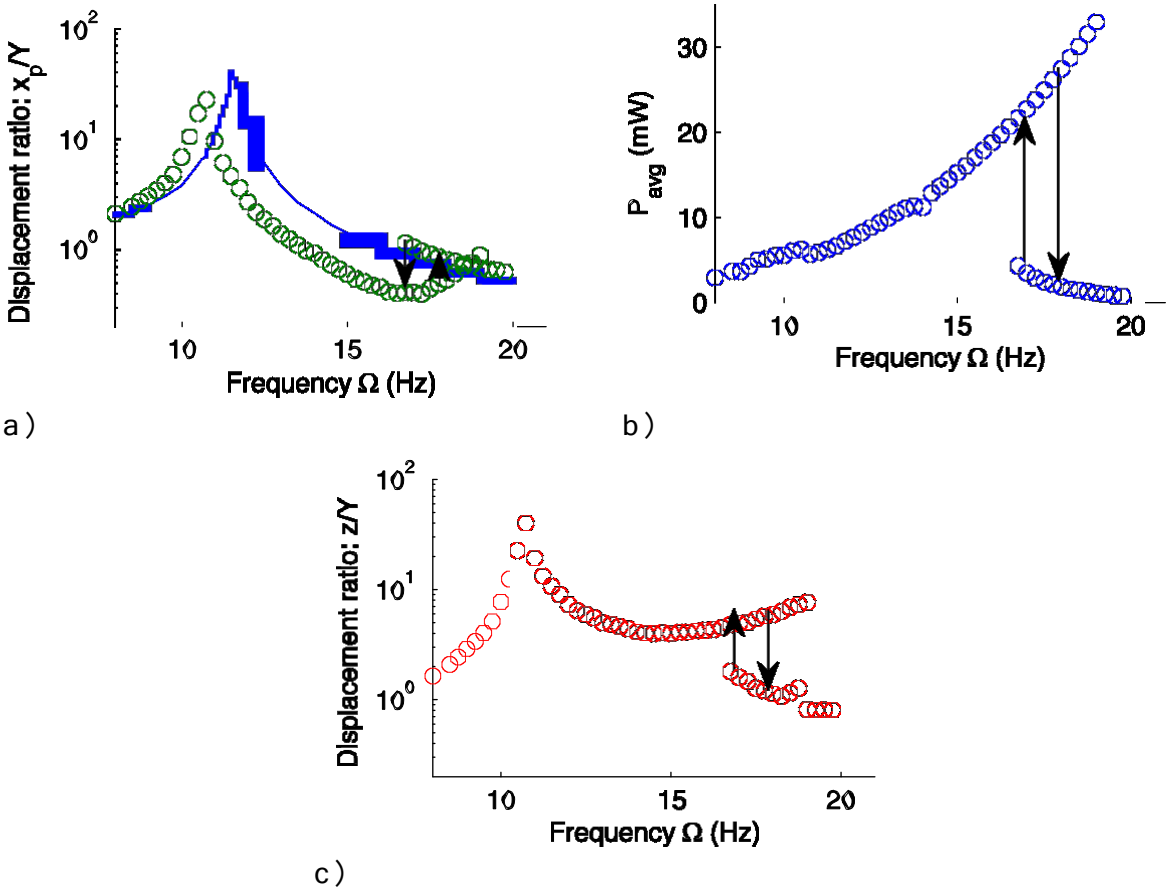

Figure 5.11: Test results for a shaker current of $I_{RMS} = 1.5$(A) and $R_{load} = 26.3(\Omega)$. a) displacement ratio x_p/Y, blue line experiment results with NES removed, red average power consumed by the load resistor; c) relative displacement ratio.

5.4 Conclusion

The testing of the device demonstrated that the main objective of this work was achieved, and proved the original design concept; that a NES could be modified to in such a way that the damping effects of the NES could be harnessed into usable power.

The transient testing revealed that the system was a close match to the analytic model. A critical input energy level exists for the NES to be engaged, and energy levels just passed that threshold will induce nonlinear beating resulting in excellent vibration absorption. Any energy levels pass this point will result in less nonlinear beating at the beginning of the response, and will result in the NES and primary masses entering into a 1:1 resonance where vibrational energy is localized to the NES and dissipated through damping.

The harmonic excitation tests diverged from the analytic analysis for the low excitation levels due to limitations of the testing conditions, but were a good match for the high excitation levels. At the lower force levels, the results displayed characteristics of both the high and low level excitation analytic predictions, with the overall results being very good in terms of vibration suppression. In all the tests, useable power is produced within the system. The power output also has wideband characteristics, especially within the region of singular solutions, an interesting consideration if this system were modified to be only an energy harvester.

Chapter 6

Summary

The original proposal of this work was to investigate the potential of an energy harvesting nonlinear energy sink. From a review of the literature of the NES, the intention was to exploit one of the main phenomenon of the NES to generate power; namely the fact that the device sinks vibrational energy and dissipates it through damping. By directly converting the dissipated damped energy into electricity, one could then have a device that could minimize vibration while harvesting energy.

From this idea the design goals were constructed. The first design criterion was to have a system with an essential nonlinearity (minimal linear stiffness) with a small amount of mechanical damping. The solution was to mount a mass on a thin preloaded steel beam. This would provide linear motion with a high degree of nonlinear stiffness, as well as a low linear stiffness component. The preloading gave the beam an increase in displacement, while also further reducing the linear stiffness of the beam. Using a thin steel beam also had the added benefit of a low amount of mechanical damping.

The second criterion was to harvest the vibrational energy in electrical form. To do this a traditional energy harvester setup was employed by simply replacing the NES mass with magnets and surrounding them with coils. Fixing the magnets to the primary mass allowed them to vibrate when the system was excited. A low amount of mechanical damping would allow for more electrical damping, giving better energy harvesting.

With the apparatus defined, the interactions between the mechanical and electrical systems were explored. From Newton's second law the equations of motion for the system were defined. Starting from a simple single coil approach, the relationship between the changing magnetic fields from the oscillating magnets to the fixed coils was defined in terms of relative velocity. This definition included a transduction factor k_t, an essential component linking the electrical and mechanical systems. The transduction factor was then used to define the electrical damping, induced coil voltage and current.

System parameter identification was conducted starting with the primary system, using tradition linear identification methods. The next step was to determine the transduction factor. Using the software FEMM, the magnetic fields of the magnets were estimated and exported to Matlab. The radial component of the magnetic flux density was integrated over the area of a coil for different discrete placements along the entire length of the magnet. Two locations were found to have optimal k_t values, corresponding to the ends of the magnets, determining where the coils should be placed when the system is at rest. Because the coils were connected in series such that the voltages were summed, the transduction factor was then doubled to represent the effect of both coils. It was also found that the transduction factor is not constant, and changes with respect to the relative displacement. It was argued that the transduction factor could be considered as constant, due to the fact that the regions were k_t was low corresponded to low relative velocity.

The stiffness and mechanical damping of the NES were then determined through the restoring force surface method. Exciting the entire system with a slowly modulated harmonic excitation, the force at every recorded time instant was approximated. Also knowing the displacement and velocity at every time instant, a 3-dimensional averaged force surface was constructed for the displacement and velocity of the NES. The stiffness of the NES was found to have a strong nonlinearity that was nearly cubic, while having a low linear stiffness. The mechanical damping of the NES was found to be very low. The restoring force surface method was then extended to the primary system, the results matching primary parameters and verifying the method. Connecting the coils to the load resistor, the same procedure was conducted for the NES to determine the effect of the electrical damping. The

results indicated a good match to the FEM results. Combining all of the system parameters resulted in a complete system model, describing the equations of motions for the mechanical system and the electrical system.

The transient system response was studied analytically, where it was shown that there is an initial energy threshold for the NES to be engaged. If the initial energy threshold was not met the system response was dominated by the primary system and vibration absorption by the NES was minimal. The best vibrational absorption results occurred when the initial energy threshold was just passed, resulting in a nonlinear beating and good targeted energy transfer(TET). The nonlinear beating induced quick energy exchanges between the primary system and NES, which must be passed through the NES damping, quickly reducing vibrational energy. At higher initial energy levels, the nonlinear beating was reduced and the system entered into a 1:1 resonance. During 1:1 resonance the phenomenon of TET was easily visualized, as seen in the percentage of instantaneous energy within the NES plots, where vibrational energy was localized to the NES over the duration of the response. The energy being released back to the system once the majority was dissipated. The robustness of the system was then explored by altering the primary systems mass and stiffness. The NES having no linear stiffness was able to self-tune and reduce vibrations for despite these changes.

The frequency energy relationship of the system was then explored by examining the nonlinear normal modes of the underlying Hamiltonian system. Using the method of complexification, the amplitudes of the undamped system were defined with respect to a dominant frequency. Knowing the amplitudes of the system, the energy for different periodic orbits could be defined, giving the two so-called symmetric backbone curves S11±. The initial energy threshold could be visualized as the cusp of the S11- curve. A wavelet transform was applied to the four initial simulations, allowing for the calculation of the frequencies and energy at each moment in time. These were then superimposed on the backbone curves. These revealed the nature of the nonlinear beating phenomenon and its dependence on initial energy.

The effect of electrical damping and the potential for energy harvesting was determined. For higher initial energy levels, the vibration in the primary system

could be reduced by increasing the amount of damping, or reducing the load resistance. This increase in vibration suppression had the effect of reducing the amount of power available for harvesting. Comparing the percentage of initial energy dissipated through electrical damping and the percentage of initial energy consumed by the load resistor, a nondimensional term was found relating the two. It was found that the optimal load resistance would vary with the initial energy. Fortunately the optimal values were at high damping levels, therefore striking a balance between vibration suppression and energy harvesting.

The harmonically excited response analysis utilized a modified classic perturbation method. Based upon the method of multiple scales, the analysis included two harmonic balances to capture the dynamics of the system, giving 4 coupled highly nonlinear equations describing the amplitudes and phases of the primary system and the relative displacements at any excitation frequency. The equations not only described the amplitudes and phases, but also indicated when the system would experience strongly modulated responses through Hopf bifurcations, as well as the existence of multiple solutions and response stability. The stability of these equations must be regarded as a divergence from periodic solutions. The equations were then validated by numerical integration of original equations at points of stability.

Two types of responses were identified and categorized; high and low excitation levels. The distinction between these two responses was whether the system would be attracted to a high level amplitude in the lower frequency range. For low excitation levels, the higher amplitude response manifests as a closed island response, with no connection to low amplitude response for all frequencies. It was found that when this island is unconnected, it is an unattainable response, verified through numerical integration with various initial conditions.

A method for determining when the high amplitude island would become realizable was proposed. Each of the high and low excitation levels exhibit a peak amplitude frequency. By doing a continuation analysis at that frequency, for the displacement transmissibility ration and excitation amplitude, the excitation amplitude where the higher response becomes dominant can be identified. A safe excitation amplitude was defined for the low response, and the value was found to be dependent on damping.

In the case of all low excitation amplitudes, vibration damping is excellent, having broad band vibration suppression. For the high excitation amplitudes the effectiveness of the NES is minimized, but only in terms of broad band vibration absorption. With the high amplitude response realized, a peak emerges where no vibration attenuation occurs, that is slightly shifted from the primary systems natural frequency. Depending on the level of amplitude, there may be regions that exhibit excellent vibration suppression, limiting the useful range of the NES.

Regardless of which excitation category the system falls into, one fact remains; that in all cases the NES can produce useable power. The load resistance can then be selected to change the energy output performance of the system. Lower load resistances would yield higher results, but would have a less effective broadband harvesting, while higher load resistances could potentially generate more power at higher frequencies, but would be susceptible to the jump phenomenon, which would give lower power outputs.

The transient performance of the system was then tested, performed in the same manner as the analytic simulations. The results had good agreement with analytic results. The optimal initial energy corresponded to the analytically derived one, and the NES underwent nonlinear beating giving good vibration suppression. At greater initial energies the NES exhibited TET and 1:1 resonance, giving comparable results to the simulations. The wavelet transform was applied to the recorded responses and were found to be attracted to the S11+ backbone curve, as predicted by the analysis of the nonlinear normal modes. The frequency energy plots also indicated that the actual linear stiffness may be higher than the one found through the surface restoring force method. The ability to harvest transient vibrational energy proved to be possible, with measured results being approximately 15% less than predicted simulations.

Testing the system under harmonic excitation proved difficult. The goal of inducing the low excitation amplitude response was not achievable due to apparatus limitations. The results for an equivalent low excitation amplitude was interpreted as a mix of high and low excitation response. A shifted peak was observed, signifying a high excitation amplitude, but the displacement ratio was much lower, a quality of

the low excitation amplitude. Although not matching the analytic results, the performance was excellent, the NES reducing vibrations in a broadband manner. Increasing the applied shaker force, the results matched the analytic results very well. The responses showed a high amplitude shifted peak and vibration attenuation in some frequency regions.

The analysis and testing have shown that an energy harvesting nonlinear energy sink is attainable. Furthermore, the design presented in no way impedes the function of the NES, it merely harvests the dissipated vibrational energy; elegant due to its simplicity. In addition to its simplicity, the system is robust, able to compensate for changes in system parameters.

Future work may explore many interesting features of this system. This system was constructed without any tuning, as the system has the ability to self-tune due to the lower linear stiffness. For the transient response, if a repeatable initial condition is known, the system may be optimized so that the nonlinear beating phenomenon is always engaged. The same applies for the harmonically excited response. If the excitation amplitude is known, a method to optimizing the NES may be developed so that the possibility of the high amplitude branches is never realized.

The system may also be used as semi-active smart structure. The electrical system has the interesting ability to quickly change the damping by changing load resistance. Utilizing digitally controllable resistors a control scheme may be implemented that can maximize the vibrational absorption and energy harvesting abilities.

References

[1] C. R. Fuller, S. J. Elliott and P. A. Nelson, Active Control of Vibration. London; San Diego: Academic Press, c1996.

[2] I. Maciejewski, "Control system design of active seat suspensions," Journal of Sound and Vibration, vol. 331, pp. 1291-1309, 2012.

[3] W. Sun, J. Li, Y. Zhao and H. Gao, "Vibration control for active seat suspension systems via dynamic output feedback with limited frequency characteristic," Mechatronics, vol. 21, pp. 250-260, 2011.

[4] D. York, X. Wang and F. Gordaninejad, "A new MR fluid-elastomer vibration isolator," Journal of Intelligent Material Systems and Structures, vol. 18, pp. 1221-1225, 2007.

[5] Y. Sun, "Control of torsional rotor vibrations using an electrorheological fluid dynamic absorber." Journal of Vibration Control, vol. 17, pp. 1253-1264, 2011.

[6] D. J. Inman, Engineering Vibration. Upper Saddle River, N.J.: Pearson Prentice Hall, 2008.

[7] J. P. Den Hartog, Mechanical Vibrations. New York: McGraw-Hill, 1956.

[8] A. H. Nayfeh and D. T. Mook, Nonlinear Oscillations. New York ; Toronto: Wiley, 1979.

[9] A. F. Vakakis and O. Gendelman, "Energy pumping in nonlinear mechanical oscillators: Part II - Resonance capture," Journal Of Applied Mechanics-Transactions Of The ASME, vol. 68, pp. 42-48, 2001.

[10] O. Gendelman, L. I. Manevitch, A. F. Vakakis and R. M'Closkey, "Energy pumping in nonlinear mechanical oscillators: Part I - Dynamics of the underlying Hamiltonian systems," Journal Of Applied Mechanics-Transactions Of The ASME, vol. 68, pp. 34-41, 2001.

[11] E. Gourdon, C. H. Lamarque and S. Pernot, "Contribution to efficiency of irreversible passive energy pumping with a strong nonlinear attachment," Nonlinear Dynamics, vol. 50, pp. 793-808, 2007.

[12] T. P. Sapsis T.P., A. F. Vakakis A.F., O. V. Gendelman O.V., L. A. Bergman L.A., G. Kerschen and D. D. Quinn D.D., "Efficiency of targeted energy transfers in coupled nonlinear oscillators associated with 1:1 resonance captures: Part II, analytical study," Journal of Sound and Vibration, vol. 325, pp. 297-320, 2009.

[13] D. Quinn, O. Gendelman, G. Kerschen, T. P. Sapsis, L. Bergman and A. F. Vakakis, "Ef ficiency of target lators associated with 1:1 resonance captures: Part I," Journal of Sound and Vibration, vol. 311, pp. 1228, 2008.

[14] A. F. Vakakis, O. V. Gendelman, L. A. Bergman, D. M. McFarland, G. Kerschen and Y. S. Lee, Nonlinear Targeted Energy Transfer in Mechanical and Structural Systems. Toronto: Springer 2008.

[15] T. Nguyen and S. Pernot, "Design criteria for optimally tuned nonlinear energy sinks—part 1: transient regime," Nonlinear Dynamics, vol. 69, pp. 1-19, 2012.

[16] O. V. Gendelman, Y. Starosvetsky and M. Feldman, "Attractors of harmonically forced linear oscillator with attached nonlinear energy sink I: Description of response regimes," Nonlinear Dynanmics, vol. 51, pp. 31-46, 2008.

[17] G. Gatti and M. J. Brennan, "On the effects of system parameters on the response of a harmonically excited system consisting of weakly coupled nonlinear and linear oscillators," Journal of Sound and Vibration, vol. 330, pp. 4538-4550, 2011.

[18] G. Gatti, I. Kovacic and M. J. Brennan M.J., "On the response of a harmonically excited two degree-of-freedom system consisting of a linear and a nonlinear quasi-zero stiffness oscillator," Journal of Sound and Vibration, vol. 329, pp. 1823-1835, 2010.

[19] E. Gourdon, N. A. Alexander, C. A. Taylor, C. H. Lamarque and S. Pernot, "Nonlinear energy pumping under transient forcing with strongly nonlinear coupling: Theoretical and experimental results," Journal of Sound and Vibration, vol. 300, pp. 522-551, 2007.

[20] G. Kerschen, D. M. McFarland, J. J. Kowtko, Y. S. Lee, L. A. Bergman and A. F. Vakakis, "Experimental demonstration of transient resonance capture in a system of two coupled oscillators with essential stiffness nonlinearity," Journal of Sound and Vibration, vol. 299, pp. 822-838, 2007.

[21] G. Kerschen, J. J. Kowtko, D. M. Mcfarland, L. A. Bergman and A. F. Vakakis, "Theoretical and Experimental Study of Multimodal Targeted Energy Transfer in a System of Coupled Oscillators," Nonlinear Dynamics, vol. 47, pp. 285-309, 2007.

[22] D. M. McFarland, L. A. Bergman and A. F. Vakakis, "Experimental study of non-linear energy pumping occurring at a single fast frequency," International Journal of Nonlinear Mechanics, vol. 40, pp. 891-899, 2005.

[23] X. Jiang, D. M. McFarland, L. A. Bergman and A. F. Vakakis, "Steady State Passive Nonlinear Energy Pumping in Coupled Oscillators: Theoretical and Experimental Results," Nonlinear Dynamics, vol. 33, pp. 87-102, 2003.

[24] S. Roundy, P. K. Wright and J. M. Rabaey, Energy Scavenging for Wireless Sensor Networks: With Special Focus on Vibrations. Boston: Kluwer Academic, 2004.

[25] A. Erturk and D. J. Inman, "Piezoelectric energy harvesting," pp. 392, 2011.

[26] S. Hurlebaus and L. Gaul, "Smart structure dynamics," Mechanical Systems and Signal Processing, vol. 20, pp. 255-281, 2006.

[27] M.N. Fakhzan, "Harvesting vibration energy using piezoelectric material: Modeling, simulation and experimental verifications," Mechatronics, 2012.

[28] S. Priya, "Advances in energy harvesting using low profile piezoelectric transducers," Journal Of Electroceramics, vol. 19, pp. 167-184, 2007.

[29] S. Saadon and O. Sidek, "A review of vibration-based MEMS piezoelectric energy harvesters," Energy Conversion and Management, vol. 52, pp. 500-504, 2011.

[30] B.P. Mann and N.D. Sims, "On the performance and resonant frequency of electromagnetic induction energy harvesters," Journal of Sound and Vibration, vol. 329, pp. 1348-1361, .

[31] D. Spreemann, Y. Manoli, "Electromagnetic Vibration Energy Harvesting Devices," New York: Springer, 2012.

[32] B. P. Mann and N. D. Sims, "Energy harvesting from the nonlinear oscillations of magnetic levitation," Journal of Sound and Vibration, vol. 319, pp. 515-530, 2009.

[33] Yang Zhu, J. W. Zu and L. Guo, "A Magnetoelectric Generator for Energy Harvesting From the Vibration of Magnetic Levitation," IEEE Transactions on Magnetics, vol. 48, pp. 3344-3347, 2012 NOV., 2012.

[34] J. Liu and K. Liu, "A tunable electromagnetic vibration absorber: Characterization and application," Journal of Sound and Vibration, vol. 295, pp. 708-724, 2006.

[35] N. Zhou and K. Liu, "A tunable high-static–low-dynamic stiffness vibration isolator," Journal of Sound and Vibration, vol. 329, pp. 1254-1273, 2010.

[36] A. Carrella, M. J. Brennan, T. Waters and K. Shin, "On the design of a high-static-low-dynamic stiffness isolator using linear mechanical springs and magnets," Journal of Sound and Vibration, vol. 315, pp. 712-720, 2008.

[37] L. Zuo, "Design and characterization of an electromagnetic energy harvester for vehicle suspensions," Smart Materials and Structures, vol. 19, 2010.

[38] H. A. Wheeler, "Simple Inductance Formulas for Radio Coils," Proceedings of the Institute of Radio Engineers, vol. 16, pp. 1398-1400, 1928.

[39] Finite Element Method Magnetics. 2013. http://www.femm.info/wiki/HomePage

[40] S. F. Masri and T. K. Caughey, "A Nonparametric Identification Technique for Nonlinear Dynamic Problems," Journal of Applied Mechanics, vol. 46, pp. 433-447, June 1, 1979.

[41] S. F. Masri, H. Sassi and T. K. Caughey, "Nonparametric Identification of Nearly Arbitrary Nonlinear Systems," Journal of Applied Mechanics, vol. 49, pp. 619-628, September 1, 1982.

[42] K. Worden, "Data processing and experiment design for the restoring force surface method, part I: integration and differentiation of measured time data," Mechanical Systems and Signal Processing, vol. 4, pp. 295-319, 7, 1990.

[43] K. Worden, "Data processing and experiment design for the restoring force surface method, part II: Choice of excitation signal," Mechanical Systems and Signal Processing, vol. 4, pp. 321-344, 7, 1990.

[44] D. McFarland, G. Kerschen, J. Kowtko, Y. Lee, L. Bergman and A. Vakakis, "Experimental investigation of targeted energy transfers in strongly and nonlinearly coupled oscillators," Journal of the Acoustical Society of America, vol. 118, pp. 791-799, 2005.

[45] G. Kerschen, "VTT benchmark: application of the restoring force surface method," Mechanical Systems and Signal Processing, vol. 17, pp. 189-193, 2003.

[46] N. G. Stephen, "On energy harvesting from ambient vibration," Journal of Sound and Vibration, vol. 293, pp. 409-425, 2006.

[47] O. V. Gendelman, T. Sapsis, A. F. Vakakis and L. A. Bergman, "Enhanced passive targeted energy transfer in strongly nonlinear mechanical oscillators," Journal of Sound and Vibration, vol. 330, pp. 1-8, 2011.

[48] T. Pham, S. Pernot and C. Lamarque, "Competitive energy transfer between a two degree-of-freedom dynamic system and an absorber with essential nonlinearity," Nonlinear Dynamics, vol. 62, pp. 573-592, 2010.

[49] R. Bellet, B. Cochelin, P. Herzog and P. -. Mattei P.-O., "Experimental study of targeted energy transfer from an acoustic system to a nonlinear membrane absorber," Journal of Sound and Vibration, vol. 329, pp. 2768-2791, 2010.

[50] O. V. Gendelman, E. Gourdon and C. H. Lamarque, "Quasiperiodic energy pumping in coupled oscillators under periodic forcing," Journal of Sound and Vibration, vol. 294, pp. 651-662, 2006.

[51] Y. Starosvetsky and O. V. Gendelman, "Attractors of harmonically forced linear oscillator with attached nonlinear energy sink. II: Optimization of a nonlinear vibration absorber," Nonlinear Dynamics, vol. 51, pp. 47-57, 2008.

[52] A. Luongo and D. Zulli, "Dynamic analysis of externally excited NES-controlled systems via a mixed Multiple Scale/Harmonic Balance algorithm," Nonlinear Dynamics, vol. 70, pp. 2049-2061, 2012.

[53] MATCONT and CL MATCONT: Continuation toolboxes in Matlab. 2013. http://www.matcont.ugent.be/

[54] Y. Starosvetsky and O. V. Gendelman, "Response regimes of linear oscillator coupled to nonlinear energy sink with harmonic forcing and frequency detuning," Journal of Sound and Vibration, vol. 315, pp. 746-765, 2008.

[55] I. Grinberg, V. Lanton and O. V. Gendelman, "Response regimes in linear oscillator with 2DOF nonlinear energy sink under periodic forcing," Nonlinear Dynamics, vol. 69, pp. 1889-1902, 2012.

Appendix A

Four equations describing the amplitudes and phases of the system under harmonic excitation, returned to the main system parameters.

$$\frac{d}{dt}a = -\frac{1}{8}\frac{1}{\Omega\left(2R_{coil}+R_{load}\right)\sqrt{\frac{k_p}{m_p}}\,m_p}\left(\left(8bk_aR_{coil}+4bk_aR_{load}+6b^3k_nR_{coil}+3b^3k_nR_{load}\right)\sin\left(-\beta+\alpha\right)\right) - \frac{1}{8}\frac{1}{\Omega\left(2R_{coil}+R_{load}\right)\sqrt{\frac{k_p}{m_p}}\,m_p}\left(\left(-4b\Omega k_t^2-8b\Omega c_{am}R_{coil}-4b\Omega c_{am}R_{load}\right)\cos\left(-\beta+\alpha\right)\right) - \frac{1}{8}\frac{1}{\Omega\left(2R_{coil}+R_{load}\right)\sqrt{\frac{k_p}{m_p}}\,m_p}\left(-4Y\sqrt{k_p^2+c_p^2\Omega^2}\sin\left(-\alpha+\phi\right)R_{load}+8c_paR_{coil}+4c_paR_{load}-8Y\sqrt{k_p^2+c_p^2\Omega^2}\sin\left(-\alpha+\phi\right)R_{coil}\right) \tag{A.1}$$

(A.2)

$$\frac{d}{dt}\alpha(t) =$$

$$-\frac{1}{8}\frac{\left(4\,b\,\Omega\,k_t^2+8\,b\,\Omega\,c_{am}\,R_{coil}+4\,b\,\Omega\,c_{am}\,R_{load}\right)\sin(-\beta+\alpha)}{\left(2\,R_{coil}+R_{load}\right)\sqrt{\frac{k_p}{m_p}}\,m_p\,a\,\Omega}$$

$$-\frac{1}{8}\frac{1}{\left(2\,R_{coil}+R_{load}\right)\sqrt{\frac{k_p}{m_p}}\,m_p\,a\,\Omega}\left(\left(8\,b\,k_a\,R_{coil}\right.\right.$$

$$\left.+4\,b\,k_a\,R_{load}+6\,b^3\,k_n\,R_{coil}+3\,b^3\,k_n\,R_{load}\right)\cos(-\beta+\alpha)\Big)$$

$$-\frac{1}{8}\frac{1}{\left(2\,R_{coil}+R_{load}\right)\sqrt{\frac{k_p}{m_p}}\,m_p\,a\,\Omega}\Big(-8\,a\,k_p\,R_{coil}$$

$$-4\,a\,k_p\,R_{load}+8\,a\,\Omega^2\,m_p\,R_{coil}+4\,a\,\Omega^2\,m_p\,R_{load}$$

$$+8\,Y\sqrt{k_p^2+c_p^2\,\Omega^2}\,\cos(-\alpha+\phi)\,R_{coil}+4\,Y\sqrt{k_p^2+c_p^2\,\Omega^2}\,\cos($$

$$-\alpha+\phi)\,R_{load}\Big)$$

$$\frac{d}{dt} b(t) = -\frac{1}{2} \left(\left(\left(\left(\left(\frac{1}{2} R_{coil} + \frac{1}{4} R_{load} \right) c_{am} + \frac{1}{4} k_t^2 \right) \cos(-\beta + \phi) + \Omega \left(\frac{1}{2} R_{load} + R_{coil} \right) \sin(-\beta + \phi) m_a \right) Y m_a \sqrt{k_p^2 + c_p^2 \Omega^2} - \left(\Omega^2 c_p \left(\frac{1}{2} R_{load} + R_{coil} \right) m_a + \frac{1}{4} \left(\left(2 R_{coil} + R_{load} \right) c_{am} + k_t^2 \right) k_p \right) a m_a \cos(-\beta + \alpha) + \frac{1}{4} \Omega \left(-4 k_p \left(\frac{1}{2} R_{load} + R_{coil} \right) m_a + \left(\left(2 R_{coil} + R_{load} \right) c_{am} + k_t^2 \right) c_p \right) a m_a \sin(-\beta + \alpha) + \frac{3}{16} b \left(\left(2 R_{coil} + R_{load} \right) c_{am} + k_t^2 \right) \left(\frac{8}{3} m_a^2 \Omega^2 + \left(\frac{4}{3} m_p \Omega^2 + k_n b^2 + \frac{4}{3} k_a \right) m_a + \left(k_n b^2 + \frac{4}{3} k_a \right) m_p \right) \right) \left(\frac{1}{2} R_{load} + R_{coil} \right) \Bigg) \Bigg/ \left(\sqrt{\frac{k_p}{m_p}} m_p \left(\Omega^2 \left(\frac{1}{2} R_{load} + R_{coil} \right)^2 m_a^2 + \frac{1}{16} \left(\left(2 R_{coil} + R_{load} \right) c_{am} + k_t^2 \right)^2 \right) \right) \tag{A.3}$$

(A.4)

$$
\begin{aligned}
&\text{Ji(t)} = \text{(r(Rload + Rcoil) ((O (Rload} \\
&\text{+ Rcoil) macos(4>) – sin(4>) (camRload + 2Rcoilcam))} \\
&\cos(J3) + \sin(J3)\,((\ R_{0011}cam + \text{camRload} + +\ )\cos(4>) \\
&+ \sin(4>)\,O\,(\ Rload\ + Rcoil)\ ma))\ maj\ + f,o^2 \\
&+ a\,(\ O\,(-4kp\ (\ Rload\ + Rcoil)\ ma + cp\ (camRload\ + \\
&+ 2Rcoilcam))\cos(a) + (02\ (\ Rload\ + Rcotl)\ cpma \\
&+ kp\ (camRioad + 2Rcoilcam))\sin(a))\,(\ R\text{-}pad \\
&+ Rcoil)macos(Ji)\ -a(\ Rload+Rcol1)\ ((o^2\ (\ Rload \\
&+ Rcoil)\ cp\ ma + kp\ (camRload + +\ 2Rcoilcam))\cos(a) \\
&- \text{Osin}\{a)\ (-4kp\ (\ R\ pad + Rcou)\ ma + cp\ (camRload + K, \\
&+ 2Rcoilcam)))masin(J3) + Ob((-\ mP0^2 + knb^2 \\
&+ ka)\ (\ Rload\ + Rcoil\ f + ((-\ am + (kn\,b^2 \\
&+ ka)\ mp)\ R!,;I + ((+\ (\ kn\,!?- + ka)\ mp)\ Rload \\
&- cam)\ Rcoil + (-\ am + (kn\,!?- + ka)\ mp)\ Rioad \\
&- camRioad- k:)\ ma - mp\ (camR/oad + \\
&+ 2R\ c-)^2))\ /(R(d(\ R..,.+Rroa\ r\ m; \\
&+ i6\ (c\text{-}Rioad + .t;' + 2R \bullet c-)2]\ b'''P
\end{aligned}
$$